Mechanistic understanding of the marine biogeochemical proxy δ^{30}Si: A modeling approach

Dissertation

zur Erlangung des akademischen Grades eines
Doktors der Naturwissenschaften
– Dr. rer. nat –
am Fachbereich 2 (Biologie/Chemie) der Universität Bremen

Shuang Gao
Bremen, Februar 11, 2014

Gutachter

Prof. Dr. Dieter A. Wolf-Gladrow
Prof. Dr. Christina De La Rocha
Tag des Promotionskolloquiums: März 27, 2014

Acknowledgements

Many years later, when I recall my Ph.D time, I am sure I will still be grateful to many of these people....

I would like to give special thanks first to my advisor Christoph Völker. He guided me from the very first day as a modeler throughout these years with his enthusiasm, gentle encouragement and great patience. He is my primary resource for getting help with science and model technique related questions. He has been supportive academically and emotionally during the toughest time of my Ph.D. I appreciate very much his great contribution of time, ideas and advices throughout my whole Ph.D time and especially during the thesis writing.

I would also like to give heartfelt thanks to Dieter Wolf-Gladrow, who brought me into modeling field and has been supportive since I was a Master student. He has given me a lot of freedom in research and at the same time, provided me insightful suggestions with his profound knowledge on the subject and beyond. His fast feedbacks, gentle encouragement and relaxed demeanor made my Ph.D experience stimulating and rewarding.

I am very grateful to my Ph.D committee members Gerrit Lohmann and Martin Butzin for their constructive suggestions, fruitful discussions with me and fast response to my questions.

I am also thankful to Christina De La Rocha for inspirational discussions during conferences, fast response to my questions regarding measurement data and reviewing my thesis.

I would like to give special thanks to Ernst Maier-Reimer for helpful discussions and suggestions on model techniques. Although he has left us, his enthusiasm for science was contagious and stimulates us still.

I thank Claudia Hanfland, Claudia Sprengel, Dörte Rosenbaum, Jelle Bijma and POLMAR graduate school as a whole for providing me great chances to attend many courses, conferences, trainings and social events. Without POLMAR, my Ph.D time wouldn't be so colorful.

I am very lucky to be one of the Biogeos, who provide a friendly and family-like atmosphere. I am especially grateful to our group's secretary, Dörte Rosenbaum, for her great help with translation of the thesis abstract. She keeps us organized with miscellaneous daily routines and is always ready to help. Thanks to Dorothee Kottmeier for joining and organizing my thesis defense committee.

I thank my former colleagues Xu Xu and Ying Ye as well as present colleagues Judith Hauck, Tingting Wang, Xiaoping Yao, Christian Stepanek and Xu Zhang for their great helps with model techniques and for sharing their experiences with modeling skills and softwares.

I am grateful for time spent with my office mates Nina Keul and Ella Howes. Nina was always ready to help when she was here and her enthusiasm was contagious. I am indebted to Ella for her help to proofread and to give suggestions regarding English at any time.

I would like to thank my dear friend Mirja Hoins as well as her family for their great support throughout my time here. I very much appreciate the time we spent together in learning languages, watching movies, cycling, cooking or simply ”quatschen”. I will never forget the last Christmas we had together when the first time I felt like at home.

I must also mention my great friends Qun and Sven Göthel, who are always enthusiastic, warm-hearted and helpful. I would like to thank them for their care and encouragement throughout the time, especially during my thesis writing.

This acknowledgement would not be complete if I do not mention my special friend of six years, Falk Wilfert. I cannot count how many days and nights we were discussing my work and my future plans. He always feels with me, motives me and supports me. He helps me unconditionally with my work, such as proofreading. He also gave me many precious memories along the way and made a place in my heart he will ever occupy. My dear, I want you to know that I am deeply indebted to you for your support and care.

At the end I would like to thank my family and my Chinese friends in my mother tongue....

致 谢

亲爱的老爸老妈，首先要感谢的肯定是你们。感谢你们这么多年以来对女儿的关怀、支持、理解和无条件付出。在德国求学的五年有辛苦也有收获，你们的信任和期盼一直是我在困难时刻坚持走下去的动力。我深深知道不管今后我将何去何从，你们永远是我的心灵支柱和容我停泊的温暖港湾。

身在他乡的日子，最挂念的人莫过于奶奶。还记得以前您每晚都陪我学习，有时甚至到深夜。为不影响我，您晚上从来不看电视。一个又一个漫漫长夜，您就这么陪着我熬过来。至今我都还记得橘黄的灯光下，您就坐在我身后的那种温暖感觉。如今您已是九十高龄，我每每都为自己不能在您身边尽孝而感到愧疚万分。奶奶，若是没有您的辛勤付出，就肯定不会有我的今天，我对您的感激之情无以言表。

在好山好水好寂寞的国外，有三五个能分享快乐、分担痛苦的朋友是人生之幸事。我要首先感谢姚晓萍和王婷婷这两个好姐妹这么多年以来的陪伴，对我的照顾和担当。还要感谢张群一直以来对我的关心和帮助，特别是在我写论文期间的督促和鼓励。我要特别感谢曾经的室友任健这些年来对我在生活和工作中诸多的无私帮助。还要感谢邹昊一直以来的支持，特别是在我论文写作期间为我提供的无数次蹭饭机会。感谢所有曾经关心帮助过我的中国朋友，不管你们现在是否还在我的身边。因为有你们，就算身在不来梅港也能感受到阳光般的温暖。

Abstract

The stable silicon isotopic composition δ^{30}Si of silicic acid and of biogenic opal is used as a proxy for investigating the marine silicon cycle and silicic acid utilization by diatoms both at present and in the geological past. The marine biogeochemical and physical processes involved in determining the modern δ^{30}Si distribution have not been fully understood. Hence, the usage of δ^{30}Si as a proxy for reconstruction of the marine silicon cycle and paleoproductivity by diatoms is hampered. This work is aimed at providing a comprehensive view and systematic approaches for understanding the oceanic δ^{30}Si distribution and its controlling mechanisms under both present and the last glacial maximum (LGM) climate conditions. A coupled ocean (MPI-OM)-biogeochemical (HAMOCC5.1) model is applied to simulate the marine silicon cycle and the silicon isotopic fractionation processes during biogenic opal production and dissolution.

In the present-day simulation, the surface δ^{30}Si increases along a Rayleigh type distillation curve during the utilization of silicic acid by diatoms, which demonstrates the primary control of biological fractionation on the surface δ^{30}Si distribution. The variations between the Rayleigh curves in different ocean basins, on the other hand, show the impact of physical transport of water on determination of the surface δ^{30}Si. In the deep ocean, our model captures a significant silicon isotopic gradient between the North Atlantic and the North Pacific. The advection related to the thermohaline circulation is thought to be the essential controlling factor of deep ocean δ^{30}Si. The model-data comparison implies that the usage of fractionation during biogenic opal dissolution as explanation to δ^{30}Si distribution is still speculative. The modeled silicic acid concentrations and δ^{30}Si show good agreement with the observations, when only fractionation during opal production is considered. The capability of the model to reproduce the large-scale modern oceanic δ^{30}Si distribution gives us confidence in simulating the δ^{30}Si during the LGM.

In the LGM simulation, the extension of sea-ice cover in both the Northern and the Southern Hemisphere may cause a reduction of phytoplankton growth due to low light under the ice. The silicic acid utilization by diatoms especially around Antarctica is therefore inhibited, in line with reduced biogenic opal export fluxes. Our preliminary model results of the glacial Si isotopic composition agree with the interpretation from sediment core data that silicic acid utilization by diatoms in the Southern Ocean during the LGM was diminished relative to the present interglacial.

The sensitivity of δ^{30}Si to glacial-interglacial ocean physical variations such as the strength of overturning circulation and ocean surface mixing is tested, using a simple seven-box model. The results indicate that the changes in global average δ^{30}Si due to the glacial-interglacial ocean physical variation may be of a similar magnitude as the total glacial-interglacial δ^{30}Si variation.

The modeling approach is a valid and powerful tool of promoting a mechanistic understanding of the marine biogeochemical proxy δ^{30}Si. One important advantage over common interpretation of local field studies is that models calculate isotopic fractionation without application of Rayleigh or open system approximation. In addition, the sensitivity of δ^{30}Si to various biogeochemical and physical factors can be tested systematically.

Zusammenfassung

Die stabile Isotopenzusammensetzung δ^{30}Si von Kieselsäure und biogenem Opal wird als Proxy zur Untersuchung des marinen Silizium-Kreislaufs und der Kieselsäurenutzung durch Diatomeen sowohl im heutigen Ozean als auch in dem der geologischen Vergangenheit verwendet. Die marinen biogeochemischen und physikalischen Prozesse, die bei der Bestimmung der heutigen δ^{30}Si-Verteilung beteiligt sind, sind noch nicht vollständig entschlüsselt worden. Daher ist der Gebrauch von δ^{30}Si als Proxy zur Rekonstruktion des marinen Silizium-Kreislaufs und der Paläoproduktivität durch Diatomeen erschwert. Die vorliegende Arbeit hat zum Ziel, eine verständliche Übersicht und systematische Ansätze zum Verständnis der ozeanischen δ^{30}Si-Verteilung und seiner Kontrollmechanismen zu geben, wie sie sowohl unter heutigen klimatischen Bedingungen als auch der während des letzten Vereisungsmaximums (LGM) herrschten. Es wird ein gekoppeltes Ozeanzirkulations (MPI-OM) und biogeochemisches Modell (HAMOCC5.1) verwendet, um den marinen Silzium-Kreislauf und die Isotopenfraktionierungsprozesse des Siliziums während der biogenen Opalproduktion und -auflösung zu simulieren.

In der Gegenwarts-Simulation steigt der δ^{30}Si-Gehalt in der Oberflächenschicht des Ozeans entlang einer Rayleigh-Destillations-Kurve während der Kieselsäureaufnahme durch Diatomeen. Dies zeigt den primär treibenden biologischen Faktor der Fraktionierung der δ^{30}Si-Verteilung an der Oberfläche. Die Variation zwischen den Rayleigh-Kurven in verschiedenen Ozeanbecken zeigt aber andererseits den nicht zu vernachlässigenden Einfluss des physikalischen Wassertransports auf die Oberflächen-δ^{30}Si-Verteilung. In der Tiefsee erfasst das Modell einen signifikanten Siliziumisotopengradienten zwischen dem Nordatlantik und dem Nordpazifik. Die mit der thermohalinen Zirkulation zusammenhängende Advektion wird als der ausschlaggebende Kontrollfaktor der δ^{30}Si-Verteilung in der Tiefsee angesehen. Die modellierten Kieselsäurekonzentrationen und δ^{30}Si-Werte zeigen eine gute Übereinstimmung mit den Beobachtungen, wenn nur die Fraktionierung während der Opalproduktion berücksichtigt wird. Der Vergleich der Modelldaten deutet an, dass die Nutzung der Fraktionierung während der biogenen Opalauflösung als Erklärung für die δ^{30}Si-Verteilung noch recht spekulativ ist. Die Fähigkeit des Modells, großskalige heutige ozeanische δ^{30}Si-Verteilungen zu reproduzieren, gibt uns die Zuversicht, im Folgenden dann die Verteilung von δ^{30}Si während des letzten Vereisungsmaximums zu simulieren.

In der LGM-Simulation zeigt sich eine Vergrößerung der Meereisbedeckung sowohl in der Nord- als auch in der Südhemisphäre. Diese verursacht eine Reduktion des Phytoplankton-Wachstums aufgrund von Lichtmangel unter dem Eis. Die Kieselsäurenutzung

durch Diatomeen im Südpolarmeer ist deshalb reduziert und führt zu reduzierten biogenen Opalexport-Flüssen in hohen Breiten in beiden Hemisphären. Unsere - noch vorläufigen - Modell-Ergebnisse zur glazialen Si-Isotopenzusammensetzung stimmen überein mit der Interpretation aus Sedimentkern-Daten, dass die Kieselsäureverwertung durch Diatomeen in höheren Breiten des Südlichen Ozeans während des letzten Vereisungsmaximums im Verhältnis zum heutigen Interglazial vermindert war.

Die Sensitivität von δ^{30}Si im Hinblick auf glazial-interglaziale Änderungen der physikalischen Ozeanzirkulation, wie z. B. der Stärke der Umwälzzirkulation und Durchmischung des Oberflächenwassers wird mit einem einfachen Sieben-Box-Modell getestet. Die Resultate zeigen, dass die Änderungen im globalen Durchschnitts δ^{30}Si durch Zirkulationsänderungen von einer ähnlichen Größenordnung sein können wie der gesamte glazial-interglaziale δ^{30}Si Unterschied.

Der Modellierungsansatz ist ein wertvolles Werkzeug zur Unterstützung eines mechanistischen Verständnisses des marinen biogeochemischen Proxy δ^{30}Si. Ein wichtiger Vorteil gegenüber der bisher üblichen Interpretation von lokalen Feldstudien ist, dass Modelle die Isotopenfraktionierung ohne die Anwendung von vereinfachenden Annahmen, wie der Rayleigh-Fraktionierung oder der Fraktionierung in einem stationären offenen System berechnen. Darüber hinaus kann die Sensitivität von δ^{30}Si gegenüber verschiedenen biogeochemischen und physikalischen Faktoren im Modell systematisch getestet werden.

Contents

Chapter 1

Introduction

1.1 The marine silicon cycle and its connection to the carbon cycle and climate

1.1.1 Silicon and the marine silicon cycle

Silicon is the second most abundant element in the Earth's continental crust (∼28% by mass) after oxygen (*Rudnick and Gao*, 2003). The global biogeochemical Si cycle has received significant scientific attention in the last decades, because it is widely believed to have a great impact on global CO_2 levels and hence global climate, through the combined processes of the weathering of silicate minerals and transfer of CO_2 from the atmosphere to the ocean and finally to the lithosphere (*Berner*, 1997; *Conley*, 2002). Terrestrial and oceanic Si cycles are the two major components of the global Si cycle. The chemical weathering of continental rocks releases dissolved silicon (DSi) into rivers and ground waters that ultimately reach the ocean. During the transport on land from the weathering site to the ocean, the DSi may be used by plants or fresh water diatoms to form specific siliceous structures (biogenic silica, BSi) such as silica cells in grasses and reproductive structures of plants (phytoliths) (*Kaufman et al.*, 1981). The BSi, besides DSi, formed on the continents accounts for 16% of the gross riverine Si input into the ocean, espe-

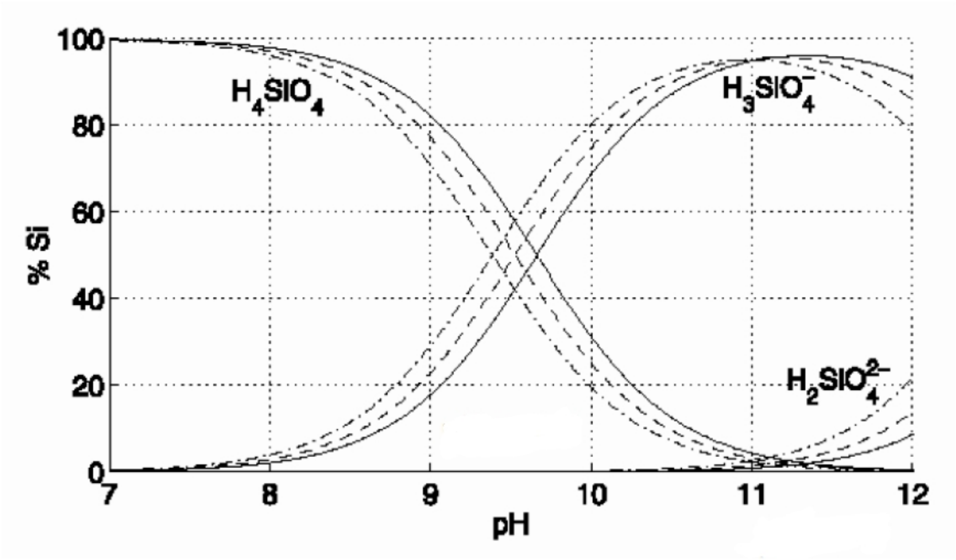

Figure 1.1: Relative abundances of silicic acid species as a function of pH and temperature. T = 10 °C (solid line), T = 17 °C (dashed line), T = 25 °C (dash-dotted line) (from *Wischmeyer* (2002)).

cially during high river discharge (*Conley*, 1997). The terrestrial Si cycle, thus, is closely connected with the marine Si cycle through the discharge of Si.

Silicon exists in the ocean either in the dissolved phase, primarily in form of orthosilicic acid ($Si(OH)_4$), with only ∼5% present in dissociated form ($SiO(OH)_3^-$) at pH 8.2 (Figure 1.1), or in solid phase mainly as lithogenic silica (LSi) or biogenic silica (BSi). Lithogenic silica is formed by inorganic processes from terrestrial sources of rock and soil, while biogenic silica ($SiO_2 \cdot nH_2O$) derives from siliceous sponges and various marine plankton, including diatoms, radiolaria, silicoflagellates during the formation of their siliceous skeletal structures (e.g. diatom frustules and sponge spicules) (*Conley and Schelske*, 2001), by taking up silicic acid from seawater. Since diatoms are by far the most productive siliceous organisms in the modern marine environment (*Nelson et al.*, 1995; *Tréguer et al.*, 1995) and our focus is on the oceanic biogeochemical Si cycle, we use biogenic silica or biogenic opal mostly to refer to marine diatom frustules.

The magnitude of fluxes in the marine Si biogeochemical cycle has been quantified at the end of twentieth century (*Tréguer et al.*, 1995) and more recently (*Ragueneau et al.*, 2000; *Laruelle et al.*, 2009; *Tréguer and De La Rocha*, 2013). The ocean contains approximately 97,000 Tmol Si (*Tréguer and De La Rocha*, 2013). An up-to-date estimate of the net inputs of dissolved silicon to the world ocean amounts to 9.4 ± 4.7 Tmol Si yr^{-1} (*Tréguer and De La Rocha*, 2013), including continental inputs (8.3 Tmol Si yr^{-1} containing net river inputs, groundwater flux and seafloor weathering inputs), aeolian inputs (0.5 Tmol Si yr^{-1}) and hydrothermal inputs (0.6 Tmol Si yr^{-1}), with a contribution of the net riverine input of ~62% (Figure 1.2b). In the surface ocean, biogenic silica is produced by siliceous organisms, mainly by diatoms, at a rate of ~240 Tmol Si yr^{-1} with 136 Tmol Si yr^{-1} in the coastal zone, 23 Tmol Si yr^{-1} in the open ocean excluding the Southern Ocean and 80 ± 18 Tmol Si yr^{-1} in the Southern Ocean south of the Polar Front Zone (PFZ: <51 °S) (*Tréguer and De La Rocha*, 2013). More than half (~56%) of the silica production dissolves directly in the surface mixed layer, while the remaining 44% of the production, which escape dissolution, sink down toward the ocean interior. The competition between biogenic silica dissolution in surface waters and its export to the deep waters is controlled by both intrinsic features of silica dissolution (see section 1.1.2) and external factors which influence silica export such as seasonality, food web structure and aggregation (*Ragueneau et al.*, 2000). The exported silica further dissolves during sinking through the deep ocean, releasing silicic acid. The total dissolution rate of Si in the deep ocean amounts to 26.2 Tmol Si yr^{-1} by a new estimate (*Tréguer and De La Rocha*, 2013), which differs from the previous estimate of 90.0 Tmol Si yr^{-1} (*Tréguer et al.*, 1995). The surviving biogenic silica ultimately reaches the marine sediment and a proportion of 92% of the siliceous "rain material" is recycled at the sediment-water interface according to the new estimation by *Tréguer and De La Rocha* (2013). It is notable that the recycling of Si occurs mainly at the sediment-water interface rather than in the deep waters as reported previously by *Tréguer et al.* (1995). This updated estimate falls in line with observations by *Nelson et al.* (2002) and *Honjo et al.* (2008). Only less than 3% of the silica produced in the euphotic zone is permanently buried in the sediment (*DeMaster*, 2002; *Tréguer and De La Rocha*, 2013). Together with the net sink of biogenic silica in sponges on continental shelves, this balances approximately the net inputs of Si to the

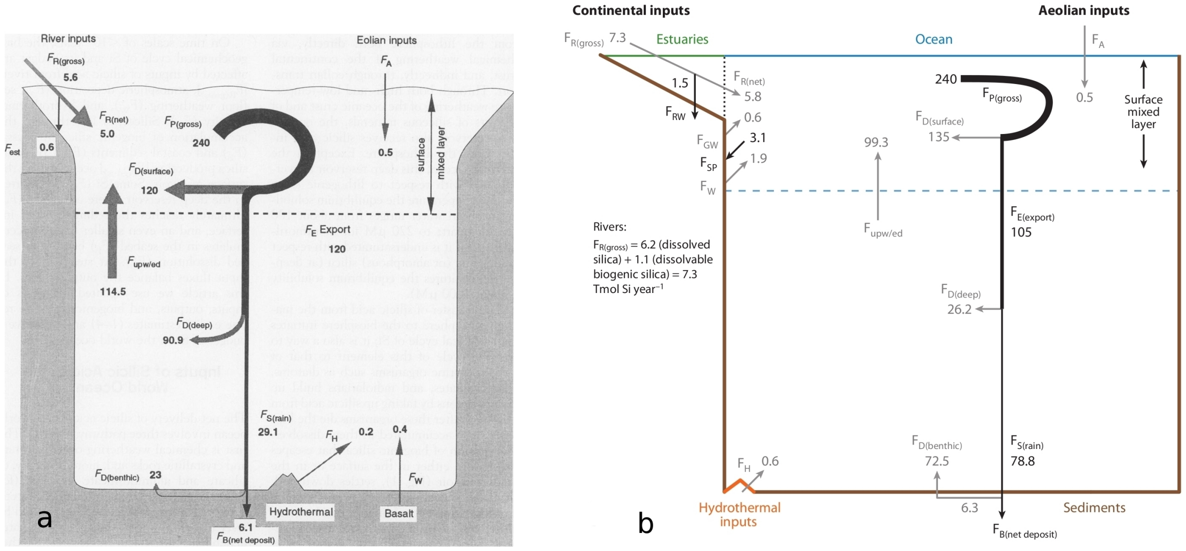

Figure 1.2: Biogeochemical cycle of silicon in the world ocean at steady state ((a) taken from *Tréguer et al.* (1995); (b) taken from *Tréguer and De La Rocha* (2013)): a possible balance that is in reasonable agreement with the individual range of each flux (F). The dotted line represents the limit between the estuaries and the ocean. Gray arrows represent fluxes of silicic acid (dissolved silica) and black arrows represent fluxes of particulate biogenic silica; all fluxes are in teramoles of silicon per year. Abbreviations: $F_{R(gross)}$, gross river inputs; $F_{R(net)}$, net river inputs; F_{RW}, deposits of biogenic silica and reverse weathering in estuaries; F_{GW}, groundwater flux; F_A, aeolian inputs; F_H, hydrothermal inputs; F_W, seafloor weathering inputs; $F_{P(gross)}$, biogenic silica gross production; $F_{D(surface)}$, flux of silicic acid recycled in the surface reservoir; $F_{E(export)}$, flux of biogenic silica exported toward the deep reservoir; $F_{D(deep)}$, flux of silicic acid recycled in deep waters; $F_{D(benthic)}$, flux of silicic acid recycled at the sediment-water interface; $F_{S(rain)}$, flux of biogenic silica that reaches the sediment-water interface; $F_{upw/ed}$, flux of silicic acid transferred from the deep reservoir to the surface mixed layer (upwelling, eddy diffusion); $F_{B(netdeposit)}$, net deposition of biogenic silica in coastal and abyssal sediments; F_{SP}, net sink of biogenic silica in sponges on continental shelves.

world ocean (Figure 1.2). According to the estimate by *Tréguer and De La Rocha* (2013), the residence time for silicon in the ocean is ∼10,000 years, shorter than the previous estimates by *Tréguer et al.* (1995) and *Laruelle et al.* (2009). The residence time for biological uptake of dissolved Si is ∼400 years, which indicates that silicon delivered into the ocean passes through the biological uptake and dissolution cycle an average of 25 times before being removed to the seabed (*Tréguer and De La Rocha*, 2013).

1.1.2 Silica dissolution dynamics

The saturation concentration of silicic acid in seawater is much higher than even the highest silicic acid concentrations observed in the ocean and thus seawater is strongly undersaturated with respect to biogenic silica. The dissolution rate of silica rises exponentially with increasing undersaturation (*Van Cappellen and Qiu*, 1997; *Rickert et al.*, 2002). The dissolution rate of silica varies with temperature because of the temperature dependence of (1) the saturation concentration and (2) the activity of bacteria that speeds up dissolution (*Kamatani*, 1982; *Bidle et al.*, 2002). At higher ambient temperature, diatom frustules thus dissolve more rapidly (*Kamatani*, 1982; *Hurd and Birdwhistell*, 1983; *Brzezinski and Nelson*, 1995; *Demarest et al.*, 2009). The dissolution rate of biogenic silica exhibits a decrease over time or with increasing water depth when in situ, at different temperatures. This decrease is likely due to the reduction of overall surface area and an increase of the fraction of less soluble structures in the frustules as dissolution proceeds (*Kamatani*, 1982; *Rickert et al.*, 2002; *Demarest et al.*, 2009). In addition, biogenic silica dissolution is also affected by diatom species in terms of specific surface areas or morphology and structure of the frustules (*Kamatani*, 1982; *Ehrlich et al.*, 2010; *Passow et al.*, 2011), bacterial degradation (*Bidle and Azam*, 1999; *Bidle et al.*, 2002), grazing (*Jacobson and Anderson*, 1986; *Miller et al.*, 1990) and trace elements within the opaline matrix (e.g. Aluminium) (*Van Bennekom et al.*, 1991; *Rickert et al.*, 2002).

1.1.3 Diatoms

Diatoms are a major group of phytoplankton, belonging to the Bacillariophyceae class, with an estimate of 200,000 different species (*Armbrust*, 2009), ranging in size from approximately 10 μm to 200 μm. They exist either as single cells or as colonies (*Mann and Droop*, 1996). Silicon is clearly important for diatoms because silica forms a major part of their cell walls. It has also been hypothesized that it is involved in a variety of metabolic processes (*Round et al.*, 1990). The diatom cell wall consists of two valves, of which the slightly larger valve (epitheca) overlaps the narrower one (hypotheca), and they together enclose and protect the protoplast. The valves are connected with several thin, linking structures termed girdle bands or cincture. The girdle band in the theca overlapping region is called pleural band (Figure1.3 center). Beside silica the cell wall also contains a thin organic coating around the frustule, which protects diatom shells from dissolution. The diatom cell walls can be classified into three major morphological types if we observe them in "valve view" (versus "girdle view"): radial centrics, polar centrics, and pennates (Figure 1.4).

Only around 50 years ago it was discovered by *Drum and Pankratz* (1964) via electron microscopic examinations that construction of new diatom cell walls takes place within a membrane-limited compartment termed silica deposition vesicle (SDV). Silicic acid is taken up actively into the cell across the plasmalemma and concentrated in the SDV by means of specific transporter proteins (SITs) (*Kröger and Poulsen*, 2008). It is believed that diatoms create large intracellular pools of soluble silicon at supersaturated levels (*Sullivan*, 1986; *Blank et al.*, 1986). The location of these soluble silicon pools and the mechanism of intracellular transport of silicic acid to the SDV are still unknown. The deposition of silica occurs by polycondensation of silicic acid inside different SDVs for valves and girdle bands formation, respectively (Figure 1.3). When deposition completes, the new silica elements are added on the cell wall by exocytosis via fusion of the SDV membrane with the plasmalemma, though the exact mechanism is under debate. The organic components within the SDV such as silaffins and long-chain polyamines are believed to initiate and accelerate silicic acid polycondensation and further influence the silica nanostructure (*Kröger and Poulsen*, 2008).

As indicated in Figure 1.3, the formation of new valves always takes place within the confines of the parental cell wall, which leads to a size reduction in the cell that inherits the parental hypotheca; this is one of the best known features of diatom biology (*Round et al.*, 1990). Diatom cells undergo vegetative division until the cell is about one-third its initial size (*Hasle and Syvertsen*, 1996). Sexual reproduction then takes place and restores

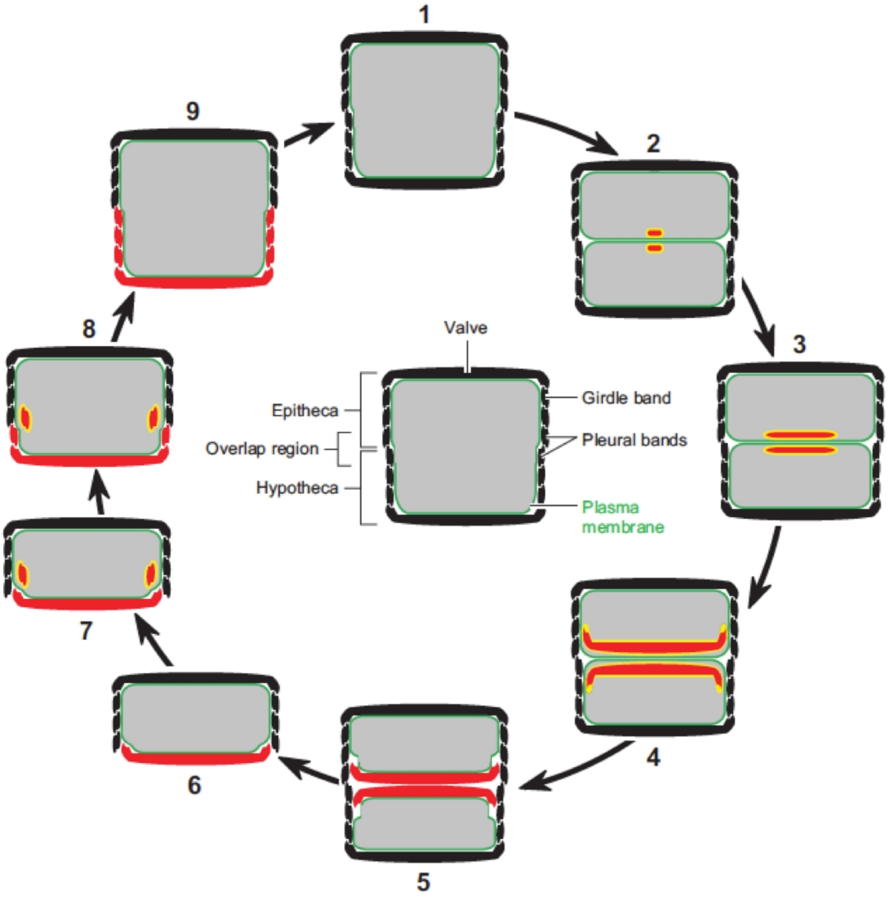

Figure 1.3: Schematic structure of the diatom cell (center) and diatom cell cycle (taken from *Kröger and Poulsen* (2008)). Diatom cells are shown in cross section. The gray area represents the protoplast, the green line depicts the plasma membrane. For simplicity, intracellular organelles other than the silica deposition vesicle (SDV) are not shown. Cells arranged in the circle show different stages of the cell cycle: (1) Shortly before cell division the cell wall contains the maximum number of girdle bands; (2) immediately after cytokinesis new biogenic silica (red) is formed in each sibling cell inside a valve SDV (yellow); (3) expansion of the valve SDVs as more and more silica is deposited; (4) at the final stage of valve SDV development, each SDV contains a fully developed valve; (5) the newly formed valves are deposited in the cleavage furrow on the surface of each protoplast by SDV exocytosis; (6) the sibling cells have separated; (7+8) expansion of the protoplast in interphase requires the synthesis of new silica (red) inside girdle band SDVs (yellow); each girdle band is synthesized in a separate SDV, and after SDV exocytosis is added to the newly formed valve (hypovalve); (9) after synthesis of the final hypovalve girdle band (pleural band) cell expansion stops, and DNA replication is initiated.

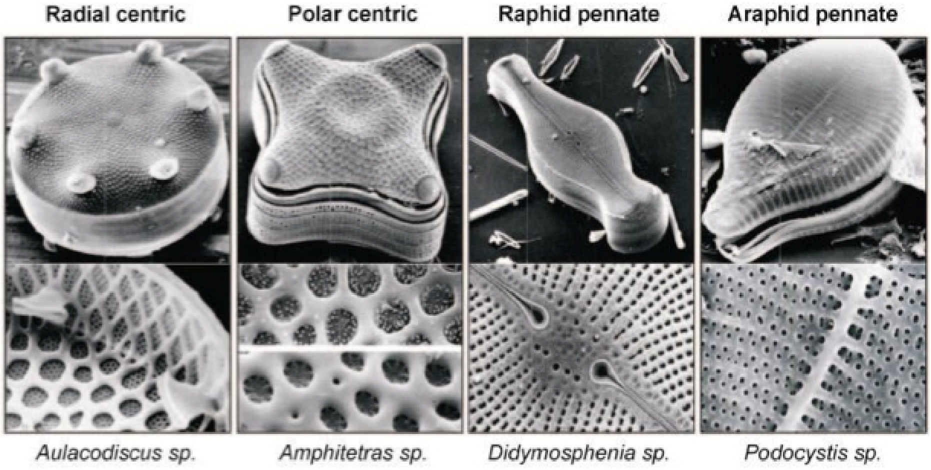

Figure 1.4: Structure and biogenesis of diatom cell walls. Scanning electron microscopy (SEM) images of the cell walls of four different diatom species (taken from *Kröger and Poulsen* (2008)).

the cell size of a diatom population. The male and female gametes that are produced via meiosis fuse to form a special zygote called auxospore. An initial diatom cell of maximum size is formed within the auxospore and thus a new generation begins.

1.1.4 Connection of the marine silicon cycle to the carbon cycle and climate

Diatoms contribute up to half of the modern oceanic primary production (*Nelson et al.*, 1995) and to much of the export of organic carbon from the surface waters (*Dugdale et al.*, 1995; *Buesseler*, 1998; *Smetacek*, 1999). The biogenic silica as one of the "ballast" minerals other than $CaCO_3$ and lithogenic mineral, participates in transporting organic carbon to the deep ocean via a process known as the "biological pump". Through this way, the silicon cycle is coupled with the carbon cycle and further plays a role in influencing the world's climate through regulating the $p\mathrm{CO}_2$ level (*Broecker and Peng*, 1993). The interaction between the silicon and carbon cycle happens at different scales with large temporal and spatial variations (*Ragueneau et al.*, 2006). At the cellular level, the Si:C ratio is influenced by various environmental factors. The Si:C ratio increases when diatom growth is limited by macronutrients like N, P (*Claquin et al.*, 2002) or by trace elements like Fe (*Takeda*, 1998; *Hutchins and Bruland*, 1998). Higher Si:C ratios are observed when diatoms are under grazing pressure (*Smetacek*, 1999; *Pondaven et al.*, 2007). On the other hand, under severe Si limitation the Si:C ratio decreases, which can be simulated by a half-saturation constant that is less for growth than for Si uptake (*Martin-Jézéquel et al.*, 2000). *Baines et al.* (2010) suggest that ecological factors such as community composition may cause systematic regional and temporal differences in cellular stoichiometry of Si to carbon and to other nutrients.

At the global scale, the opal to POC (particulate organic carbon) ratio of phytoplankton varies during primary production in different ocean regions possibly due to regional differences in the supply ratio of silicic acid and nitrate (*Ragueneau et al.*, 2002). In addition, the proportion of primary production that is carried out by diatoms (opal producers) or by coccolithophores (carbonate producers) differs spatially. A recent study found that thick-shelled diatom species that evolve in response to heavy copepod grazing pressure sink mainly as empty shells to depth, decoupling silicon and carbon cycles in the iron-limited Southern Ocean (*Assmy et al.*, 2013). This indicates that ecology has an impact on marine biogeochemical cycles. Despite the increase in Si:C ratio with depth, the spatial differences in the opal to POC ratio seem to convey down to deeper waters (*Ragueneau et al.*, 2002). Recent studies on temporal (*Lam et al.*, 2011) and regional (*Ragueneau et al.*, 2006; *Wilson et al.*, 2012) variabilities of POC and ballast mineral sinking fluxes point out that there needs to be a shift in the focus from a geochemical point of view toward a more ecological point of view, in order to better understand the variability of Si:C ratio or carrying coefficient and the functioning of the biological pump. A better understanding of the factors controlling the degree of coupling between the silicon and carbon biogeochemical cycles is needed when using biogenic opal as a proxy for paleoproductivity referring to past climate change (*Pondaven et al.*, 2000).

1.2 Stable silicon isotopes

Isotopes are atoms with the same number of protons and thus chemical characteristics but different neutron numbers in their nuclei. Thus they are located in the same ("isos" in Greek) place ("topos" in Greek) in the periodic table of elements. Depending on whether there is a detectable decay of the nucleus or not, isotopes can be classified into two fundamental groups, radioactive and stable species. Silicon has three stable isotopes, ^{28}Si, ^{29}Si and ^{30}Si, with mean abundances of 92.17515%, 4.67739% and 3.14746%, respectively (*Ding et al.*, 2005).

1.2.1 Notation

The isotopic ratio of silicon is defined as the ratio of the abundance of one of the rare isotopes to the abundance of the most abundant isotope,

$$^{29}R = \frac{^{29}\mathrm{Si}}{^{28}\mathrm{Si}} \tag{1.1}$$

$$^{30}R = \frac{^{30}\mathrm{Si}}{^{28}\mathrm{Si}}. \tag{1.2}$$

The isotopic composition δ (‰) of a sample is expressed as the difference between the isotopic ratio of the sample and that of a standard, relative to the isotopic ratio of the standard, times 1000,

$$\delta^{29}\mathrm{Si} = (\frac{^{29}R_{\mathrm{sample}}}{^{29}R_{\mathrm{NBS-28}}} - 1) \cdot 10^3 \ (‰) \tag{1.3}$$

$$\delta^{30}\mathrm{Si} = (\frac{^{30}R_{\mathrm{sample}}}{^{30}R_{\mathrm{NBS-28}}} - 1) \cdot 10^3 \ (‰). \tag{1.4}$$

The standard is synthetic silica sand (NBS, the United States National Bureau of Standards, now renamed as NIST, the National Institute of Standards and Technology), whose isotopic ratios are reported by *Coplen et al.* (2002) as

$$^{29}R_{\mathrm{NBS-28}} = \frac{^{29}\mathrm{Si}}{^{28}\mathrm{Si}} = \frac{4.6853\%}{92.22223\%} = 0.0508044 \tag{1.5}$$

$$^{30}R_{\mathrm{NBS-28}} = \frac{^{30}\mathrm{Si}}{^{28}\mathrm{Si}} = \frac{3.0924\%}{92.22223\%} = 0.0335320. \tag{1.6}$$

The Si isotopic ratios of the standard (NBS-28) has been modified by *Ding et al.* (2005) to 0.0507446 for $^{29}\mathrm{Si}/^{28}\mathrm{Si}$ and 0.0341465 for $^{30}\mathrm{Si}/^{28}\mathrm{Si}$. The calculations in this thesis, however, are based on the earlier measurements (Eqs. 1.5 and 1.6) in order to enable a direct comparison with previous studies.

The fractionation factor (α) of a chemical or biological process is defined as the isotopic ratio of product A divided by that of the source B,

$$\alpha_{\mathrm{A-B}} = \frac{\mathrm{R_A}}{\mathrm{R_B}}. \tag{1.7}$$

Equation 1.7 can be also expressed in terms of the δ-values as follows.

$$\alpha_{\mathrm{A-B}} = \frac{\delta_{\mathrm{A}} + 10^3}{\delta_{\mathrm{B}} + 10^3} \tag{1.8}$$

As α is usually very close to 1, the deviation of α from 1 in parts per thousand (ϵ notation) is often used to express the degree of isotope fractionation. Combined with Equation 1.8, ϵ can be approximated by the difference between the δ values of the two substances, A and B, if α is close to unity.

$$\epsilon_{\mathrm{A-B}} = (\alpha_{\mathrm{A-B}} - 1) \cdot 10^3 = \frac{\delta_{\mathrm{A}} - \delta_{\mathrm{B}}}{1 + \delta_{\mathrm{B}}/10^3} \approx \delta_{\mathrm{A}} - \delta_{\mathrm{B}}\,(‰) \tag{1.9}$$

In the case of diatom opal formation by uptake of silicic acid, the fractionation factor is

$$\alpha_{\mathrm{BSi-DSi}} = \frac{\mathrm{R_{BSi}}}{\mathrm{R_{DSi}}}, \tag{1.10}$$

and the fractionation is

$$\epsilon_{\mathrm{DSi-BSi}} \approx \delta_{\mathrm{DSi}} - \delta_{\mathrm{BSi}}. \tag{1.11}$$

The values of $^{30}\alpha$ and $^{30}\epsilon$ for biogenic opal production by diatoms have been estimated to be 0.9989 and -1.1‰, respectively, by *De La Rocha et al.* (1997).

1.2.2 Closed system and open system

Isotope fractionation is usually discussed under two idealized circumstances, a closed system (Rayleigh model) and an open system. In a closed system, the substrate is added once at the beginning of a reaction and it is not renewed over the course of the reaction. The substrate is progressively consumed over time, sequentially decreasing in concentration, while the product accumulates in the system. Diatoms deplete silicic acid in the surface water within a few days during a bloom, which can be treated approximately as a closed system, because the nutrient uptake greatly exceeds new inputs from vertical mixing. In contrast, the substrate in an open system is continually renewed, while at the same time, the product and unused substrate flow out of the system (*Fry*, 2006).

For silicon isotopes the fractionation dynamics in both systems are shown in Figure 1.5. In the closed system, one should distinguish between the biogenic silica produced at each instant and the accumulated biogenic silica produced over a period of time (e.g. during a bloom). Their isotopic compositions are described by the following equations, which follow from mass balance.

$$f = \frac{[\mathrm{Si(OH)_4}]_{\mathrm{remaining}}}{[\mathrm{Si(OH)_4}]_{\mathrm{initial}}} \tag{1.12}$$

$$\delta^{30}\mathrm{Si}_{\mathrm{DSi}} = \delta^{30}\mathrm{Si}_{\mathrm{DSi\,initial}} + \epsilon \cdot ln(f) \tag{1.13}$$

$$\delta^{30}\mathrm{Si}_{\mathrm{BSi\,inst}} = \delta^{30}\mathrm{Si}_{\mathrm{DSi}} + \epsilon \tag{1.14}$$

$$\delta^{30}\mathrm{Si}_{\mathrm{BSi\,acc}} = \delta^{30}\mathrm{Si}_{\mathrm{DSi\,initial}} - \epsilon \cdot \frac{f \cdot ln(f)}{1-f} \tag{1.15}$$

The notation f stands for the fraction of remaining silicic acid from the initial concentration in the system, ϵ indicates the fractionation between the instantaneously produced biogenic silica and the silicic acid pool. The instantaneous and accumulated BSi are noted as $\delta^{30}\mathrm{Si}_{\mathrm{BSi\,inst}}$ and $\delta^{30}\mathrm{Si}_{\mathrm{BSi\,acc}}$, respectively. The isotopic composition of silicic acid increases exponentially along a Rayleigh distillation curve as the lighter isotope $^{28}\mathrm{Si}$ is slightly preferred by diatoms when building their opaline shells. The BSi produced at any given point in time is offset by ϵ from the $\delta^{30}\mathrm{Si}$ value of silicic acid. The $\delta^{30}\mathrm{Si}$ value of the accumulated BSi in the closed system also increases as silicic acid concentration declines, but it can only span a range within the value of ϵ (Figure 1.5a).

Different from the closed system, there is only one product in the open system, which is the biogenic silica produced at an instant in time (Figure 1.5b). The isotopic compositions of both silicic acid and biogenic silica produced from it increase linearly, with an offset of ϵ between them. The equations governing the open system are shown as follows and notations are the same as in the closed system.

$$\delta^{30}\mathrm{Si}_{\mathrm{DSi}} = \delta^{30}\mathrm{Si}_{\mathrm{DSi\,initial}} - \epsilon \cdot (1-f) \tag{1.16}$$

$$\delta^{30}\mathrm{Si}_{\mathrm{BSi}} = \delta^{30}\mathrm{Si}_{\mathrm{DSi\,initial}} + \epsilon \cdot f \tag{1.17}$$

It is notable that in the ocean the silicon fractionation proceeds usually in a mixed way depending on the ocean circulation other than behaving in the way as shown in the two ideal models.

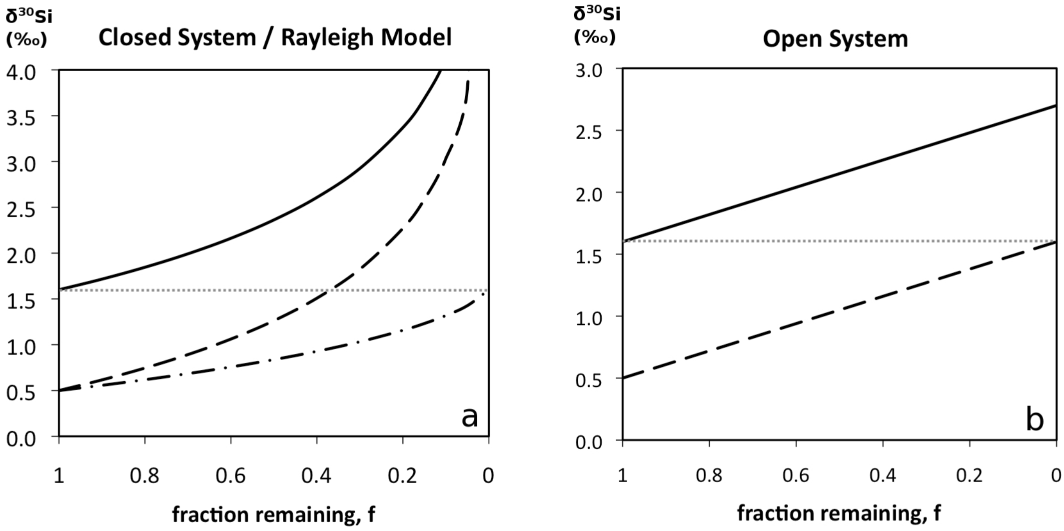

Figure 1.5: Silicon isotope dynamics in (a) closed system and (b) open system. In both figures δ^{30}Si of silicic acid is drawn in solid line, the instantaneously produced biogenic silica is in dashed line. The accumulated biogenic silica is drawn in dashed-dotted line in figure a. The grey lines indicate the initial input value of δ^{30}Si of silicic acid, which is +1.6‰ in both figures. The fractionation factor (ϵ) used here is -1.1‰.

1.2.3 State-of-the-art of research in δ^{30}Si

During the formation of diatom frustules, the lighter isotope ^{28}Si in silicic acid is taken up and incorporated preferentially into the shells, leaving the silicic acid in the water enriched in the heavier stable isotopes ^{29}Si and ^{30}Si. Given a finite pool of silicic acid, the continued preferential uptake of ^{28}Si by diatoms will result in a progressive increase in the relative abundance of the heavier isotopes in both dissolved and biogenic silica (see above about the "Rayleigh model"). In other words, the isotopic composition δ^{30}Si of silicic acid and of the opaline shells increases as silicic acid concentration decreases. Variations in the δ^{30}Si of the opaline shells that are buried in the sediments may therefore reflect the extent of silicic acid depletion in the surface water at the time when the shells were formed. Thus, δ^{30}Si holds a great potential as a proxy for investigation of marine silicic acid utilization and primary production by diatoms both at present and in the geological past. This proxy has been applied extensively in the Southern Ocean for investigating the glacial silicic acid concentration and productivity in order to explain the low glacial pCO$_2$

level (*De La Rocha et al.*, 1998; *Brzezinski et al.*, 2002; *Beucher et al.*, 2007; *Pichevin et al.*, 2009; *Ellwood et al.*, 2010).

The fractionation, ϵ, between silicic acid and biogenic silica in the frustules of diatoms has been evaluated by various laboratory studies. It has been determined by *De La Rocha et al.* (1997) in a series of laboratory experiments as ϵ = -1.1 ± 0.4 ‰ independent of temperature (12-22 °C), growth rate, or diatom species, for the three different species tested. Apart from that, *Milligan et al.* (2004) found that the fractionation ϵ during diatom opal formation is independent from $p\mathrm{CO}_2$ level (100-750 ppm), which supports a broader use of the proxy δ^{30}Si under various environmental conditions. However, a recent laboratory study has revealed some species-dependency of ϵ (ranging from -0.54 to -2.09‰) by marine diatoms, which draws attention to diatom taxonomic analysis when using δ^{30}Si, in the future, for reconstruction of Si utilization (*Sutton et al.*, 2013). Many field studies have investigated the in situ variability of ϵ for diatom opal formation (*De La Rocha et al.*, 2000; *Varela et al.*, 2004; *Cardinal et al.*, 2005; *Reynolds et al.*, 2006; *De La Rocha et al.*, 2011) or dissolution (*Demarest et al.*, 2009; *Beucher et al.*, 2011) with respect to using either the "Rayleigh model" (a relative isolated water mass with single input of silicic acid before the onset of diatom bloom) or the "steady state model" (an open water mass with continuous input of silicic acid throughout the diatom bloom). Progress has been made also by field studies on mechanisms that control δ^{30}Si distribution and variation, such as physical mixing, opal dissolution or iron availability, and its implication for tracing oceanic Si cycling (*Cardinal et al.*, 2005, 2007; *Reynolds et al.*, 2006; *Beucher et al.*, 2011; *Fripiat et al.*, 2011a,b, 2012; *de Souza et al.*, 2012a,b)

Modeling studies, on the other hand, provide comprehensive views and systematic approaches for understanding δ^{30}Si distribution and controlling mechanisms, because they calculate isotopic fractionation without application of Rayleigh or open system approximations. *Wischmeyer et al.* (2003) calculated an overall oceanic distribution of silicon isotopes using a three-dimensional global ocean circulation and biogeochemistry model for the first time. Their work revealed that the relationship between silicic acid concentration and its δ^{30}Si is not a simple Rayleigh distillation curve except in the Southern Ocean and in the equatorial Pacific. They also investigated the applicability of the correlation between silicic acid concentration in the surface water and the $\delta^{30}\mathrm{Si}_{\mathrm{BSi}}$ in the sediment for estimating the absolute silicic acid concentrations in the past. However, their model results did not show significant δ^{30}Si variations between the deep Atlantic and deep Pacific, which disagrees with the observational data (*De La Rocha et al.*, 2000). Using a seven-box model, *Reynolds* (2009) observed a 0.3‰ difference between the δ^{30}Si of the deep-water masses of North Atlantic and North Pacific. A very recent modeling study with a general circulation model (GCM) including Fe-dependent Si:N uptake ratio also showed a deep δ^{30}Si gradient between the North Atlantic and the Southern Ocean (*Matsumoto et al.*, 2013). There are only a few more modeling studies which focus on oceanic Si isotopes: *De La Rocha and Bickle* (2005) investigated the sensitivity of δ^{30}Si to the marine silica cycle taking advantage of a simple two-box model; *Fripiat et al.* (2012) and *de Brauwere et al.* (2012) used non-steady state box models for simulating temporal variations of δ^{30}Si during transient events like blooms in order to get a handle on how different isotopic effects influence the cycling of Si isotopes.

1.3 Aims of the thesis

It has been a decade since the first modeling of the global marine δ^{30}Si distribution was accomplished (*Wischmeyer et al.*, 2003). Given the growing body of field data collected since then, an up-to-date model-data comparison is feasible and desired. In this thesis I present a new setup of the marine silicon cycle and the silicon isotopic system in a global model for investigating δ^{30}Si both at present and in the Last Glacial Maximum (LGM). In addition, a multibox model is constructed to investigate sensitivities of δ^{30}Si to glacial-interglacial ocean physical parameters. This work is aimed at representing a more realistic global pattern of oceanic and sedimentary δ^{30}Si distributions and revealing possible controlling mechanisms via a modeling approach.

Chapter 2

Model Description

To simulate the biogeochemical cycle and isotopic composition of silicon, we applied the Hamburg Ocean Carbon Cycle Model, version 5.1 (HAMOCC5.1) (*Six and Maier-Reimer*, 1996), which includes an interactive sediment module (*Heinze et al.*, 1999), coupled with an Ocean General Circulation Model (OGCM), the Max Planck Institute global Ocean/Sea-Ice Model (MPI-OM) (*Marsland et al.*, 2003). The biogeochemical model is set up as a subroutine of the OGCM, therefore it has the same horizontal and vertical resolution and the same time steps as the OGCM.

2.1 The ocean circulation model

The Ocean General Circulation Model used for this work is the Max-Planck-Institute global Ocean/Sea-Ice Model (MPI-OM) (*Marsland et al.*, 2003). It is based on the primitive equations that represent thermodynamic processes. The model is forced by daily mean fields of heat, freshwater and momentum fluxes, provided by the German Ocean Model Intercomparison Project (OMIP) (`http://www.omip.zmaw.de`). The spatial discretization with an orthogonal curvilinear C-grid results in an average horizontal resolution of 6 °. It has 20 vertical levels with level thickness increasing with depth. The time step is three hours. The model bathymetry was created by interpolation of the ETOPO-5 dataset (Data Announcement 88-MGG-02, Digital relief of the Surface of the Earth. NOAA, National Geophysical Data Center, Boulder, Colorado, 1988) to the model grid. A detailed description of MPI-OM can be found online (`http://www.mpimet.mpg.de/en/science/models/mpiom.html`).

2.1.1 Ocean primitive equations

The model solves conservation equations for momentum, mass, heat and salinity under assumptions such as the Boussinesq approximation and the hydrostatic approximation. The momentum balance is based on the Navier-Stokes equation, but modified for a hydrostatic Boussinesq fluid on a rotating sphere. The horizontal momentum balance is described as

$$\frac{D\vec{V}_0}{Dt} + f(\vec{k} \times \vec{V}_0) = -\frac{1}{\rho_w}[\vec{\nabla}_H(p + \rho_w g\zeta)] + \vec{F}_H + \vec{F}_V \tag{2.1}$$

where D/Dt stands for the material derivative, $\vec{V}_0 = (u_0, v_0)$ is the horizontal velocity vector, t is the time, f is the Coriolis parameter, $\vec{k}$ is a unit vector normal to the earth's surface, ρ_w is a constant reference density, $\vec{\nabla}_H$ is the horizontal gradient operator, p is the internal pressure, g is the acceleration due to gravity and ζ is the sea surface elevation. $\vec{F}_H$ and $\vec{F}_V$ are horizontal and vertical eddy momentum fluxes that are parameterized assuming an eddy viscosity.

The vertical velocity is calculated from the horizontal velocity field under incompressibility condition.

$$\frac{\partial w_0}{\partial z} = -\vec{\nabla}_H \cdot \vec{V}_0 \tag{2.2}$$

Density ρ is a function of potential temperature (θ), salinity (S) and pressure (p), using the international equation of state endorsed by the Joint Panel on Oceanographic Tables and Standards (*Fofonoff and Millard*, 1983).

$$\rho = \rho(\theta, S, p) \tag{2.3}$$

Pressure p is calculated using the hydrostatic equation.

$$\frac{\partial p}{\partial z} = -g\rho \tag{2.4}$$

Under the Boussinesq approximation, the continuity equation for incompressible flow is

$$\frac{d\rho}{dt} = 0 \tag{2.5}$$

Potential temperature θ and salinity S follow the advection-diffusion equations

$$\frac{d\theta}{dt} = \vec{\nabla} \cdot (\boldsymbol{K}\vec{\nabla}\theta) \tag{2.6}$$

$$\frac{dS}{dt} = \vec{\nabla} \cdot (\boldsymbol{K}\vec{\nabla}S) \tag{2.7}$$

where the tensor $\boldsymbol{K}$ is a subgridscale parameterization of horizontal and vertical diffusion.

All biogeochemical tracers are fully advected and mixed by the OGCM.

$$\frac{dC_i}{dt} = \vec{\nabla} \cdot (\boldsymbol{K}\vec{\nabla}C_i) + \lambda_i C_i + F_i(C_i, C_j) \tag{2.8}$$

where C_i and C_j denote tracers, λ_i represents tracer specific source and sink terms and F_i describes nonlinear biologically mediated interactions between different tracers.

2.1.2 Ocean subgridscale parameterizations

Subgridscale parameterizations are necessary for those processes which take place on smaller scales than the model resolution. The model includes subgridscale parameterizations for bottom boundary layer slope transport (*Legutke and Maier-Reimer*, 2002), horizontal and vertical viscosity, vertical and isopycnal diffusivity, eddy induced mixing (*Gent et al.*, 1995), and convection.

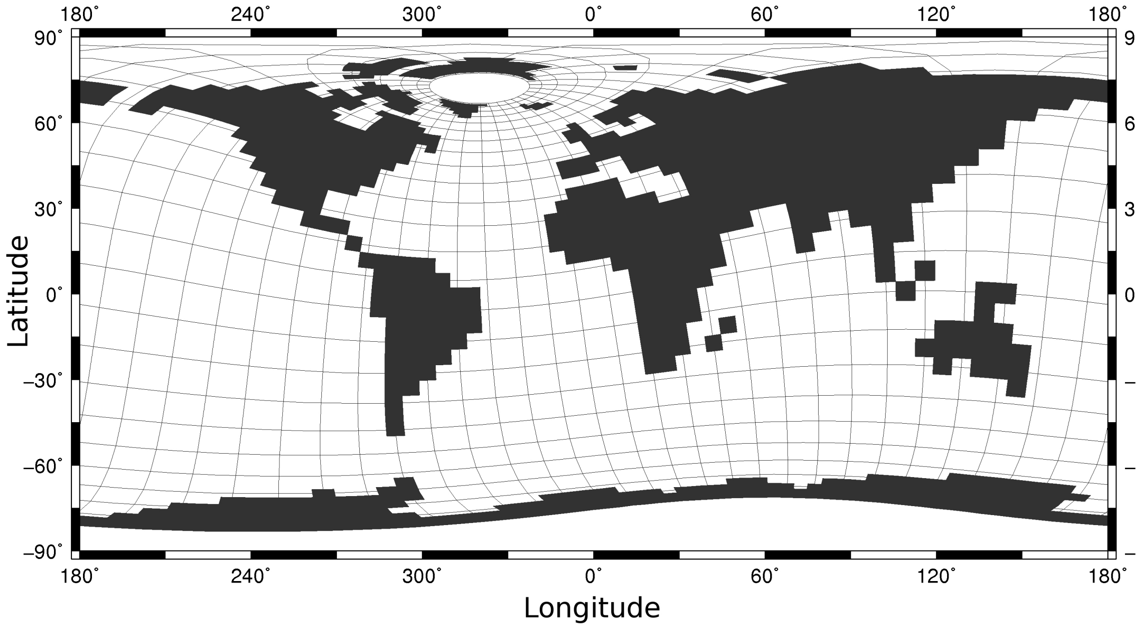

Figure 2.1: Standard MPI-OM grid orthogonal curvilinear gird for this study.

2.1.3 Model grid

The horizontal discretization of the MPI-OM is on a staggered Arakawa C-grid and the vertical discretization is on a 'z-coordinate' system. The model applies a bipolar orthogonal curvilinear coordinate system. In order to get the highest resolution near the main deep water formation regions, which are essential for thermohaline circulation (THC) and climate change, one pole is placed over Greenland and the other over Antarctica in the model (Figure 2.1). In this model setup, the horizontal resolution varies gradually between 67 km in the Arctic Ocean and about 808 km in the tropics, with a formal resolution of 6 °. The water column is divided into 20 vertical levels with four layers in the upper 90 m, representing the euphotic zone.

2.2 The biogeochemical model

The biogeochemical model HAMOCC5.1 is derived originally from the work of *Six and Maier-Reimer* (1996). HAMOCC5.1 is a complex NPZD (Nutrient Phytoplankton Zoo-

Table 2.1: Parameters used in the biological model HAMOCC5.1

Model Parameter	Value
Constant O_2:P stoichiometric ratio: $R_{\mathrm{O_2:P}}$	172 mol O_2 (mol P)$^{-1}$
Constant C:P stoichiometric ratio: $R_{\mathrm{C:P}}$	122 mol C (mol P)$^{-1}$
Constant N:P stoichiometric ratio: $R_{\mathrm{N:P}}$	16 mol N (mol P)$^{-1}$
Constant Fe:P stoichiometric ratio: $R_{\mathrm{Fe:P}}$	3.66×10^{-4} mol Fe (mol P)$^{-1}$
Global riverine input of Si	9.0 Tmol Si yr^{-1}
Global riverine input of $CaCO_3$	10.8 Tmol C yr^{-1}
Global riverine input of POC	1.1 Tmol P yr^{-1}
Half saturation constant for $Si(OH)_4$ uptake: $K_{PHY}^{\mathrm{Si(OH)_4}}$	4.0 μmol L^{-1}
Constant sinking speed of detritus: w_{DET}	5 m d^{-1}
Constant sinking speed of opal: w_{opal}	10 m d^{-1}
Constant sinking speed of $CaCO_3$: $w_{\mathrm{CaCO_3}}$	30 m d^{-1}
Opal redissolution rate constant, water column	0.01 d^{-1}
$CaCO_3$ redissolution rate constant, water column	0.075 d^{-1}
POC remineralization rate constant, water column	0.025 d^{-1}
DOC remineralization rate constant, water column	0.004 d^{-1}
$Si(OH)_4$ saturation concentration	1000 μmol L^{-1}
Opal redissolution rate constant, sediment	1.0×10^{-3} (kmol Si m^{-3})$^{-1}$ s^{-1}
$CaCO_3$ redissolution rate constant, sediment	1.0×10^{-7} (kmol C m^{-3})$^{-1}$ s^{-1}
POC remineralization rate constant, sediment	1.16×10^{-7} (kmol O m^{-3})$^{-1}$ s^{-1}
Diffusion coefficient, pore waters	1.0×10^{-9} m^2 s^{-1}
Characteristic temperature for opal dissolution: T_c	12 °C
Species dependent factor for opal dissolution: A	3.0×10^{-3} d^{-1}

plankton Detritus) model, with 5 biogeochemical tracers in the atmosphere, 25 in the water column and 19 in the sediment in the standard model setup. The interactions between the cycling of C, N, P, Fe and O_2 are simulated assuming constant stoichiometric ratios (*Redfield*, 1934), and the Si cycle is described further below. The most important model parameters are listed in Table 2.1. For a complete technical description of HAMOCC5.1, readers should refer to the model documentation by *Maier-Reimer et al.* (2005).

In the euphotic zone, phytoplankon growth depends on the availability of light and on the most limiting nutrient among phosphate, nitrate and iron, as described by a Monod type equation

$$P_{phy} = \frac{PHY \cdot J(I) \cdot X}{K_{PHY}^{\mathrm{PO_4}} + X} \tag{2.9}$$

with

$$X = min(\mathrm{PO_4}, \frac{\mathrm{NO_3}}{R_{\mathrm{N:P}}}, \frac{\mathrm{Fe}}{R_{\mathrm{Fe:P}}}). \tag{2.10}$$

Here P_{phy} denotes phytoplankton growth rate by photosynthesis (expressed in kmol P m^{-3} d^{-1}), PHY is phytoplankton biomass concentration (kmol P m^{-3}), J indicates a maximum phytoplankton growth rate (d^{-1}) under a certain availability of solar radiation I (W m^{-2}). $\mathrm{PO_4}$ (kmol P m^{-3}) and $\mathrm{NO_3}$ (kmol N m^{-3}) are concentrations of phosphate and nitrate, respectively. Fe is dissolved iron concentration (kmol Fe m^{-3}), $R_{\mathrm{N:P}}$ (mol N (mol P)$^{-1}$) and $R_{\mathrm{Fe:P}}$ (mol Fe (mol P)$^{-1}$) denote constant N:P and Fe:P stoichiometric ratios, respectively.

It is assumed that phytoplankton consists of diatoms, coccolithophorids and flagellates, although there is no explicit phytoplankton classification in the model. When silicate is available, diatom opal production is first computed proportionally to particulate organic matter production as:

$$P_{\mathrm{Si}} = min\left(\frac{\Delta DET}{\Delta t} \cdot R_{\mathrm{Si:P}} \cdot \frac{\mathrm{Si(OH)_4}}{K_{PHY}^{\mathrm{Si(OH)_4}} + \mathrm{Si(OH)_4}},\ r_{Pro} \cdot\ \mathrm{Si(OH)_4})\right), \tag{2.11}$$

where P_{Si} denotes biogenic opal production rate (kmol Si m^{-3} d^{-1}), $\Delta DET/\Delta t$ denotes particulate organic matter production rate (kmol P m^{-3} d^{-1}), $R_{\mathrm{Si:P}}$ is biogenic opal to organic matter production ratio (mol Si (mol P)$^{-1}$), $K_{PHY}^{\mathrm{Si(OH)_4}}$ indicates half saturation constant for $\mathrm{Si(OH)_4}$ uptake (kmol Si m^{-3}) and r_{Pro} is a rate constant (d^{-1}) for opal production under silicic acid non-limiting conditions. The remaining fraction of the particulate organic matter production is associated with calcareous shells production by coccolithophorides described as:

$$P_{\mathrm{Ca}} = \frac{\Delta DET}{\Delta t} \cdot R_{\mathrm{Ca:P}} \cdot \frac{K_{PHY}^{\mathrm{Si(OH)_4}}}{K_{PHY}^{\mathrm{Si(OH)_4}} + \mathrm{Si(OH)_4}}, \tag{2.12}$$

where P_{Ca} denotes biogenic $\mathrm{CaCO_3}$ production rate (kmol C m^{-3} d^{-1}) and $R_{\mathrm{Ca:P}}$ is biogenic $\mathrm{CaCO_3}$ to organic matter production ratio (mol C (mol P)$^{-1}$).

Dissolution of opaline frustules proceeds according to a temperature dependent function (*Kamatani*, 1982) as:

$$r = A \cdot exp(T/T_c), \tag{2.13}$$

where r indicates diatom opal dissolution rate (d^{-1}). A denotes a species dependent factor in nature, but in the model it is a constant that has been tuned within the range given by *Kamatani* (1982) such that the model presents the most realistic vertical distribution of silicic acid. T ($^\circ$C) denotes temperature and T_c ($^\circ$C) stands for critical temperature which is calculated according to Arrhenius equation.

Dissolved iron is provided by dust release in the ocean surface layer. Following *Johnson et al.* (1997) dissolved iron forms complexes with a strong iron-binding ligand that is present at 0.6 nmol L^{-1} throughout the ocean. Above this concentration, dissolved iron is scavenged strongly, so that its deep ocean concentration is nearly uniform at 0.6 nmol L^{-1}.

2.3 The sediment model

Particles (organic detritus, opal, calcium carbonate and dust) settle down through the water column with constant sinking speeds (see Table 1) and are being remineralized and dissolved on the way downwards. Those particles that have escaped degradation reach the ocean floor. Together with nutrient concentrations in the bottom ocean layer, these fluxes become the upper boundary condition for the sediment model. The sediment model (*Heinze et al.*, 1999) simulates particle accumulation, decomposition of detritus, redissolution of opal and calcium carbonate and the vertical diffusion of pore water tracers. The simultaneous dissolution and diffusion processes are calculated by an implicit approach. The model contains 12 biologically active sediment layers with increasing layer thickness and decreasing porosity from top to bottom. The prescribed porosity remains constant over the integration time. To maintain this porosity profile, the particulate matter is shifted downwards and stored in an additional diagenetically consolidated layer (the 13th layer), representing the materials that leave the ocean biogeochemical cycle for the burial. At model steady state, this mass loss of the whole ocean-sediment system is balanced by riverine input. Upward shifting occurs when the sediment porosity falls below the prescribed value, for example, when sea-ice forms at the surface and production of particulate matter in the water column stops. In this case, there is no deposition of particulate material onto the sediment, while the dissolution and decomposition in the sediment continues. The cases leading to upward or downward transfer in the sediment are illustrated in Figure 2.2.

2.4 Silicon isotopic fractionation

In order to investigate the δ^{30}Si distribution, we incorporated the cycling of the silicon isotope ^{30}Si into HAMOCC5.1 in addition to that of total Si (the sum of the stable isotopes ^{28}Si, ^{29}Si and ^{30}Si) which already existed in the model. The heavier isotope ^{30}Si is fractionated against during diatom opal production and potentially also during dissolution of diatom frustules as follows:

$$P^{t}_{^{30}\mathrm{Si}} = P^{t}_{\mathrm{Si}} \cdot \alpha_1 \cdot \frac{[^{30}\mathrm{Si(OH)_4}]^{t-1}}{[\mathrm{Si(OH)_4}]^{t-1}} \tag{2.14}$$

$$D^{t}_{^{30}\mathrm{Si}} = D^{t}_{\mathrm{Si}} \cdot \alpha_2 \cdot \frac{[\mathrm{B}^{30}\mathrm{Si}]_{t-1}}{[\mathrm{BSi}]_{t-1}} \tag{2.15}$$

where t and $t-1$ are consecutive time levels. P_{Si} and $P_{^{30}\mathrm{Si}}$ are biogenic Si and ^{30}Si production rates (kmol Si m^{-3} d^{-1}), respectively, and $\alpha_1 = 0.9989$ (*De La Rocha et al.*, 1997) denotes the fractionation factor for biogenic Si production. D_{Si} and $D_{^{30}\mathrm{Si}}$ are the dissolution rates (kmol Si m^{-3} d^{-1}) of biogenic Si and ^{30}Si, respectively, and α_2 is either equal to 1 (in Chapter 3, assuming no fractionation during BSi dissolution) or equal to 0.99945 (*Demarest et al.*, 2009) (in Chapter 4, assuming fractionation during BSi dissolution).

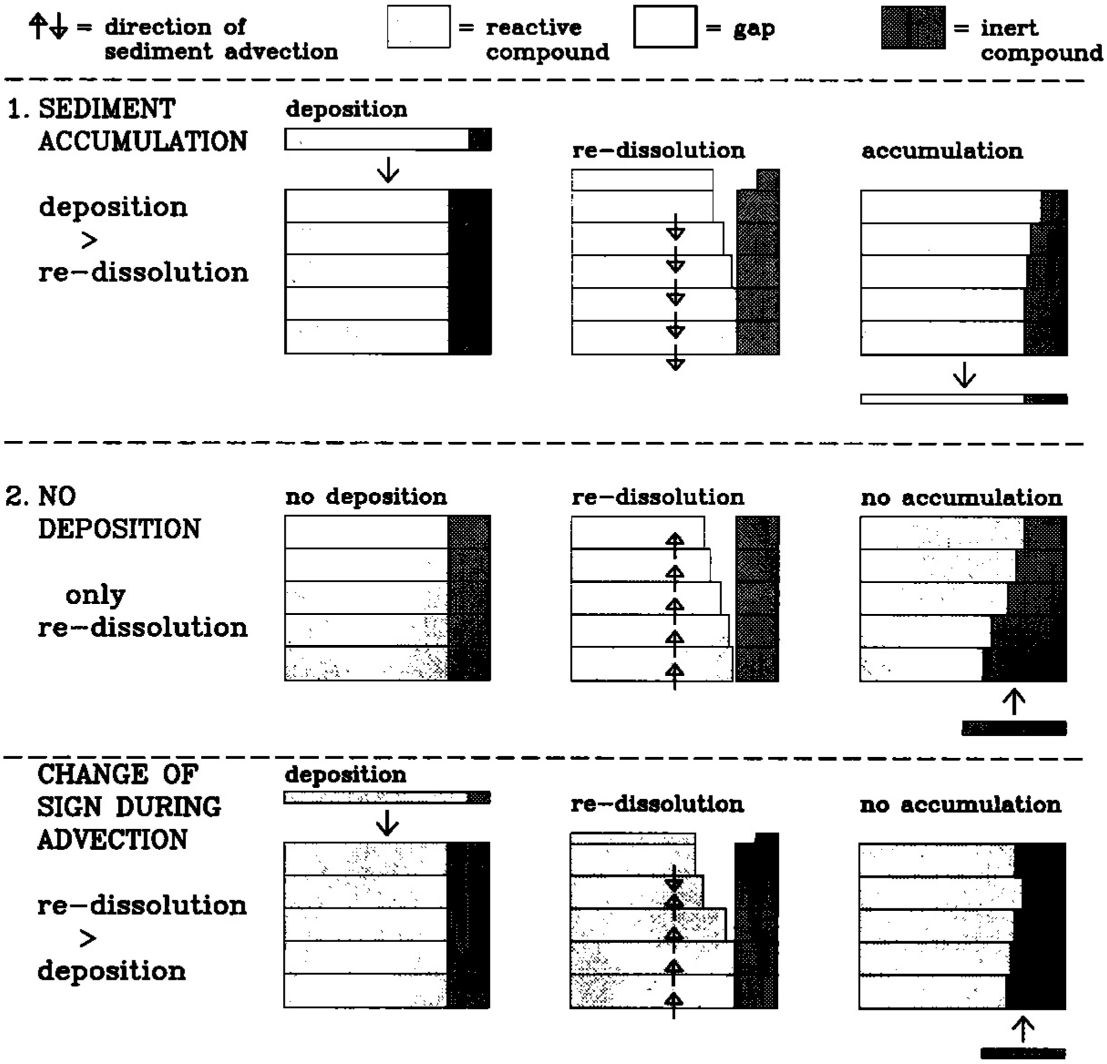

Figure 2.2: Schematic of the three cases for vertical sediment advection and sediment accumulation, taken from *Heinze et al.* (1999). (1) Sediment accumulation takes place. (2) No deposition. (3) Change of advection direction within the bioturbated zone. Here only two different solid compounds (one chemically reactive and one inert component) and five layers are shown for simplicity.

Equations 2.14 and 2.15 are derived as follows (taking the equation 2.14 as example). The fractionation factors are defined as:

$$^{29}\alpha = \frac{^{29}R_{\mathrm{BSi}}}{^{29}R_{\mathrm{DSi}}} \tag{2.16}$$

$$^{30}\alpha = \frac{^{30}R_{\mathrm{BSi}}}{^{30}R_{\mathrm{DSi}}}, \tag{2.17}$$

where ^{29}R and ^{30}R stand for the isotope ratios $^{29}\mathrm{Si}/^{28}\mathrm{Si}$ and $^{30}\mathrm{Si}/^{28}\mathrm{Si}$ of the biogenic and dissolved Si, respectively. The above equations can be transformed to:

$$\frac{\Delta \mathrm{B}^{29}\mathrm{Si}}{\Delta \mathrm{B}^{28}\mathrm{Si}} = {^{29}\alpha}\,\frac{^{29}\mathrm{Si}}{^{28}\mathrm{Si}} = {^{29}\alpha}\,\frac{^{29}\mathrm{Si}}{\mathrm{Si} -^{29}\mathrm{Si} -^{30}\mathrm{Si}} = B \tag{2.18}$$

$$\frac{\Delta \mathrm{B}^{30}\mathrm{Si}}{\Delta \mathrm{B}^{28}\mathrm{Si}} = {^{30}\alpha}\,\frac{^{30}\mathrm{Si}}{^{28}\mathrm{Si}} = {^{30}\alpha}\,\frac{^{30}\mathrm{Si}}{\mathrm{Si} -^{29}\mathrm{Si} -^{30}\mathrm{Si}} = A. \tag{2.19}$$

Here, the Δ notation indicates the newly formed silica rather than the bulk silica that has accumulated previously. In principle, the isotopic fractionation of the two minor stable isotopes are thus coupled. The question therefore is, whether it is possible to eliminate the isotope $^{29}\mathrm{Si}$ from the equations and construct a model for only $^{30}\mathrm{Si}$ and total Si. To this end we replace the $^{28}\mathrm{Si}$ by subtraction of $^{29}\mathrm{Si}$ and $^{30}\mathrm{Si}$ from the total Si and the same with $\mathrm{B}^{28}\mathrm{Si}$:

$$\mathrm{B}^{28}\mathrm{Si} = \mathrm{BSi} - \mathrm{B}^{29}\mathrm{Si} - \mathrm{B}^{30}\mathrm{Si}. \tag{2.20}$$

We further transform Equations 2.18 and 2.19 to two simultaneous linear equations:

$$\Delta \mathrm{B}^{29}\mathrm{Si} = \mathrm{B}\left(\mathrm{BSi} - \mathrm{B}^{29}\mathrm{Si} - \mathrm{B}^{30}\mathrm{Si}\right) \tag{2.21}$$

$$\Delta \mathrm{B}^{30}\mathrm{Si} = \mathrm{A}\left(\mathrm{BSi} - \mathrm{B}^{29}\mathrm{Si} - \mathrm{B}^{30}\mathrm{Si}\right) \tag{2.22}$$

which have the solution

$$\Delta \mathrm{B}^{29}\mathrm{Si} = \frac{\mathrm{B}}{1 + \mathrm{A} + \mathrm{B}} \Delta \mathrm{BSi} \tag{2.23}$$

$$\Delta \mathrm{B}^{30}\mathrm{Si} = \frac{\mathrm{A}}{1 + \mathrm{A} + \mathrm{B}} \Delta \mathrm{BSi}. \tag{2.24}$$

The expressions in the fractions can be evaluated using the definitions of A and B. We obtain thus

$$\Delta \mathrm{B}^{29}\mathrm{Si} = \frac{{}^{29}\alpha^{29}\mathrm{Si}}{\mathrm{Si} - (1 -^{29} \alpha)^{29}\mathrm{Si} - (1 -^{30} \alpha)^{30}\mathrm{Si}} \Delta \mathrm{BSi} \tag{2.25}$$

$$\Delta \mathrm{B}^{30}\mathrm{Si} = \frac{{}^{30}\alpha^{30}\mathrm{Si}}{\mathrm{Si} - (1 -^{29} \alpha)^{29}\mathrm{Si} - (1 -^{30} \alpha)^{30}\mathrm{Si}} \Delta \mathrm{BSi}. \tag{2.26}$$

Based on the fact that the numbers (1-$^{29}\alpha$) and (1-$^{30}\alpha$) are on the order of 10^{-3} and usually ^{29}Si and ^{30}Si are much smaller than the total Si, we can approximate the Equation 2.26 by

$$\Delta \mathrm{B}^{30}\mathrm{Si} = \frac{{}^{30}\alpha^{30}\mathrm{Si}}{\mathrm{Si}} \Delta \mathrm{BSi}. \tag{2.27}$$

This equation is actually the same as Equation 2.14.

2.5 Model initialization and riverine input

The oceanic silicic acid distribution is initialized with a profile obtained by averaging the World Ocean Atlas 2009 (WOA09) dataset horizontally (*Garcia et al.*, 2010) (`http://www.nodc.noaa.gov/cgi-bin/OC5/WOA09/woa09.pl`). According to the in situ measurements given by *De La Rocha et al.* (2000), we initialized the $\delta^{30}\mathrm{Si}_{\mathrm{DSi}}$ and $\delta^{30}\mathrm{Si}_{\mathrm{BSi}}$ with homogeneous values of +1.1‰ and +1.0‰, respectively.

The riverine input of Si, in form of silicic acid, is evenly supplied in the model over the whole ocean surface every model time step with a uniform isotopic composition of +0.8‰ (*De La Rocha et al.*, 2000). Although detailed distributions of riverine silicate input to coast zone have been published (*Bernard et al.*, 2011; *Dürr et al.*, 2011), a comprehensive dataset of δ^{30}Si of the input is not available yet. Our Si input pattern is therefore only an approximation of the real pattern, which varies both spatially and seasonally (*Georg et al.*, 2006).

Chapter 3

Modeling Results I: fractionation during biogenic silica production

In this chapter, we present a first set of modeling results, where we assume that Si fractionation only happens during the formation of diatom frustules but not during their dissolution.

3.1 Silicate distribution

The model is in a quasi-steady state after running for 10,000 model years. By then the globally averaged oceanic concentration of silicic acid is 82 μmol L^{-1}, which is in close agreement with the estimate of *Sarmiento and Gruber* (2006) of 84 μmol L^{-1} and falls between the estimate of *Tréguer and De La Rocha* (2013) of ∼75 μmol L^{-1} and that of the WOA09 dataset of 92 μmol L^{-1} (*Garcia et al.*, 2010).

In surface waters of the subtropical gyres the silicic acid concentrations are usually lower than 2 μmol L^{-1}, while in the Southern Ocean the surface concentrations are as high as 80 to 100 μmol L^{-1} (*Tréguer et al.*, 1995). Large-scale measured and modeled annual mean surface silicic acid concentrations agree with each other (Figure 3.1). The major discrepancies occur in the North Pacific subpolar gyre and the Southern Ocean.

The physical model tends to overestimate the stratification in the North Pacific, in other words, it underestimates the vertical mixing especially in winter time, which results in a lower surface silicic acid concentration than observations. This insufficient representation of nutrient distributions in the North Pacific subpolar gyre has been also reported in other coarse resolution models (*Six and Maier-Reimer*, 1996; *Aumont et al.*, 2003; *Wischmeyer et al.*, 2003). Another reason might be the lower concentration in the deep North Pacific (Figure 3.3e) that upwells to the surface. In the Southern Ocean, the lower silicic acid concentration south of 60 °S shown in Figure 3.1c very likely results from the lower concentration in the Circumpolar Deep Water (Figure 3.3) which upwells to the surface. The band of higher concentration in the model north of 60 °S, however, is mainly caused by a broader Circumpolar Current due to the high diffusivity of this coarse resolution model. Moreover, the Si:N drawdown ratio by diatoms is not regulated by iron limitation in our model, which leads to an underestimate of Si uptake in the Southern Ocean surface water where iron is limited (*Dunne et al.*, 2007).

The deep concentration of silicic acid is much higher (globally averaged 102.3 μmol L^{-1} at 3000 m depth in the model) than that in the surface waters (globally averaged 10.4 μmol L^{-1}). It increases along the pathway of the conveyor belt from 55.2 μmol L^{-1} averaged in the deep North Atlantic, to 91.7 μmol L^{-1} in the deep Antarctic, eventually to 128.5 μmol L^{-1} in the deep North Pacific (Figure 3.2).

The silicic acid concentration exhibits a very large vertical gradient compared to other macro-nutrients (e.g. nitrate and phosphate) and the maximum concentration of silicic acid occurs at a much deeper depth in the Pacific. This can be explained by the more efficient export of silica to the deep ocean than e.g. nitrate ("the silicate pump" *Dugdale et al.* (1995)) and silica dissolution taking place on average at greater depths than remineralization of organic matter. As we can see from Figure 3.3, the modeled vertical distribution of DSi exhibits typical patterns of observed DSi distribution within different water masses. High concentrations occur in the north deep Pacific and the Circumpolar Deep Water with a high concentration tongue spreading northward from the Southern

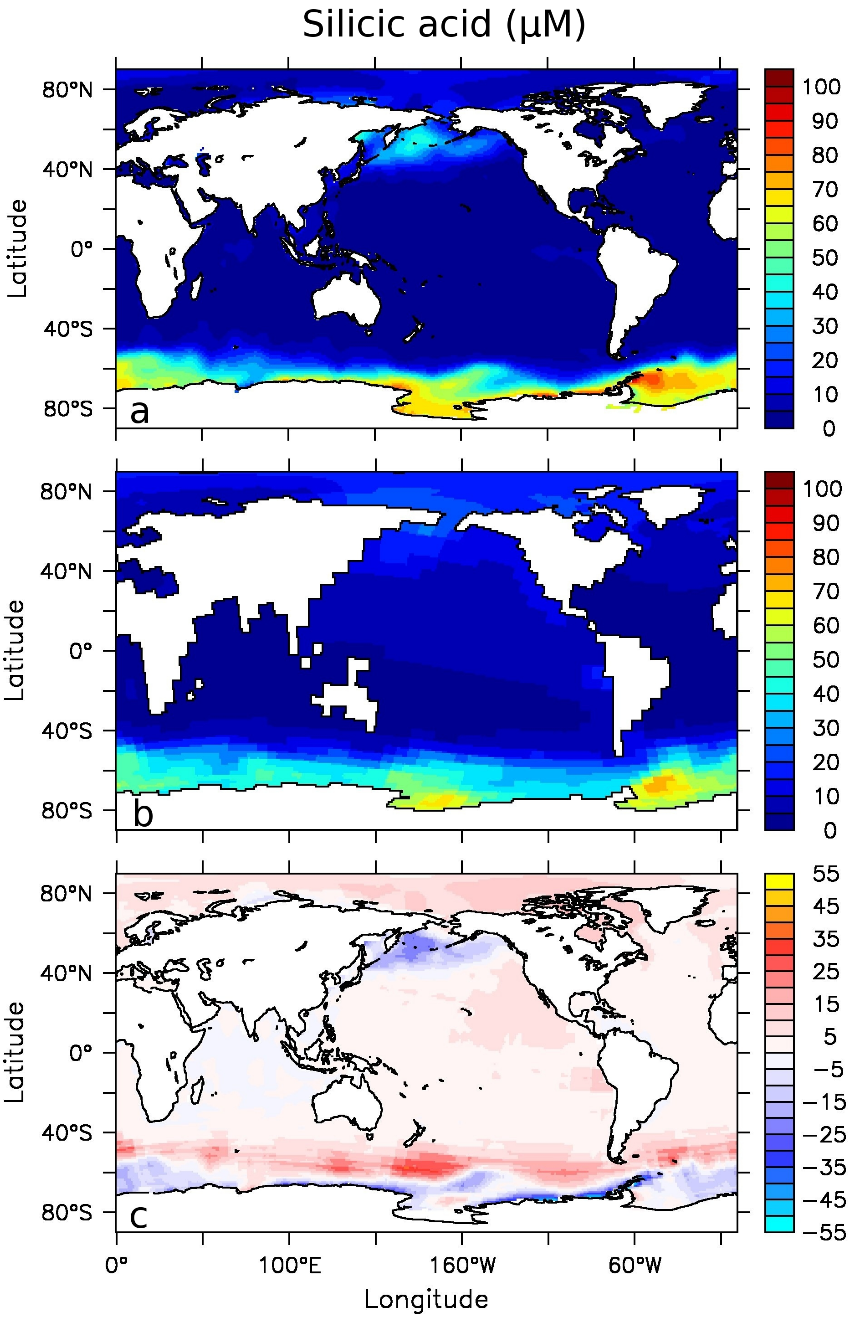

Figure 3.1: Annual mean surface silicic acid concentrations (μmol L^{-1}) from (a) World Ocean Atlas 2009 dataset, (b) our model result, (c) difference between the modeled and observed concentrations.

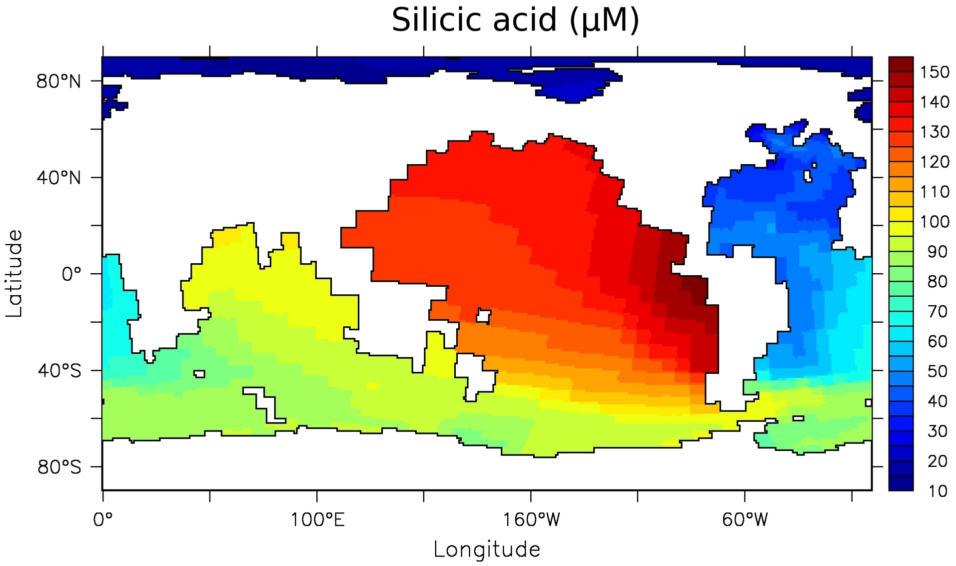

Figure 3.2: Annual mean silicic acid concentrations (μmol L^{-1}) at 3000 m depth.

Ocean representing the Antarctic Intermediate Water. However, the coarse resolution OGCM tends to underestimate the volume of the North Atlantic Deep Water and to overpredict the extent of spreading of Antarctic Bottom Water to the North Atlantic (Figure 3.3b).

3.2 Carbon and biogenic opal export

The global total particulate organic carbon (POC) and biogenic opal (BSi) that get exported cross 90 m depth by sinking of dead organic matter and inorganic shells in the model are 10.3 Pg C yr^{-1} and 118 Tmol Si yr^{-1}, respectively, which are in close accordance with *Sarmiento and Gruber* (2006)'s estimation of 9.8 Pg C yr^{-1} and 104 Tmol Si yr^{-1}. The opal export of 118 Tmol Si yr^{-1} falls also in the estimated range of 88-122 Tmol Si yr^{-1} given by *Tréguer and De La Rocha* (2013). The horizontal distributions of POC and BSi export fluxes are comparable with the estimates of *Sarmiento and Gruber* (2006), shown in Figure 3.4.

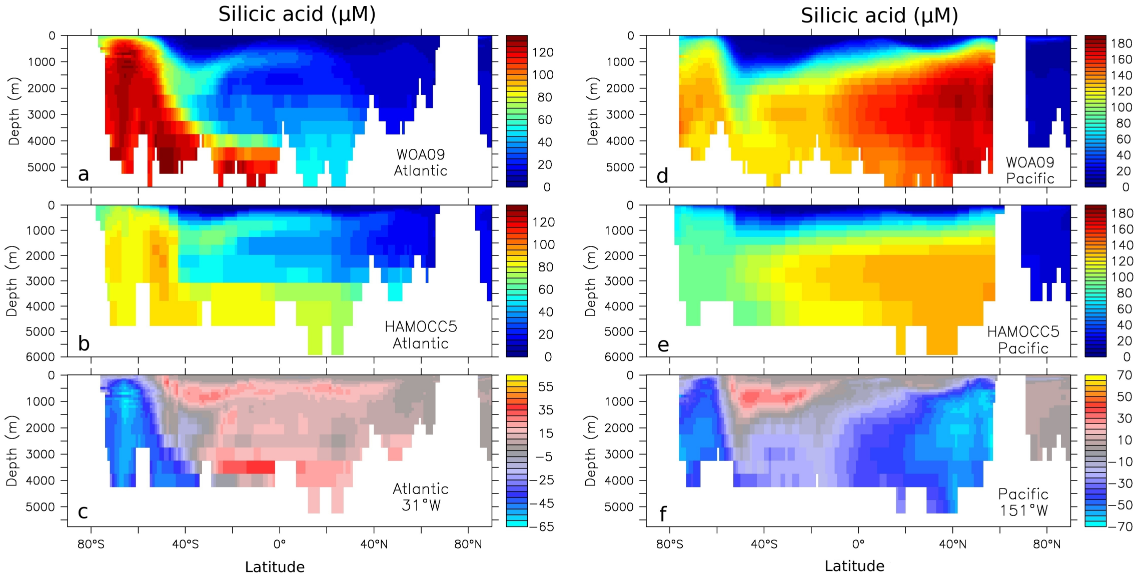

Figure 3.3: Annual mean silicic acid concentrations (μmol L^{-1}) through an Atlantic section (31 °W) and a Pacific section (151 °W), with World Ocean Atlas 2009 (WOA09) data set (a, d), our model results (b, e) and the difference between the WOA09 and modeled concentrations (c, f).

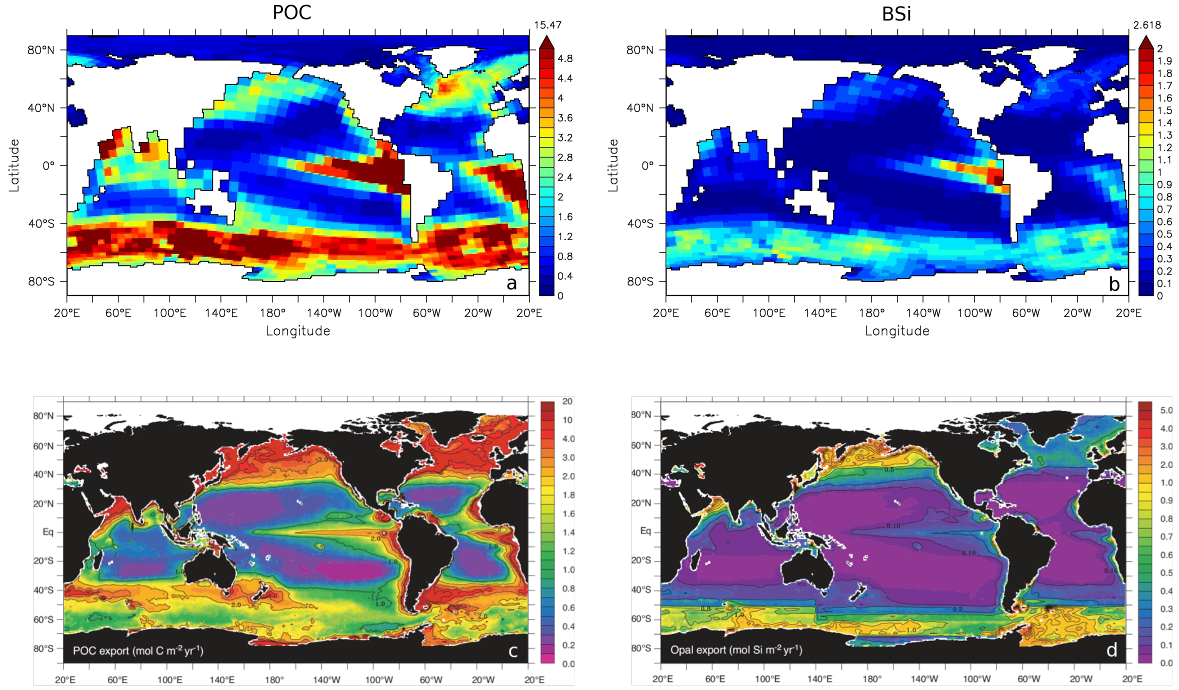

Figure 3.4: Particulate organic carbon export (mol C m^{-2} yr^{-1}) (a, c) and biogenic opal export (mol Si m^{-2} yr^{-1}) (b, d) at 90 m depth of the model result (a, b) and of the estimation of *Sarmiento and Gruber* (2006) (c, d).

3.3 The δ^{30}Si distribution

3.3.1 The δ^{30}Si distribution in the surface ocean

The annual average value of $\delta^{30}\mathrm{Si}_{\mathrm{DSi}}$ in the upper 90 m ranges from +1.20 to +3.15‰ with the higher values occurring in the subtropical gyres (Figure 3.5a), where silicic acid is depleted. The pattern of the surface $\delta^{30}\mathrm{Si}_{\mathrm{DSi}}$ distribution agrees to a great extent with the model result of *Wischmeyer et al.* (2003). However, the maximal $\delta^{30}\mathrm{Si}_{\mathrm{DSi}}$ value in our simulation is notably smaller than the ∼6‰ given by *Wischmeyer et al.* (2003). This can be attributed to our more moderate biogenic opal export production crossing 90 m depth (118 Tmol Si yr^{-1}) compared to the 177 Tmol Si yr^{-1} reported by *Wischmeyer et al.* (2003), which would lead to a stronger magnitude of Rayleigh distillation due to more silicic acid drawdown in their model (see section 3.4.3).

The pattern of averaged δ^{30}Si of biogenic opal over the upper 90 m is very similar to that of $\delta^{30}\mathrm{Si}_{\mathrm{DSi}}$, but the absolute values range from +0.15 to +1.95‰ (Figure 3.5b). Interestingly, the difference between $\delta^{30}\mathrm{Si}_{\mathrm{BSi}}$ and $\delta^{30}\mathrm{Si}_{\mathrm{DSi}}$ is mostly around -1.1‰, which is the constant fractionation factor used in the model, or is somewhat lower (between -1.1‰ and -0.4‰) except in a few regions (Figure 3.5c). The areas where the (absolute) difference is smaller than 1.1‰ are all the central upwelling or deep water formation regions, where the surface waters are rapidly replaced by deep or surrounding water masses with lighter isotopic signature. Therefore, the difference between $\delta^{30}\mathrm{Si}_{\mathrm{BSi}}$ and $\delta^{30}\mathrm{Si}_{\mathrm{DSi}}$ in these regions seems smaller due to the constant replacement of silicic acid with lighter δ^{30}Si signature. Our findings agree with previous studies as the biological fractionation during BSi production and physical mixing are two essential factors for controlling δ^{30}Si distribution in surface waters (*Cardinal et al.*, 2005; *Reynolds et al.*, 2006; *Beucher et al.*, 2008, 2011).

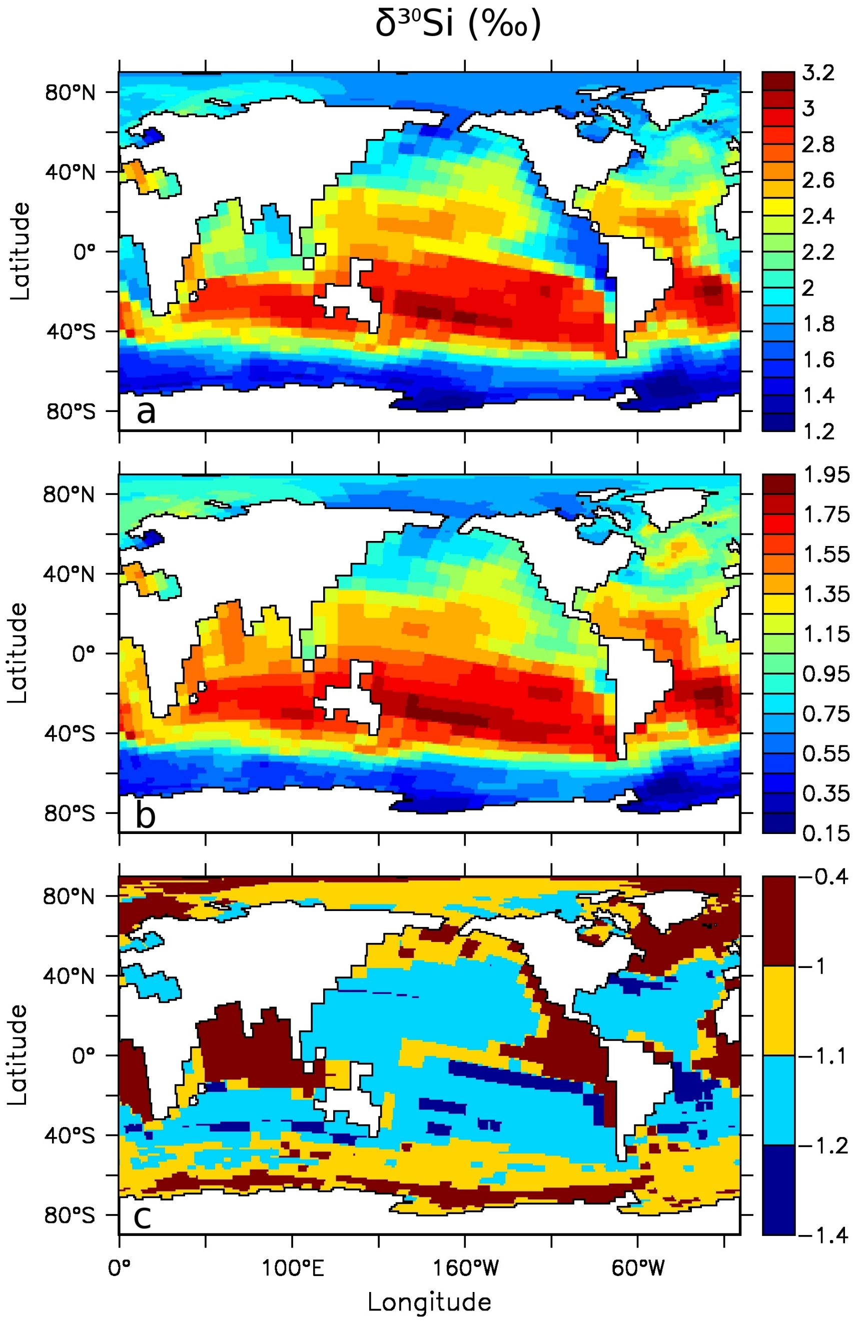

Figure 3.5: (a) The δ^{30}Si of silicic acid (‰) and (b) δ^{30}Si of biogenic opal (‰) in the surface ocean and (c) the difference between (b) and (a). Note the non-linear color scaling in the lower panel.

3.3.2 Seasonal variations of δ^{30}Si$_{\mathrm{DSi}}$

The model shows a distinct seasonal pattern of surface δ^{30}Si$_{\mathrm{DSi}}$ especially in high latitudes (Figure 3.6). In the Northern Hemisphere north of ∼40 °N, sea surface δ^{30}Si$_{\mathrm{DSi}}$ reaches lowest values in March and highest in September, while in the Southern Hemisphere (south of ∼40 °S) it is the opposite. The difference in δ^{30}Si$_{\mathrm{DSi}}$ between winter and summer can reach up to 0.7‰ both in the North Atlantic and in the Southern Ocean (Figure 3.7). Taking the North Atlantic as example, the winter mixed layer reaches its deepest depth around March (Figure 3.8a), which brings nutrient-enriched water with lighter δ^{30}Si$_{\mathrm{DSi}}$ to the surface. These abundant nutrients generally lead to a diatom spring bloom that then causes a maximum biogenic opal export in May (Figure 3.8c). During the intensive utilization of silicic acid in spring, the preferential uptake of the lighter silicon isotopes elevates the δ^{30}Si$_{\mathrm{DSi}}$ in the surface water and the δ^{30}Si$_{\mathrm{DSi}}$ increases until September due to the continual uptake by diatoms and the water column stratification. In both the Northern and Southern Hemisphere, we find that the surface δ^{30}Si$_{\mathrm{DSi}}$ is seasonal-dependent inversely related to DSi concentration and mixed layer depth. Furthermore, the δ^{30}Si$_{\mathrm{DSi}}$ peaks approximately four months after the BSi export reaches its maximum, likely due to the continued uptake by diatoms and the water column stratification. This further demonstrates that the biological fractionation and the physical mixing are two major controlling factors of δ^{30}Si$_{\mathrm{DSi}}$.

3.3.3 The δ^{30}Si$_{\mathrm{DSi}}$ distribution in the deep ocean

The δ^{30}Si$_{\mathrm{DSi}}$ in the deep ocean is controlled both by advection related to the thermohaline circulation and by biological productivity in the surface ocean. Below 2000 m depth the vertical distribution of δ^{30}Si$_{\mathrm{DSi}}$ is relatively uniform with depth (Figure 3.13, 3.14). Horizontal variations of δ^{30}Si$_{\mathrm{DSi}}$ among deep-water masses have been long noted by both in situ measurements (*De La Rocha et al.*, 2000) and a box model study (*Reynolds*, 2009). A recent modeling study also shows a similar pattern (*Matsumoto et al.*, 2013).

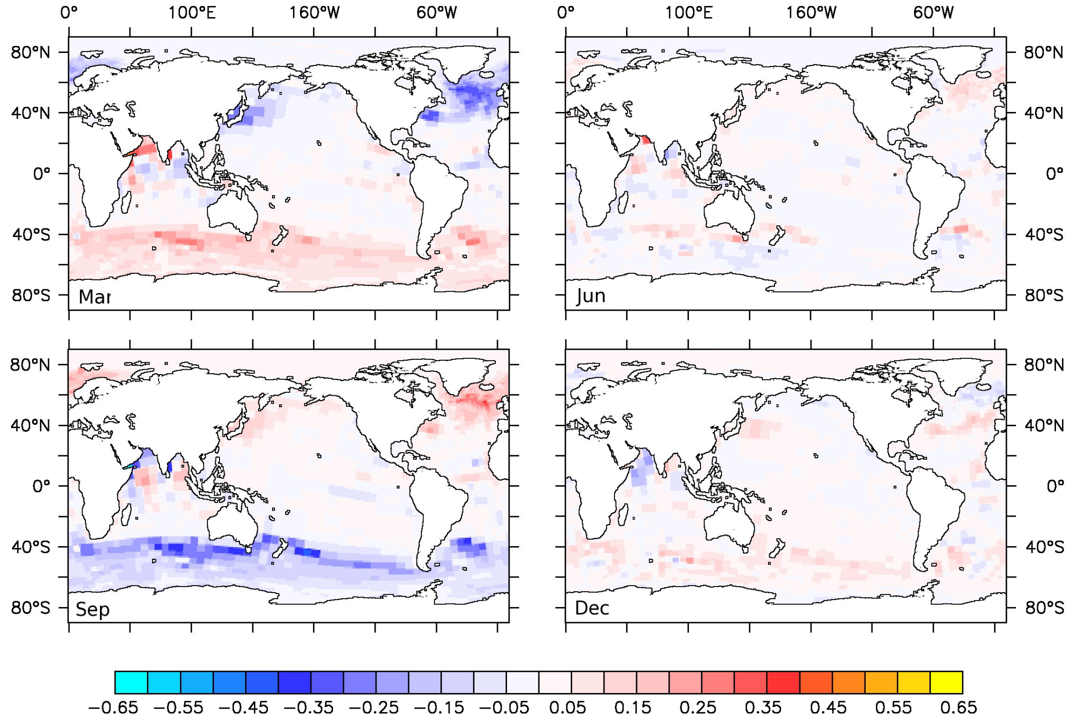

Figure 3.6: The seasonal variation of surface δ^{30}Si (‰) of silicic acid: deviation of δ^{30}Si from annual average in March, June, September and December, respectively.

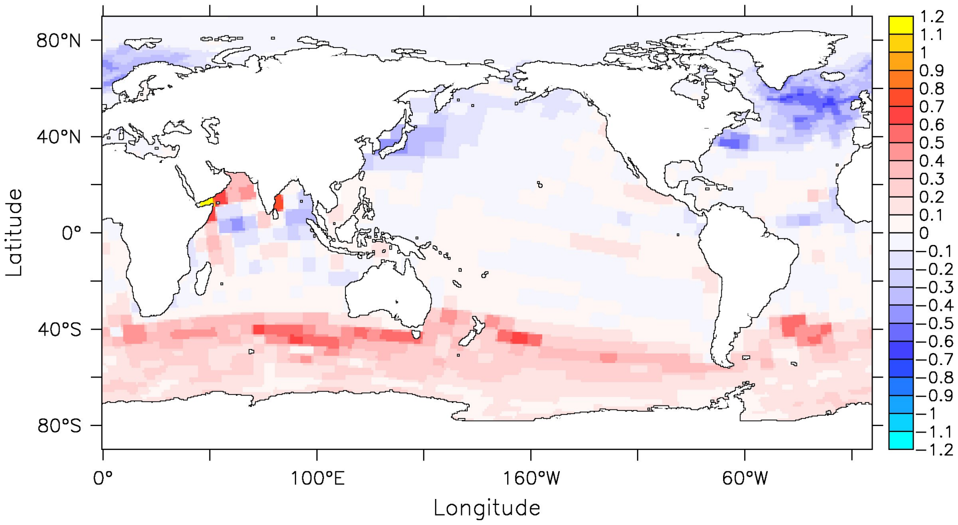

Figure 3.7: Difference in surface δ^{30}Si (‰) between March and September.

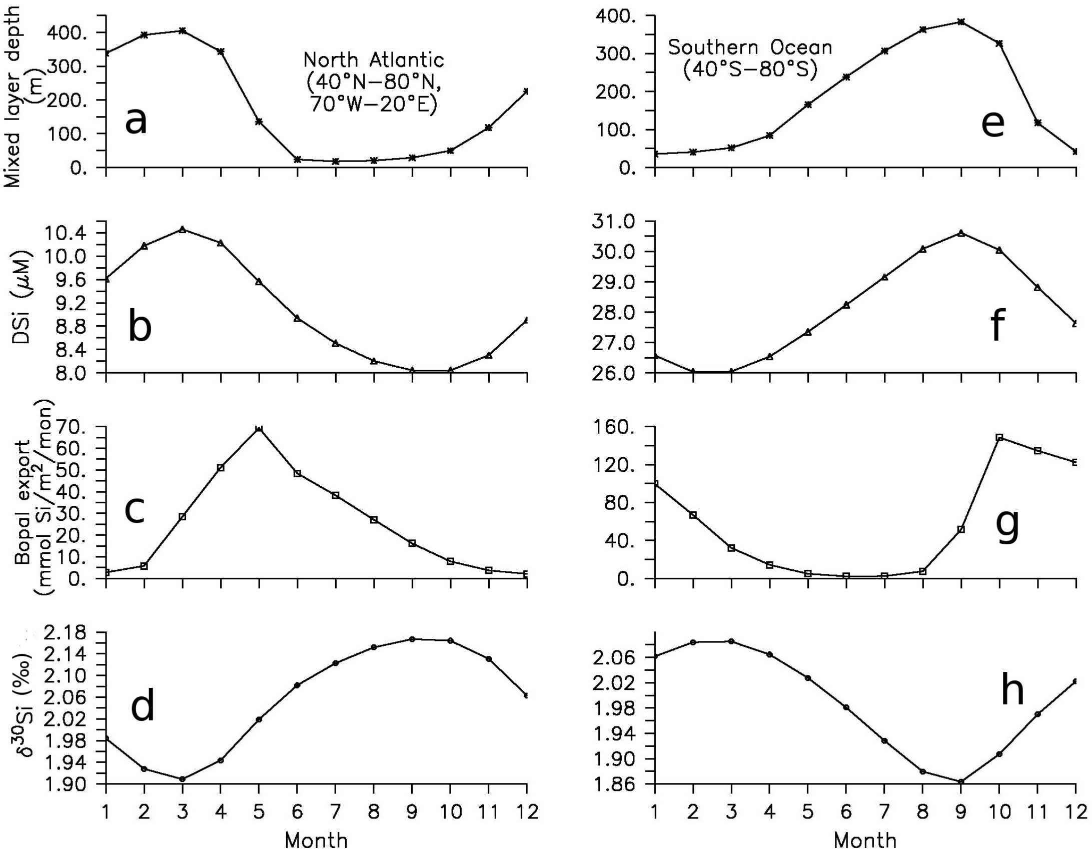

Figure 3.8: Seasonal variations of the mixed layer depth (m) (a, e), silicic acid concentration (μmol L^{-1}) (averaged in the upper 100 m water depth) (b, f), biogenic opal export (mmol Si m^{-2}) (c, g) and the δ^{30}Si (‰) of silicic acid (averaged in the upper 100 m water depth) (d, h) in the North Atlantic (a, b, c, d) and in the Southern Ocean (e, f, g, h).

Our model captures a clear decrease of deep ocean $\delta^{30}\mathrm{Si}_{\mathrm{DSi}}$ along the conveyor belt, from the North Atlantic to the North Pacific (Figure 3.9 and Figure 3.10). The $\delta^{30}\mathrm{Si}_{\mathrm{DSi}}$ below 2000 m averages +1.3‰ and +1.2‰ over large areas of the North and South Atlantic, respectively, in accordance with the measurements from *De La Rocha et al.* (2000), while in the North Pacific the average value of +1.1‰ appears higher than their reported value of +0.9‰. Nevertheless, the difference in $\delta^{30}\mathrm{Si}_{\mathrm{DSi}}$ between deep North Atlantic and deep North Pacific is between 0.1 and 0.5‰, in the neighborhood of estimations by *Reynolds* (2009) of 0.3‰ and by *De La Rocha et al.* (2000) of 0.4‰. Moreover, Figure 3.10 shows mirror-image-like relationship between deep DSi concentration and the corresponding $\delta^{30}\mathrm{Si}_{\mathrm{DSi}}$. As our model predicts higher DSi concentrations in the North Atlantic and lower concentrations in the North Pacific than seen in the WOA09 dataset (Figure 3.3c, f), we can expect in reality an even larger difference in $\delta^{30}\mathrm{Si}_{\mathrm{DSi}}$ between these two water masses. As *Reynolds* (2009) has explained, the source waters of North Atlantic Deep Water are depleted in silicic acid by diatom uptake, which leads to a relatively high $\delta^{30}\mathrm{Si}$ signature in this water mass. Dissolution of biogenic opal releases DSi with relatively lighter $\delta^{30}\mathrm{Si}$ than the surface water where the BSi is formed. Especially, dissolution of BSi which forms in the Southern Ocean under silicic acid replete conditions feeds low $\delta^{30}\mathrm{Si}$ into the deep North Pacific. The combination of preformed $\delta^{30}\mathrm{Si}_{\mathrm{DSi}}$ with a dissolution signal explains why the deep North Atlantic has a relatively higher $\delta^{30}\mathrm{Si}$ signature than the deep North Pacific.

3.3.4 The $\delta^{30}\mathrm{Si}_{\mathrm{BSi}}$ distribution in the sediment

Our model is forced by a one-year modern climatological dataset (heat, freshwater and momentum fluxes, see section 2.1) and runs into a quasi steady state so that the modeled $\delta^{30}\mathrm{Si}$ of both silicic acid and biogenic opal should represent the steady state under modern climate conditions rather than a transient state over a period of time. Given that the opal frustules sink down through the water column without significant horizontal redistribution, the pattern of $\delta^{30}\mathrm{Si}_{\mathrm{BSi}}$ on the sediment surface should reflect the $\delta^{30}\mathrm{Si}_{\mathrm{BSi}}$

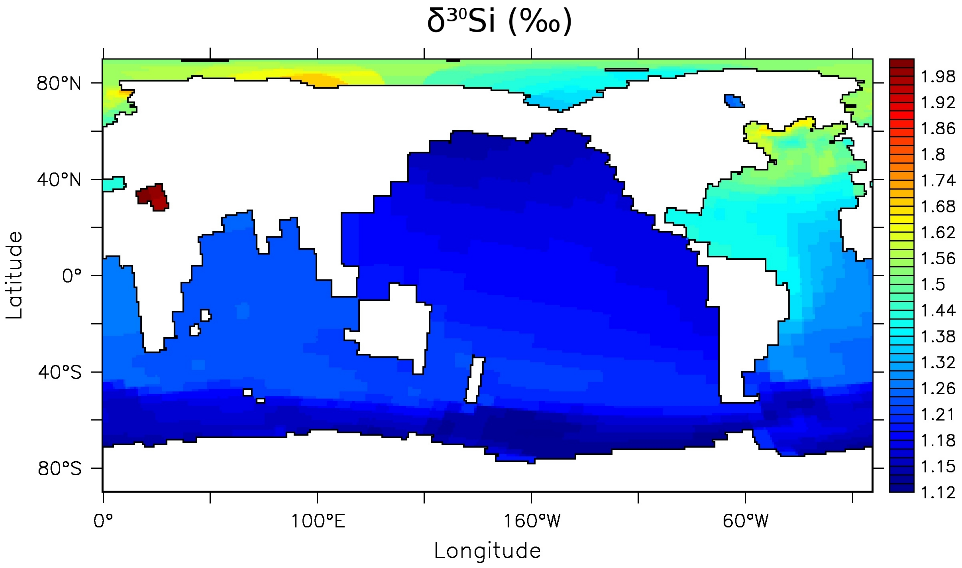

Figure 3.9: The δ^{30}Si (‰) of silicic acid at 2000 m water depth. Note the non-linear color scaling.

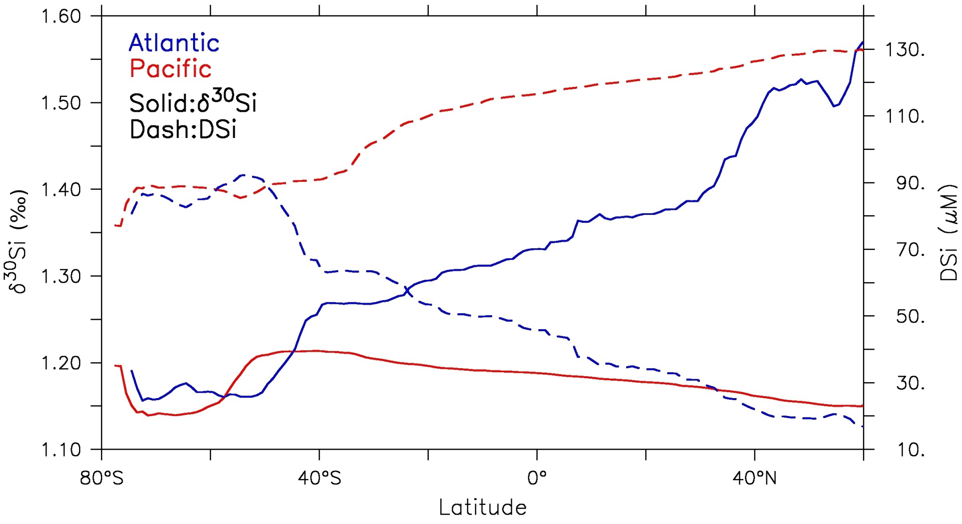

Figure 3.10: The zonal average of silicic acid concentration (dashed lines) and δ^{30}Si (‰) of silicic acid (solid lines) at 2000 m water depth both in the Atlantic basin (blue) and in the Pacific basin (red).

signature in the surface ocean. In fact, we find that the pattern of $\delta^{30}\mathrm{Si}_{\mathrm{BSi}}$ on the sediment surface is more close to the pattern of $\delta^{30}\mathrm{Si}$ of BSi that sinks out of the euphotic zone (crossing 90 m) rather than that of $\delta^{30}\mathrm{Si}_{\mathrm{BSi}}$ averaged in the upper (50 m) water layers, especially along the equator (Figure 3.5a, b, c). The difference between $\delta^{30}\mathrm{Si}_{\mathrm{BSi}}$ in upper 50 m and that crossing 90 m is shown in Figure 3.11d. The major deviation occurs in the equatorial regions where the annual average mixed layer depth is shallower than 50 m (Figure 3.12), which means that the $\delta^{30}\mathrm{Si}_{\mathrm{BSi}}$ signal that is produced in the upper 50 m is not homogenized down to 90 m and is usually higher than that in the 90 m. The $\delta^{30}\mathrm{Si}_{\mathrm{BSi}}$ distribution in the surface sediment thus mainly reflects the exported $\delta^{30}\mathrm{Si}_{\mathrm{BSi}}$ signal from the euphotic zone in the model and it is important to note that this can differ by up to 0.24‰ from what is produced in the upper water layers.

3.3.5 Vertical distributions of $\delta^{30}\mathrm{Si}_{\mathrm{DSi}}$ in the ocean

The simulated global average vertical profile of $\delta^{30}\mathrm{Si}_{\mathrm{DSi}}$ exhibits a value of ∼+2.4‰ in surface waters, where silicic acid is utilized by diatoms (Figure 3.13). The value of $\delta^{30}\mathrm{Si}_{\mathrm{DSi}}$ decreases rapidly to ∼+1.4‰ at 500 m depth, then drops further to ∼+1.2‰ below 1000 m. Our result is consistent with the recent modeling study (*Matsumoto et al.*, 2013) on the deep ocean $\delta^{30}\mathrm{Si}_{\mathrm{DSi}}$, but our globally averaged surface $\delta^{30}\mathrm{Si}_{\mathrm{DSi}}$ is lower than their value of +3‰. This is perhaps the result of the fact that surface silicic acid in our model is less depleted than in theirs. An interesting feature in Figure 3.13 is that the Atlantic Ocean has comparatively high $\delta^{30}\mathrm{Si}_{\mathrm{DSi}}$ at water depths between 500 and 3500 m, which correlates inversely with the low DSi concentrations. As we suggested before, the source water of North Atlantic Deep Water is depleted in nutrients, especially silicate, and sinks down during deep water formation with a high $\delta^{30}\mathrm{Si}_{\mathrm{DSi}}$ signature. On the other hand, the Southern Ocean has a relatively low surface $\delta^{30}\mathrm{Si}_{\mathrm{DSi}}$ (∼+2.0‰) compared to other ocean basins, due to the abundant silicic acid in the surface waters, especially south of the Antarctic Polar Front. As we can see in Figure 3.14, the vertical gradient of $\delta^{30}\mathrm{Si}_{\mathrm{DSi}}$ through the whole water column is not as pronounced as the gradient of DSi (Figure 3.3),

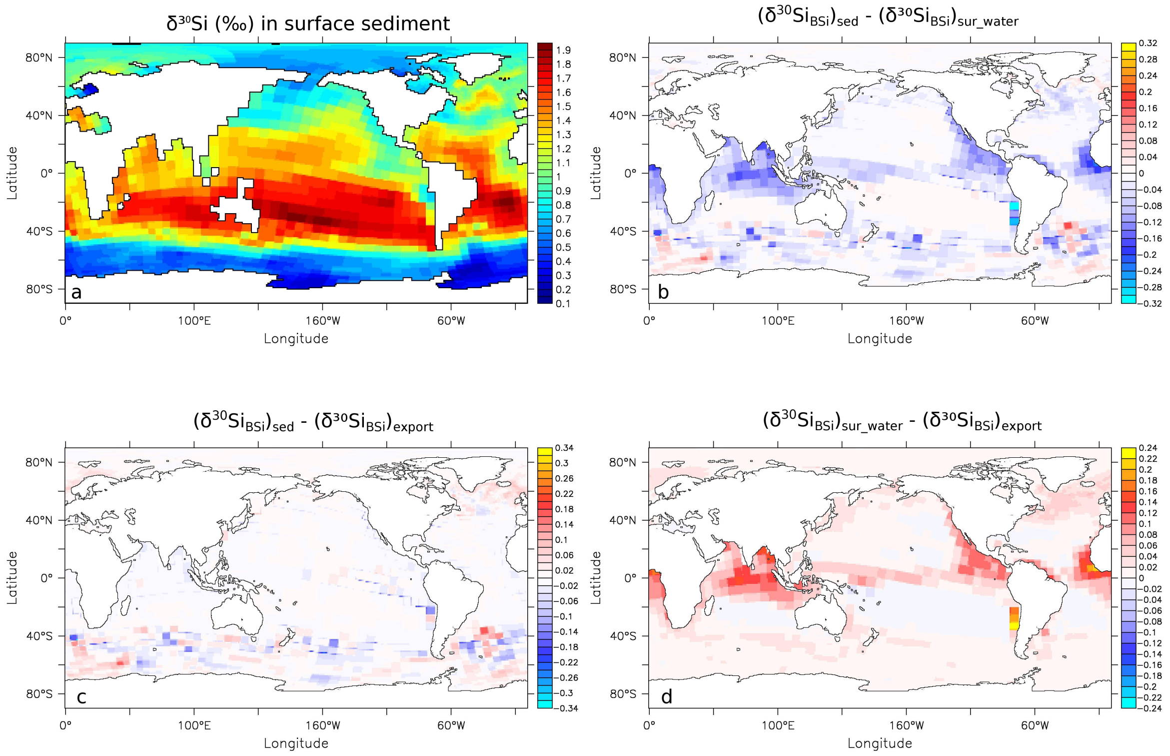

Figure 3.11: (a) The δ^{30}Si of the biogenic opal (‰) in the sediment surface layer, (b) the difference between (a) and the average δ^{30}Si of biogenic opal in the upper 50 m water column, (c) the difference between (a) and the δ^{30}Si of opal fluxes sinking out of the euphotic zone (crossing 90 m), (d) the difference between the average δ^{30}Si of biogenic opal in the upper 50 m water column and the δ^{30}Si of opal fluxes sinking out of the euphotic zone (crossing 90 m).

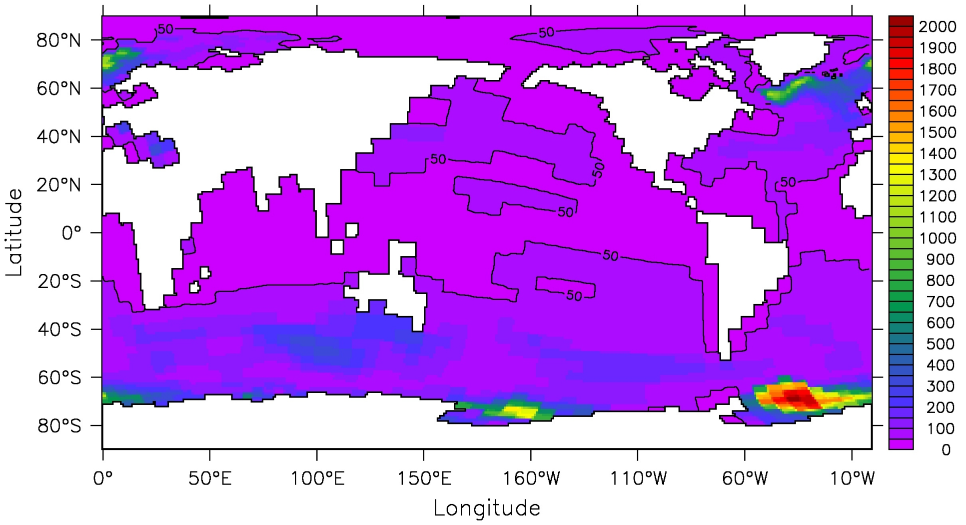

Figure 3.12: Annually averaged mixed layer depth (m).

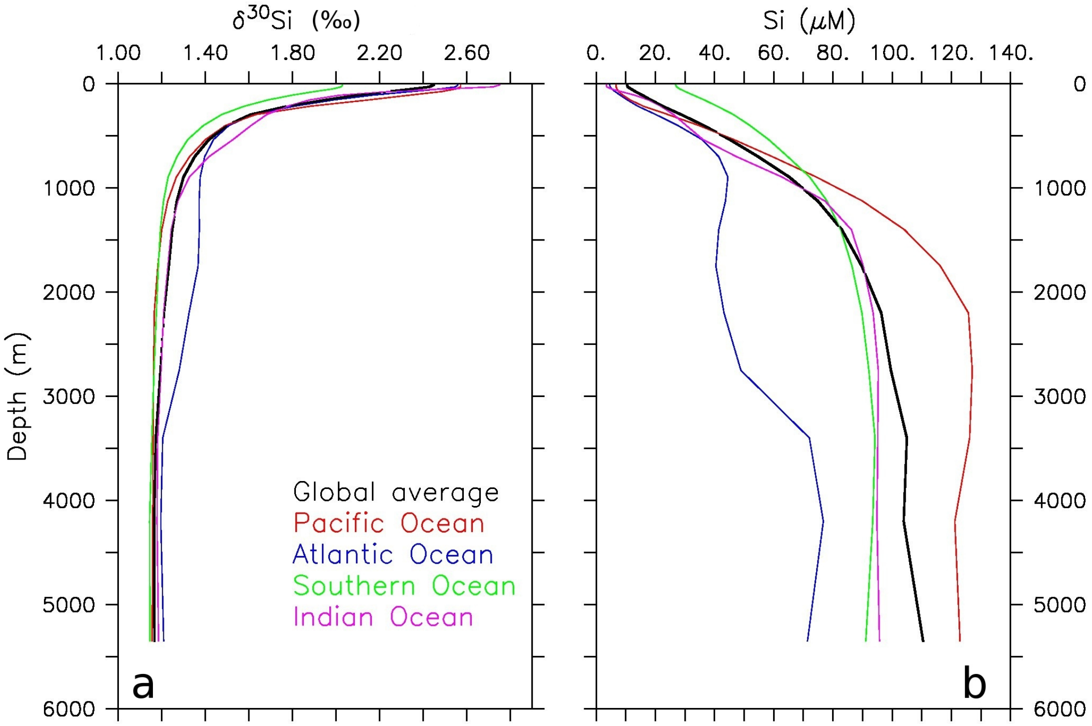

Figure 3.13: The vertical profiles of (a) δ^{30}Si of silicic acid (‰) and (b) silicic acid concentrations (μmol L^{-1}) in different ocean basins.

which might look different if we include fractionation during BSi dissolution in the model (see Figure 4.5).

3.4 Discussion

3.4.1 Rayleigh distillation

Both in the vertical and horizontal distributions, there is an inverse relation between the concentration of silicic acid and its isotopic composition δ^{30}Si. Plotting these two variables against each other shows a Rayleigh-like relationship in surface waters of the different ocean basins (Pacific, Atlantic, Southern Ocean and Indian Ocean) (Figure 3.15a). The

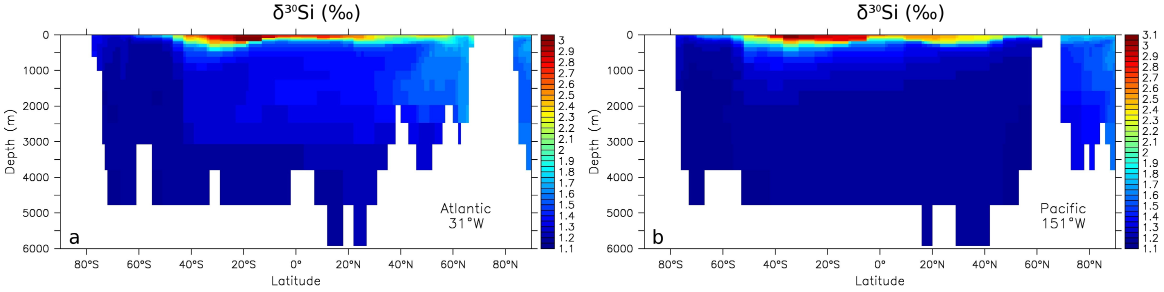

Figure 3.14: The δ^{30}Si of silicic acid (‰) through an Atlantic section (31 °W) (a) and a Pacific section (151 °W) (b).

Table 3.1: Information of regression equations of natural logarithm of silicic acid concentration versus the corresponding $\delta^{30}\mathrm{Si}_{\mathrm{DSi}}$ in different ocean basins

Ocean basin	Slope of regression lines	r^2
Pacific	-0.67	0.96
Atlantic	-0.67	0.79
Southern Ocean	-0.59	0.98
Indian Ocean	-0.79	0.95

$\delta^{30}\mathrm{Si}_{\mathrm{DSi}}$ value increases along the Rayleigh-like curve during the utilization of silicic acid, which demonstrates the primary control of biological fractionation on $\delta^{30}\mathrm{Si}_{\mathrm{DSi}}$ distribution. Figure 3.15b shows the natural logarithm of silicic acid concentration versus the corresponding $\delta^{30}\mathrm{Si}_{\mathrm{DSi}}$ in different ocean basins and they all show approximately linear relations. The slope of each regression line shown in Table 3.1 exhibits spatial variation depending on oceanic conditions. In some ocean regions the physical transport of water has non-negligible influence on surface water nutrient concentrations such as the vertical mixing in the Southern Ocean. Thus, in these regions the behavior of the system shows more affinity with the "open system" than with the "closed system" (see detailed description of both systems in Chapter 1). As shallower the slope of the regression line is, as closer the system is to an "open system".

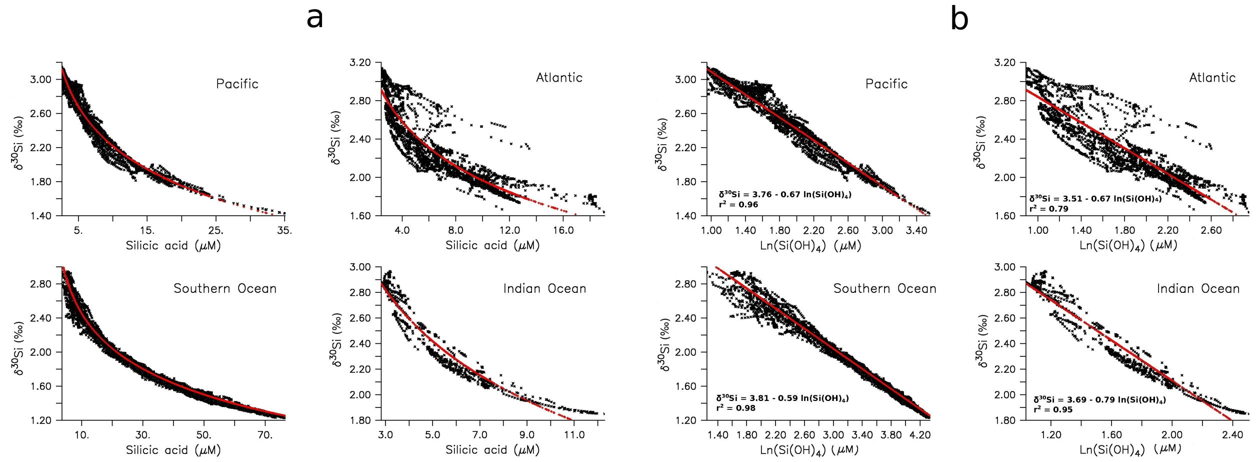

Figure 3.15: (a) Silicic acid concentration (μmol L^{-1}) in upper 90 m water column versus the corresponding δ^{30}Si (‰) in four different ocean basins and (b) natural logarithm of silicic acid concentration (μmol L^{-1}) versus its δ^{30}Si (‰) in the according ocean basins. The red lines are linear regression curves of ln(Si(OH)$_4$) versus δ^{30}Si in all panels, the y-intercepts of the regression lines are in ‰ unit.

3.4.2 Model-data comparison

In the last decade, the number of in situ measurements of δ^{30}Si is growing rapidly, especially after the GEOTRACES Project (`http://www.geotraces.org/`) has been launched. The expansion of the silicon isotope database provides the possibility of a comprehensive comparison between observation data and model results. Here we compare the measured and modeled DSi concentrations and $\delta^{30}\mathrm{Si}_{\mathrm{DSi}}$ both in the surface water (averaged between 0 and 100 m) and in the deep water (averaged between 2000 m and the ocean bottom).

The simulated DSi concentration and $\delta^{30}\mathrm{Si}_{\mathrm{DSi}}$ in the surface ocean compare well to the in situ measurements with the exception of a few locations in the North Pacific and the Southern Ocean (Figure 3.16). As we mentioned before, the model underestimates the deep DSi concentration and vertical mixing in the North Pacific subpolar gyre, which leads to lower surface concentrations of DSi and consequently to a higher $\delta^{30}\mathrm{Si}_{\mathrm{DSi}}$ signature. In the Pacific sector of the Southern Ocean, the in situ data at two stations [(57.8 °S, 103 °W) and (62.2 °S, 103 °W)] show much higher $\delta^{30}\mathrm{Si}_{\mathrm{DSi}}$ than the modeled values. This might be attributed to the significant seasonal signal (data were collected during December 2007-

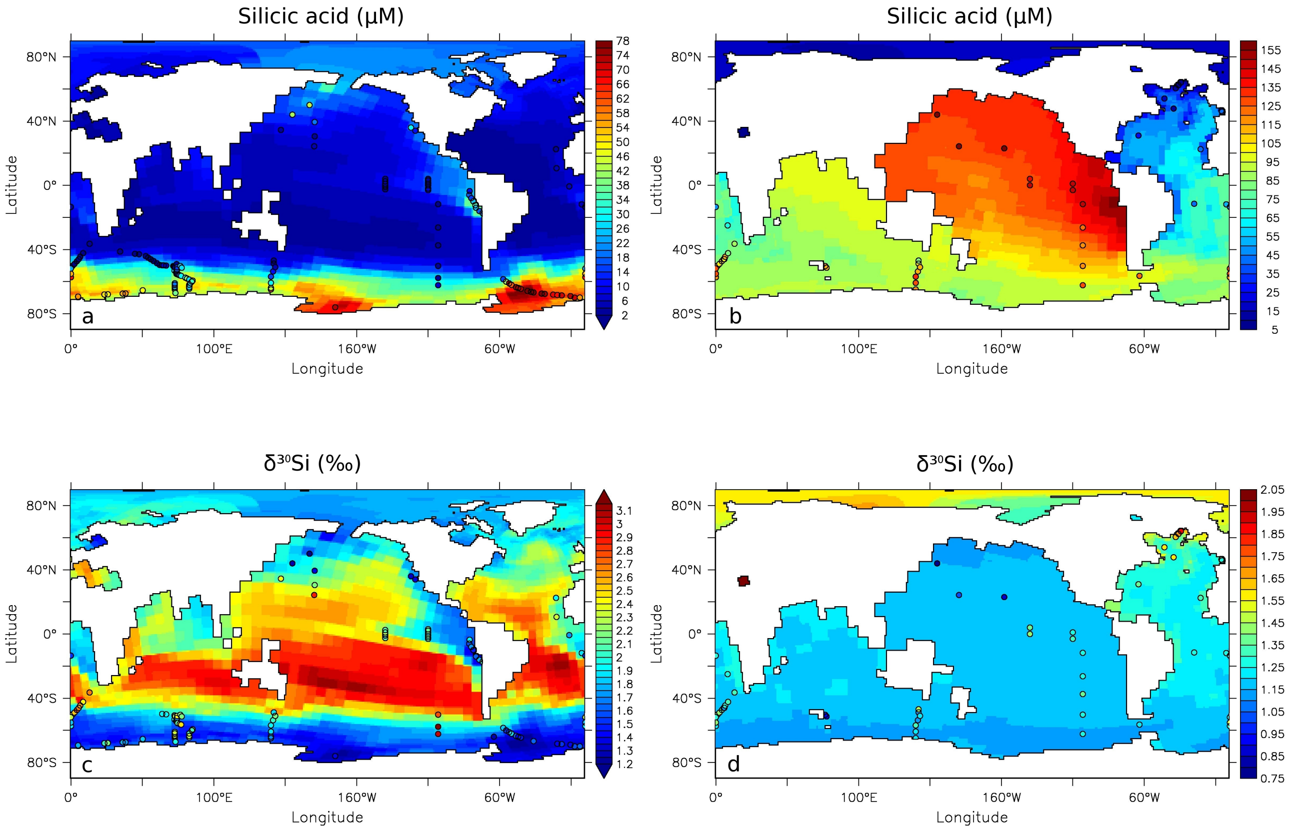

Figure 3.16: In situ measurements (colored dots) plotted over model results: (a) silicic acid concentration (μmol L^{-1}) averaged in upper 100 m water column; (b) silicic acid concentration (μmol L^{-1}) averaged between 2000 m and the sea floor; (c) δ^{30}Si of silicic acid (‰) averaged in upper 100 m water column; and (d) δ^{30}Si of silicic acid (‰) averaged between 2000 m and the sea floor.

February 2008, the Southern Hemisphere summer) contrasting to the annual mean values of the model, combined with the shallower in situ sampling depths of both stations (15 m at the northern station, 4 m and 32 m at the southern station) compared with the model representation (averaged between 0 and 100 m).

In the deep ocean, the simulated DSi concentrations are higher than observed in the Atlantic and lower in the Pacific and the Southern Ocean. This reflects the deficiencies of the coarse resolution ocean circulation model such as the too shallow Atlantic Deep Water and the too strong invasion of Antarctic Bottom Water into the north deep Atlantic (Figure 3.3b). Nevertheless, the model-data comparison exhibits the reliability of the model performance on reproducing the large-scale oceanic $\delta^{30}\mathrm{Si}_{\mathrm{DSi}}$ distribution pattern.

Table 3.2: The differences in modeling techniques between *Wischmeyer et al.* (2003)'s and our work

	Wischmeyer's work	This work
Ocean Model	Offline transport from LSG[a]	Online MPI-OM OGCM[b]
Biogeochemical Model	HAMOCC[c]4	HAMOCC[c]5.1
Model Grid	3.5 ° × 3.5 ° Arakawa E-grid	6 ° × 3.6 ° Arakawa C-grid
Vertical resolution	15 layers	20 layers
Time step	3 days	3 hours
Iron limitation	No iron limitation for nutrient uptake	With iron limitation for nutrient uptake
Approximation of ^{29}Si/^{28}Si fractionation	Assuming no fractionation	Approximation of ^{29}Si/^{28}Si fractionation according to mass dependency

[a] The Hamburg Large Scale Geostrophic Ocean General Circulation Model.

[b] Max-Planck-Institute global Ocean General Circulation Model.

[c] Hamburg Ocean Carbon Cycle Model.

3.4.3 Comparison with ***Wischmeyer et al.*** (2003)'s results

This work is based on *Wischmeyer et al.* (2003)'s pioneering simulation of the δ^{30}Si distribution. The major differences in modeling techniques between their and our studies are shown in Table 3.2.

We agree with *Wischmeyer et al.* (2003) on the high $\delta^{30}\mathrm{Si}_{\mathrm{DSi}}$ and low silicic acid concentration occurring in the surface waters of the subtropical gyres. However, our model predicts a maximum annual mean $\delta^{30}\mathrm{Si}_{\mathrm{DSi}}$ averaged in the upper 90 m of +3.15‰, which is much lower than their reported ∼+6‰. The highest observed $\delta^{30}\mathrm{Si}_{\mathrm{DSi}}$ in situ so far is +4.4‰, which corresponds to an extremely depleted silicic acid concentration of 0.2 μmol L^{-1} in the Equatorial Pacific (*Grasse et al.*, 2013). The reason for having a $\delta^{30}\mathrm{Si}_{\mathrm{DSi}}$ value as hight as +6‰ in *Wischmeyer et al.* (2003)'s model might be the strong depletion of silicic acid characterized by the BSi export of 177 Tmol yr^{-1} at 100 m depth. Both models predict seasonal variations of surface $\delta^{30}\mathrm{Si}_{\mathrm{DSi}}$. Different from *Wischmeyer et al.* (2003)'s result, our model shows the seasonal variation of both DSi concentration and $\delta^{30}\mathrm{Si}_{\mathrm{DSi}}$ primarily at high latitudes (approximately greater than 40 ° in the Northern and the Southern Hemisphere) rather than occurring in the subtropical gyres. Another improvement is that our model captures the difference in deep $\delta^{30}\mathrm{Si}_{\mathrm{DSi}}$ between the North Atlantic and the North Pacific with a clear decreasing gradient along the conveyor belt contrary to the reported little isotopic variation between deep ocean basins by *Wischmeyer et al.* (2003). This may be attributed to the high diffusion caused by coarse time steps (3-day) of advection in their model.

The improvements of the model performance are built on top of *Wischmeyer et al.* (2003)'s pioneering work and relied on the expanded measurements and improved understanding of $\delta^{30}\mathrm{Si}$ in the last decade. Some limitations of the current model setup are the relatively coarse model resolution, which may cause high diffusivity that influences nutrient distributions, and the expensive computation and long equilibration time.

Chapter 4

Modeling Results II: fractionation during biogenic silica dissolution

In this chapter, we present the second set of modeling results, where it is assumed that Si fractionation occurs not only during the formation of diatom frustules but also during their dissolution (see model setup in section 2.4). The model is in a quasi-steady state with respect to all nutrient distributions after running for 10,000 model years. These distributions will not change by introducing a silicon isotopic fractionation during dissolution of diatom frustules and thus we refer the reader to Chapter 3 for the distribution of DSi. In the current chapter we focus on the change in δ^{30}Si distributions.

We will use the notation ”FD” and ”NoFD”, respectively, for the model runs with (FD, current chapter) and without fractionation (NoFD, Chapter 3) during biogenic silica dissolution.

4.1 Introduction to fractionation during biogenic silica dissolution

4.1.1 Isotopic fractionation

A laboratory work by *Demarest et al.* (2009) has revealed that during biogenic silica (BSi) dissolution the dissolved silicon (DSi) has a δ^{30}Si value that is consistently 0.55‰ lower than that of its parent material over a wide variety of diatom assemblages, particle ages and solubilities, and ambient temperatures. The isotopic fractionation against heavier isotopes, then, occurs not only during BSi production but also during BSi dissolution. The fractionation during dissolution acts in the opposite sense (to increase δ^{30}Si of BSi) and at about half the magnitude of that associated with BSi production.

4.1.2 Implications for δ^{30}Si in the modern ocean

Tréguer and De La Rocha (2013) estimated that ~56% of the total BSi production dissolves in the surface layer. The fraction of dissolution can vary spatially from 10% of the local production in coastal upwelling areas to 80% in the open ocean central gyres (*Tréguer and De La Rocha*, 2013). In addition, the production and dissolution of BSi are uncoupled temporally, since it is not until after diatom death and degradation of its protective organic coating that the frustules are prone to dissolution. All these facts cause complications in interpreting δ^{30}Si distribution patterns, especially when dissolution-mediated fractionation takes place. Since the measured isotopic difference Δ^{30}Si ($\delta^{30}\mathrm{Si}_{\mathrm{BSi}}$ minus $\delta^{30}\mathrm{Si}_{\mathrm{DSi}}$) represents the combined net effect of two processes rather than the biological production signal alone, the field estimates of the fractionation factor ϵ_{BSi} for BSi production in surface waters may be dampened by the fractionation effect associated with dissolution. Estimates of ϵ_{BSi} derived from field measurements might, therefore, be underestimated in magnitude, as higher rates of dissolution bias the measurement toward

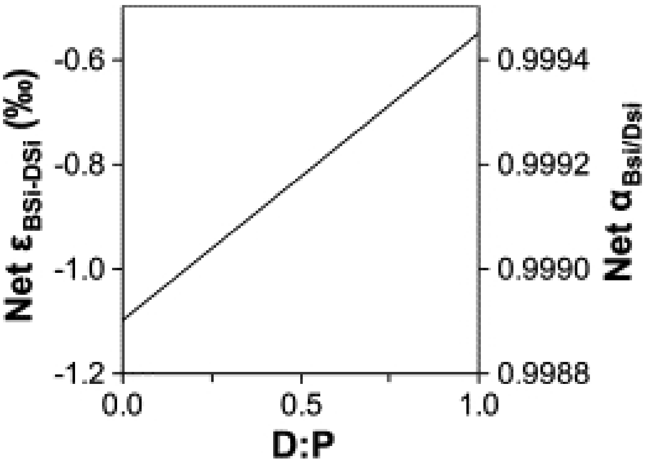

Figure 4.1: The net enrichment factor $\epsilon_{\mathrm{BSi-DSi}}$ and fractionation factor $\alpha_{30/28}$ as estimated by the measured difference in δ^{30}Si between the $bSiO_{2(s)}$ and $Si(OH)_{4(aq)}$ phases ($\Delta_{BSi-DSi}$) and driven by the balance between $bSiO_2$ production (P) and dissolution (D) in a steady-state system, according to the equation Net $\epsilon_{BSi-DSi} = \epsilon_{prod} + (\epsilon_{diss} \cdot D : P)$. Trends are based on $\epsilon_{\mathrm{BSi-DSi}}$ values of -1.1‰ for the production fractionation term (ϵ_{prod}; *De La Rocha et al.* (1997)) and +0.55‰ for the dissolution fractionation term (ϵ_{diss}; *Demarest et al.* (2009)). Note that the frame of reference is the enrichment in ^{30}Si of the particulate material relative to the dissolved pool, and that D:P cannot exceed a value of 1 under steady-state conditions (taken from *Demarest et al.* (2009)).

positive values. As illustrated by *Demarest et al.* (2009) in Figure 4.1, an increase in the rate of BSi dissolution relative to that of production will be reflected in a positive shift in the isotopic difference Δ^{30}Si, which can directly reveal the level of surface silicic acid recycling. The study by *Demarest et al.* (2009) thus offers an alternative explanation for values of Δ^{30}Si measured in situ that departs from -1.1‰, other than regional mixing. Later in this chapter the Δ^{30}Si distributions in both model runs are compared in order to estimate the possible effect on Δ^{30}Si associated with BSi dissolution.

4.1.3 Implications for δ^{30}Si as a paleo-proxy

Assuming that a significant amount of the BSi that buries in the sediment has been undergone dissolution to a certain extent, and the fractionation during BSi dissolution takes place in the field following the laboratory findings by *Demarest et al.* (2009), sedimentary records of $\delta^{30}\mathrm{Si}_{\mathrm{BSi}}$ are likely biased toward positive values. This will cause an overestimation of the relative level of past surface silicic acid uptake, if the dissolution-mediated fractionation effect is not taken into account. Thus, the preservation efficiency of BSi plays an important role in affecting sedimentary $\delta^{30}\mathrm{Si}_{\mathrm{BSi}}$ records. A number of sediment core data from the Southern Ocean (*Dezileau et al.*, 2003) indicates that, the level of BSi dissolution in Indian Antarctic and Subantarctic cores falls between 30% and 75% overall, but with differences within individual cores not exceeding 30% between marine isotope stages. The maximum of 30% within-core BSi preservation difference equates to ~0.16‰ variations in the $\delta^{30}\mathrm{Si}_{\mathrm{BSi}}$ values mediated by dissolution. This range of variation comprises about 10-30% of the within-core changes observed over glacial-interglacial timescales. Although differences of less than ~20% in dissolution between samples are unlikely to impose a measurable bias in their respective $\delta^{30}\mathrm{Si}_{\mathrm{BSi}}$ values, discrepancies in excess of this amount may determine the level of error introduced into the $\delta^{30}\mathrm{Si}_{\mathrm{BSi}}$ as a paleo-proxy (*Demarest et al.*, 2009).

4.2 The δ^{30}Si distribution

4.2.1 Horizontal distributions of δ^{30}Si

The annual average value of $\delta^{30}\mathrm{Si}_{\mathrm{DSi}}$ in the upper 90 m ranges from +0.55 to +2.55‰, with the higher values occurring in the subtropical gyres (Figure 4.2a), where silicic acid is depleted. Despite the pattern is similar, the surface $\delta^{30}\mathrm{Si}_{\mathrm{DSi}}$ in model run FD is approximately 0.6‰ lower than that in model run NoFD (Figure 4.3a, b). In the deep ocean, however, $\delta^{30}\mathrm{Si}_{\mathrm{DSi}}$ ranges from +0.7 to +1.1‰ in most of the ocean areas below 2000 m, which is also lower than the values in model run NoFD (Figure 4.3c, d). The deep $\delta^{30}\mathrm{Si}_{\mathrm{DSi}}$ both in the Atlantic and in the Pacific decreases from north to south, which is in contrast to the pattern in model run NoFD, whose deep $\delta^{30}\mathrm{Si}_{\mathrm{DSi}}$ decreases along the conveyor belt from the North Atlantic to the North Pacific. In the sediment, $\delta^{30}\mathrm{Si}_{\mathrm{BSi}}$ has a larger range of -0.1 to +3.1‰ in model run FD compared with the range in model run NoFD of +0.1 to +1.95‰ (Figure 4.3e, f). In model run NoFD, the sediment $\delta^{30}\mathrm{Si}_{\mathrm{BSi}}$ is mainly controlled by the exported signal of $\delta^{30}\mathrm{Si}_{\mathrm{BSi}}$, while in model run FD it is controlled also by the fractionation process during BSi dissolution both in the water column and in the sediment. An interesting feature of δ^{30}Si distribution in model run FD is that in the water column $\delta^{30}\mathrm{Si}_{\mathrm{DSi}}$ is lower compared to model run NoFD, but in sediment $\delta^{30}\mathrm{Si}_{\mathrm{BSi}}$ is higher in most of the areas than that in model run NoFD (Figure 4.3). This can be understood as an isotopic composition shift between the water and the sediment within these two model runs. In model run FD, as dissolution of BSi discriminates against the release of the heavier isotopes of silicon, the isotopic composition of BSi increases with water depth and further rises in the sediment throughout dissolution. This causes release of relatively light isotopes into the water column and burial of relatively heavier isotopes into the sediment compared with model run NoFD. Thus, the average $\delta^{30}\mathrm{Si}_{\mathrm{DSi}}$ of the ocean shifts toward a lower value and the $\delta^{30}\mathrm{Si}_{\mathrm{BSi}}$ of the sediment shifts then toward a higher value due to the fractionation during BSi dissolution.

As fractionation during the BSi dissolution process is included in model run FD, we should see the positive shift of isotopic difference Δ^{30}Si ($\delta^{30}\mathrm{Si}_{\mathrm{BSi}}$ minus $\delta^{30}\mathrm{Si}_{\mathrm{DSi}}$) between model run FD and model run NoFD (Figure 4.4). Δ^{30}Si in model run FD shifts toward more positive values roughly between 30 °S and 30 °N compared to model run NoFD. As we subtract Δ^{30}Si of model run NoFD from that of model run FD, we take off the effects of fractionation during BSi production and regional mixing. In this way, Figure 4.4 shows only the fractionation effect associated with BSi dissolution. If we take the higher limit of the positive shift of 0.14‰ in Figure 4.4, it should yield a ~25% recycling of Si from total production in this area according to the following equation by *Demarest et al.* (2009), see more information in the legend of Figure 4.1.

$$\mathrm{Net}\,\epsilon_{BSi-DSi} = \epsilon_{prod} + (\epsilon_{diss} \cdot D : P) \tag{4.1}$$

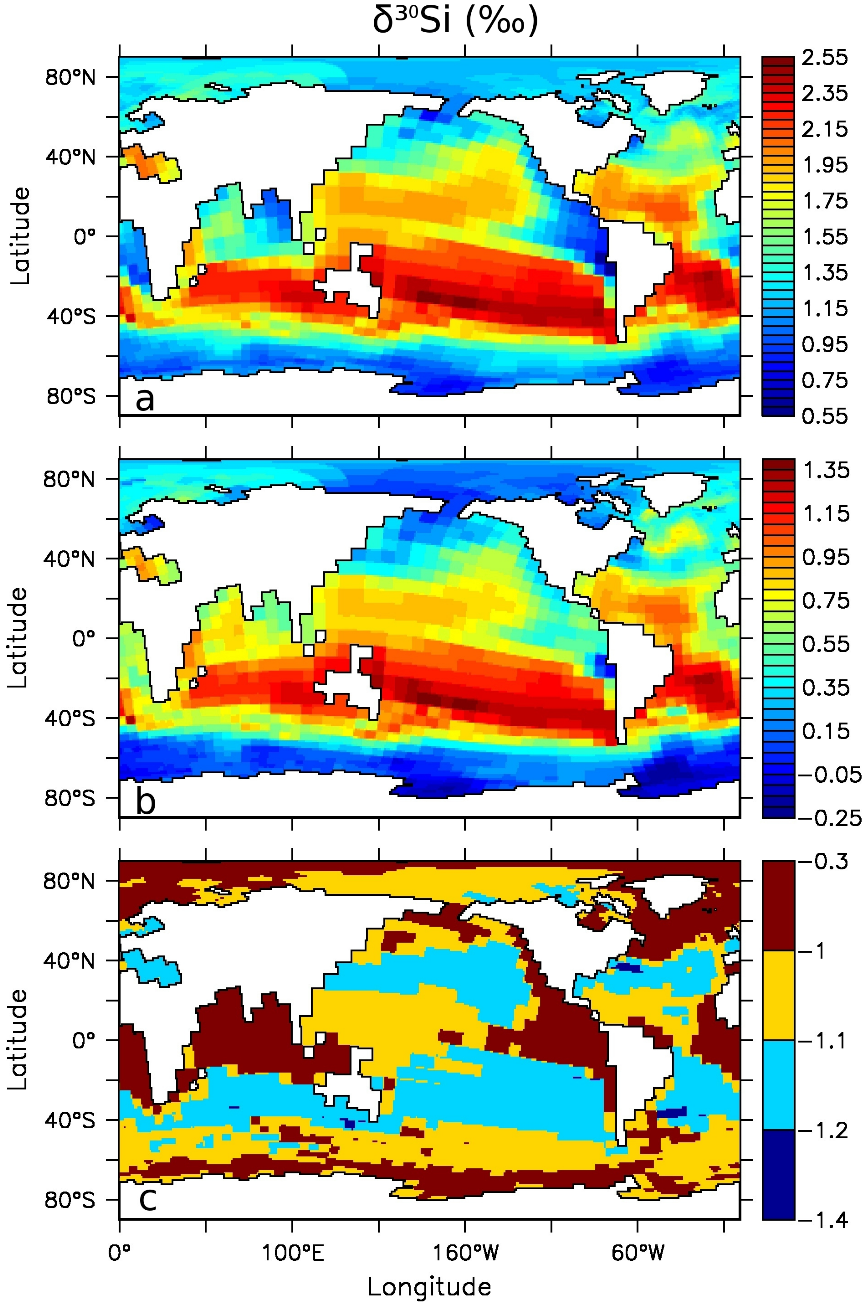

Figure 4.2: (a) The δ^{30}Si of silicic acid (‰) and (b) δ^{30}Si of biogenic opal (‰) in the surface ocean and (c) the difference between (b) and (a). Note the non-linear color scaling in the lower panel.

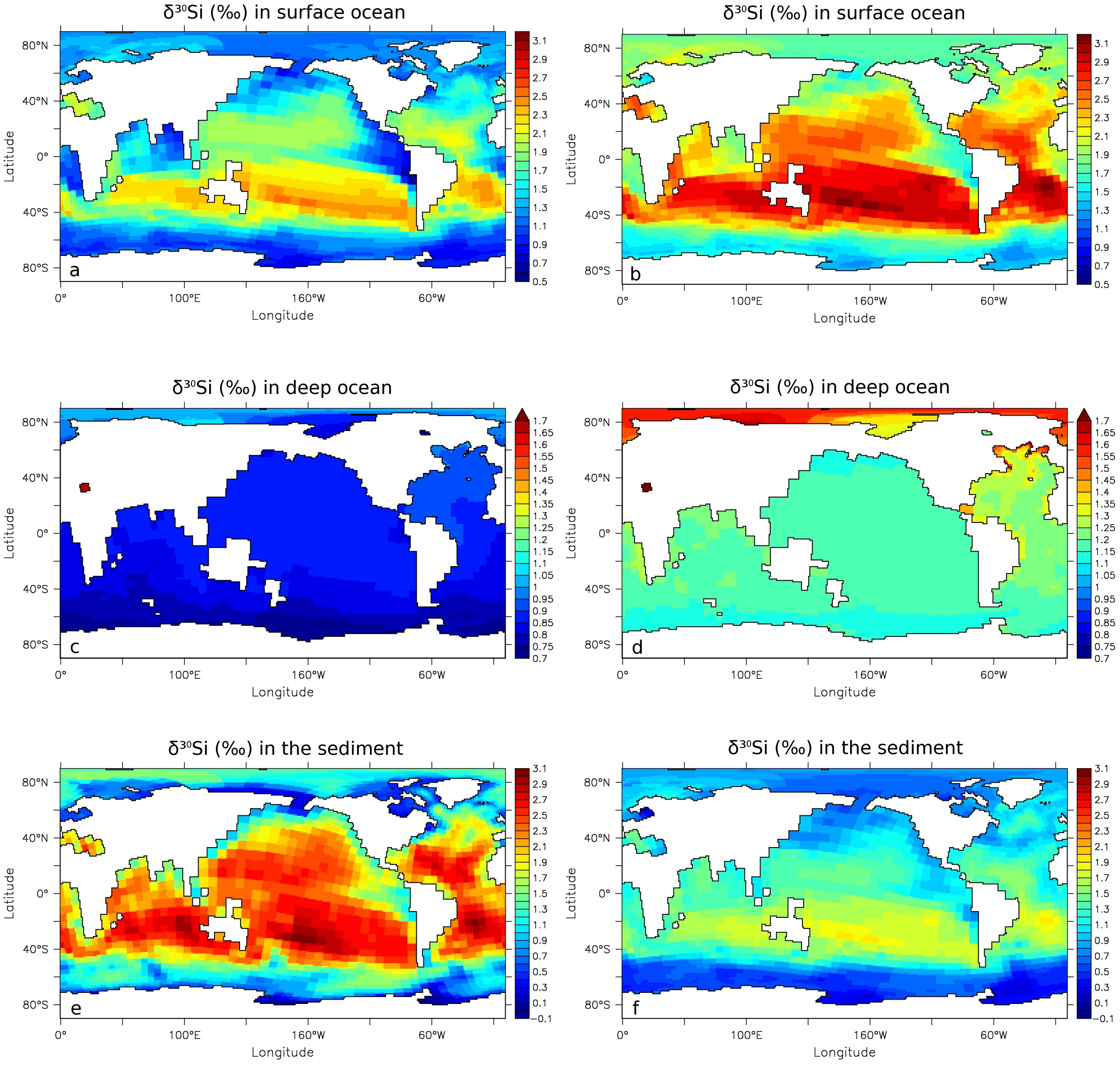

Figure 4.3: Comparison of model results between the run with fractionation during biogenic silica dissolution (a, c, e) and the run without (b, d, f). Annual mean δ^{30}Si (‰) of silicic acid in the surface ocean (a, b), in the deep ocean (averaged between 2000 and 6000 m) (c, d) and of biogenic opal in the surface sediment (e, f). The same coloring scale is used for each pair of graph.

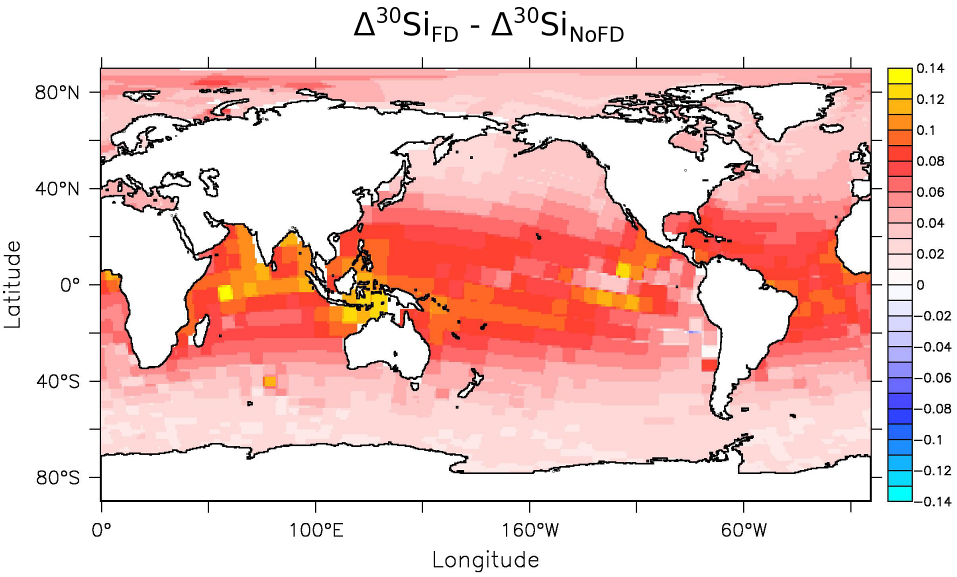

Figure 4.4: The difference in Δ^{30}Si = δ^{30}Si$_{\mathrm{BSi}}$-δ^{30}Si$_{\mathrm{DSi}}$ (‰) between model run FD and model run NoFD. It is also the difference between Figure 4.2c and Figure 3.5c.

4.2.2 Vertical distributions of δ^{30}Si

The vertical distributions of δ^{30}Si$_{\mathrm{DSi}}$ through an Atlantic section (31 °W) and a Pacific section (151 °W) are shown in Figure 4.5. The highest δ^{30}Si$_{\mathrm{DSi}}$ value occurs in the subtropical surface water due to fractionation during biological uptake. Interestingly the intermediate water has the lowest δ^{30}Si$_{\mathrm{DSi}}$ value compared to surface or deep waters in this model run. Fractionation during BSi dissolution discriminates against the release of heavier isotopes of silicon, which leads to a rise in δ^{30}Si$_{\mathrm{BSi}}$ as dissolution carries on. The δ^{30}Si$_{\mathrm{DSi}}$ signal that is released from BSi dissolution follows the increasing trend of δ^{30}Si$_{\mathrm{BSi}}$ with depth. As a result, the vertical gradient of δ^{30}Si$_{\mathrm{DSi}}$ is greater in this model run than in model run NoFD (see Figure 3.14) and it represents, to a certain extent, the BSi dissolution pattern of the model.

The horizontally averaged vertical profiles of δ^{30}Si$_{\mathrm{DSi}}$ and δ^{30}Si$_{\mathrm{BSi}}$ of both model runs are shown in Figure 4.6. In both model runs δ^{30}Si$_{\mathrm{DSi}}$ has the highest horizontally averaged value in the surface ocean due to the fractionation during BSi formation. The value of

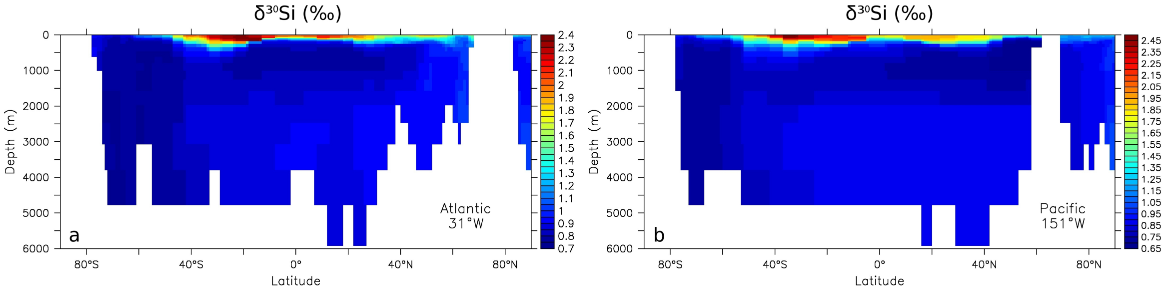

Figure 4.5: The δ^{30}Si of silicic acid (‰) through an Atlantic section (31 °W) (a) and a Pacific section (151 °W) (b).

$\delta^{30}\mathrm{Si}_{\mathrm{DSi}}$ in model run FD is, additionally, influenced by the isotopic signal released from BSi dissolution, which increases with depth as a result of fractionation. There is no surprise that the $\delta^{30}\mathrm{Si}_{\mathrm{BSi}}$ signal of model run FD increases from the surface to the ocean bottom as dissolution carries on. However, the δ^{30}Si distribution in the water column depends very much on diatom dissolution pattern, assuming that fractionation takes place during BSi dissolution. In reality, it is very likely that the more soluble members of diatom species dissolve completely in the upper ocean, while more robust species have a low degree of dissolution until they reach the sediment (*Lewin*, 1961; *Barker et al.*, 1994). Another possible departure of the model from the real process in nature might be the fraction of dissolution occurring in water column versus sediment. The model estimates a portion of 77% dissolution of the exported BSi in the water column versus a portion of 17% in the sediment (the rest is buried into a diagenetically consolidated layer), which is closer to the earlier estimates by *Tréguer et al.* (1995) of 76% versus 19%, respectively, rather than the new estimates of 25% versus 69% (*Tréguer and De La Rocha*, 2013). In this case, the model represents the maximum fractionation effect associated with BSi dissolution in the water column, which is unlikely to be observed in situ. Despite the limitations of the model, this study takes the very first step of modeling fractionation during BSi dissolution in the oceans and in marine sediments toward a complete understanding of the oceanic δ^{30}Si distribution.

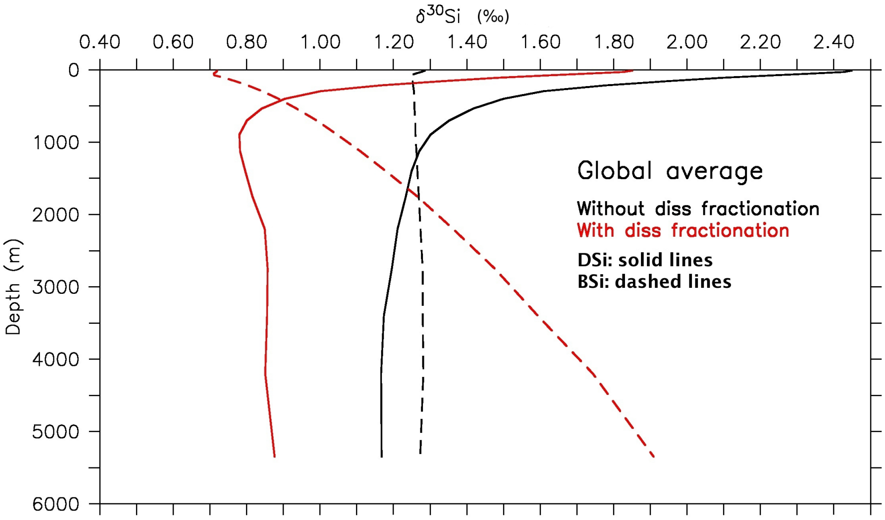

Figure 4.6: The horizontally averaged vertical profiles of δ^{30}Si (‰) of silicic acid (solid lines) and of biogenic silica (dashed lines) in both model runs with (in red) and without (in black) fractionation during biogenic silica dissolution.

4.3 Model-data comparison

In Figure 4.7, results from both the model runs are compared with in situ measurements by *de Souza et al.* (2012b) of $\delta^{30}\mathrm{Si}_{\mathrm{DSi}}$ and silicic acid concentration at four stations in the Atlantic. As we can see in Figure 4.7 a and c, $\delta^{30}\mathrm{Si}_{\mathrm{DSi}}$ profiles show the typical increase toward the surface, which is the result of the preferential uptake of lighter Si isotopes by diatoms in surface waters in both in situ and modeled results. Values of $\delta^{30}\mathrm{Si}_{\mathrm{DSi}}$ in the South Atlantic range from ∼+1.2‰ in bottom waters to ∼+2.8‰ in surface waters for model run NoFD, which are in close agreement with the in situ measurements. The vertical gradient of $\delta^{30}\mathrm{Si}_{\mathrm{DSi}}$ values is largest in the upper ocean, above the salinity minimum at ∼1000 m associated with Antarctic Intermediate Water (AAIW) in the South Atlantic (*de Souza et al.*, 2012b), which can be observed in DSi concentration profiles of both measured and modeled data (Figure 4.7 b and d). Below 1000 m, $\delta^{30}\mathrm{Si}_{\mathrm{DSi}}$ values continue to decrease with depth in both measured data and results from model run

NoFD, but the vertical gradients are much smaller. Because our model overestimates DSi concentrations both in the North and South Atlantic, the $\delta^{30}\mathrm{Si}_{\mathrm{DSi}}$ values are very likely underestimated, especially in the deep ocean. We can expect higher values of $\delta^{30}\mathrm{Si}_{\mathrm{DSi}}$ in model run NoFD, which might be then higher than the observed values from *de Souza et al.* (2012b) (Figure 4.7c). The values of $\delta^{30}\mathrm{Si}_{\mathrm{DSi}}$ of model run FD are obviously much lower than the measured data at all water depth and the increasing trend in $\delta^{30}\mathrm{Si}_{\mathrm{DSi}}$ values from ∼500 m depth toward the deep ocean in the South Atlantic, due to the dissolution-mediated fractionation, has not been observed in the in situ data. However, the combination of fractionation effects in both model runs may explain the discrepancies between the model results and the in situ measurements.

Currently the usage of fractionation during BSi dissolution as explanation to $\delta^{30}\mathrm{Si}$ distribution is still speculative. More work on mechanism study of fractionation associated with BSi dissolution and the influence of diatom dissolution pattern on the fractionation effect needs to be done.

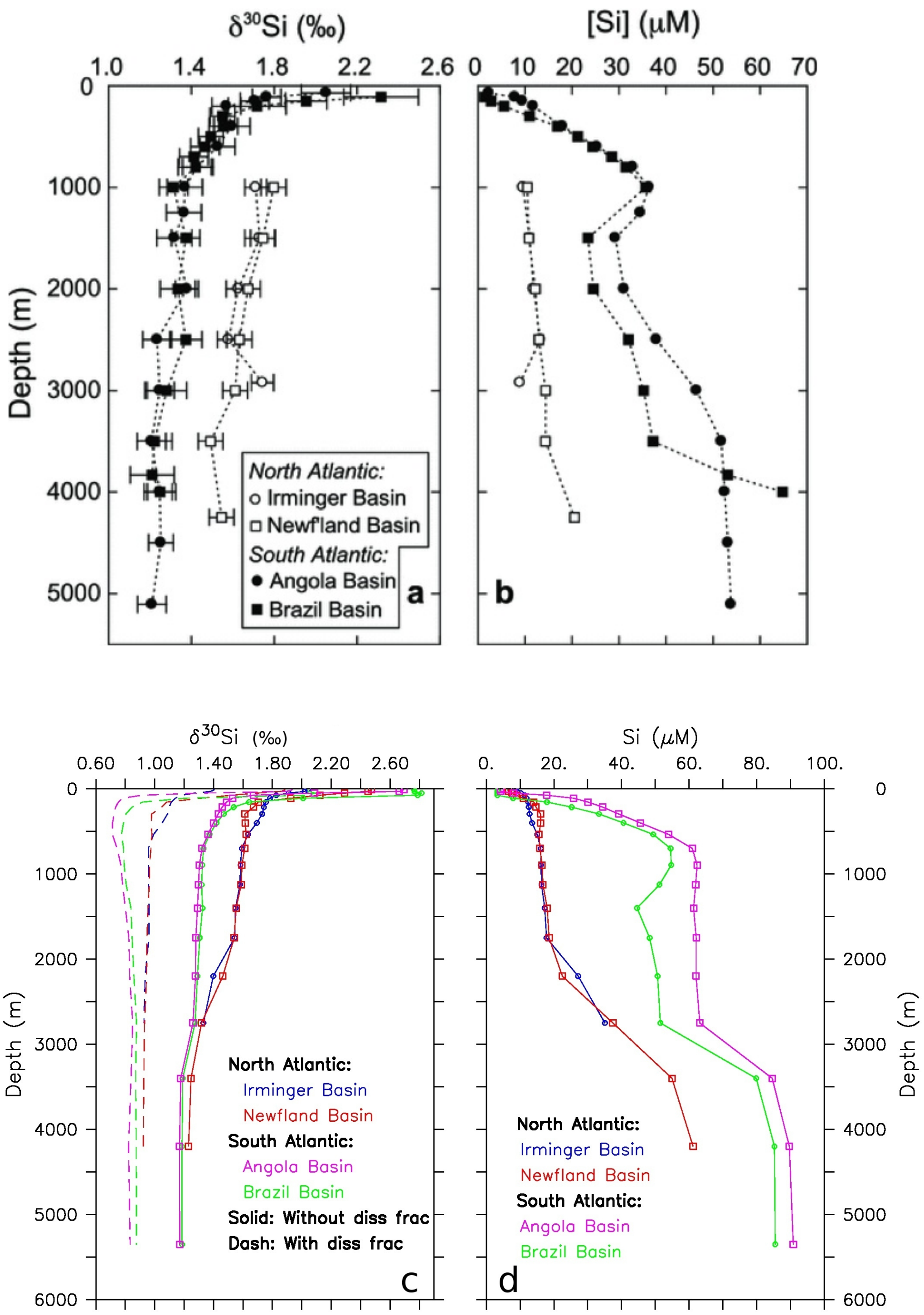

Figure 4.7: Comparison of in situ measurements of δ^{30}Si (‰) of silicic acid and the silicic acid concentration (μmol L^{-1}) at four stations in the Atlantic (*de Souza et al.*, 2012b) (a, b) with the model results (c, d) in both runs with (dashed lines) and without (solid lines) fractionation during biogenic silica dissolution at the corresponding stations.

Chapter 5

Last Glacial Maximum

5.1 Introduction

The Last Glacial Maximum (LGM) is defined as the most recent interval in Earth history when global ice sheets reached their maximum integrated volume (*Clark et al.*, 2009). This time period is constrained to a 3000-4000 years interval, centered at 21,000 (calendar) years before present (BP) (from 19,000 to 23,000 cal-years BP) by a reconstruction of sea-level change (*Yokoyama et al.*, 2000). During this time, vast ice sheets covered immense areas of northern Europe, North America, and Asia, causing a significant global average sea level drop of ∼130 m (*Mix et al.*, 2001). The decreased sea level lead to the exposure of continental shelves. Together with stronger global winds, less precipitation and reduced vegetation cover, the global average dust deposition may have been increased by 88% during the LGM relative to the current climate, based on a modeling study (*Mahowald et al.*, 2006).

The atmospheric CO_2 mixing ratio was 80 to 100 ppm lower during the LGM than the pre-industrial value (*Petit et al.*, 1999). A significant correlation has been discovered between the atmospheric $p\mathrm{CO}_2$, deep ocean temperatures and continental ice volume (*Shackleton*, 2000). Mechanisms proposed to explain the atmospheric CO_2 variations during glacial-interglacial cycles over the last 800,000 years consist of changes in various physical and biogeochemical processes, driven by changes in sea surface temperature (SST), nutrients, ocean circulation, carbonate chemistry and the "biological pump" (*Broecker and Henderson*, 1998; *Archer et al.*, 2000; *Sigman and Boyle*, 2000; *Toggweiler et al.*, 2006; *Kohfeld and Ridgwell*, 2009). The ocean certainly plays a key role in regulating the atmospheric CO_2 concentration over glacial-interglacial timescales. The Southern Ocean, above all, is essential in facilitating deep-water exchange between different ocean basins, which might have a fundamental impact on atmospheric CO_2 levels (*Köhler and Bintanja*, 2008; *Marshall and Speer*, 2012). A recent study based on Antarctic ice core analysis suggests that temporal change of atmospheric CO_2 and Antarctic temperature are highly correlated during the last deglacial warming (*Parrenin et al.*, 2013).

Diatoms are the most important primary producers in the Southern Ocean, accounting for more than 90% of the productivity during ice edge blooms (*Nelson and Smith Jr.*, 1986). The ultimate cause for the decline of Si:N uptake ratio by diatoms from present-day ∼4:1 to glacial 1:1 is believed to be the iron addition to the Southern Ocean in the dustier glacial time (*Brzezinski et al.*, 2002). The silicic acid leakage hypothesis (SALH) (*Nozaki and Yamamoto*, 2001; *Brzezinski et al.*, 2002; *Matsumoto et al.*, 2002; *Sarmiento et al.*, 2004; *Beucher et al.*, 2007; *Dubois et al.*, 2010) suggests that declines in diatom Si:N uptake ratio in the glacial Antarctic created a pool of unused silicic acid that was transported to low latitudes in Subantarctic Mode Water (SAMW). The increased supply of silicic acid to surface waters of low latitudes would benefit diatoms over coccolithophores, thereby enhancing diatom productivity. The reduced $CaCO_3$ production (carbonate pump) and diminished $CaCO_3$ to organic carbon rain ratio lower the atmospheric CO_2 by increasing surface ocean alkalinity.

Reconstruction of primary production and silicic acid utilization by diatoms in the Southern Ocean are of particular importance for understanding the ocean's role in control of atmospheric CO_2 variations during glacial-interglacial cycles. The silicon isotopic composition of biogenic opal is a promising proxy for providing information on diatom productivity and marine Si cycling in the past. *De La Rocha et al.* (1998) have suggested a strong decrease (~50%) in the relative utilization of silicic acid by diatoms in the Southern Ocean during the LGM relative to the present interglacial, by analyzing the δ^{30}Si of biogenic opal in three Antarctic sediment cores. Here we apply a coupled ocean-biogeochemical model to simulate the marine Si isotopic composition distribution during the LGM, which is so far, to the best of our knowledge, the first modeling study using a general circulation model (GCM) on the glacial δ^{30}Si distribution.

5.2 Model setup

For the LGM simulation, both the same ocean and biogeochemical model are applied as for the present-day reference run. Only the differences from the previous model setup are thus presented here. Readers should refer to Chapter 2 for a detailed model description.

The coupled ocean-biogeochemical model has a resolution of ~3 ° in the horizontal and 40 layers with increasing layer thickness in the vertical. The ocean model is driven by daily atmospheric forcing fields obtained from coupled atmosphere-ocean simulations under the LGM climate conditions with the climate model COSMOS (*Zhang et al.*, 2013). The LGM dust field is taken from modeling results by *Mahowald et al.* (2006). The atmospheric CO_2 mixing ratio is set to the LGM value of 185 ppm compared to pre-industrial 278 ppm in the reference run. The dissolved inorganic carbon (DIC) and alkalinity are initialized with values taken from a model simulation with LGM CO_2 mixing ratio at 185 ppm (*Xu*, 2012).

5.3 Preliminary results

After an integration time of 2000 years of the LGM simulation, the model is not yet in a completely steady state. Nevertheless, the spatial patterns of physical and biological tracers are converging, with a minor remaining drift in the ocean average values (e.g. the drift of global average ocean temperature and silicic acid concentration is 1×10^{-5} °C yr^{-1}

and 4 × 10^{-4} μmol L^{-1} yr^{-1}, respectively). In this chapter, the preliminary results from the LGM run are compared with the results from the reference run (with pre-industrial atmospheric CO_2 mixing ratio at 278 ppm, but a present-day physical forcing) obtained after the same integration time (referred to as the ”PD” run).

5.3.1 Ocean physics

The average temperature in the global ocean reaches 1.33 °C after 2000 model years in the LGM simulation, approximately 3.51 °C lower than that in the PD run. This is in close agreement with the 3.25 ± 0.55 °C cooling of the ocean during the LGM, derived from proxy data by *Clark et al.* (2009). Three model experiments conducted under the Paleoclimate Modeling Intercomparison Project Phase 2 (PMIP2) on average show a weaker temperature decline of ∼1.9 °C during the LGM (*Murakami et al.*, 2008). Global mean sea surface temperature (SST) in the LGM run is 3.42 °C colder than in the modern reference (PD) run, with the main cooling areas occurring around 60 °N in the North Atlantic and 50 °S in the Southern Ocean (Figure 5.1). This magnitude and pattern of cooling are in line with the multi-model analysis results based on the MARGO data set from *Annan and Hargreaves* (2013), who predict a decrease in SST during LGM of 3.5 ± 1.2 °C. The SST pattern in our simulation is very similar to the results of the coupled atmosphere-ocean model from *Zhang et al.* (2013), from which our atmospheric forcing fields are taken. Our LGM simulation indicates an equatorward extension of annual sea-ice cover around Antarctica relative to the PD run (Figure 5.2), with a maximum sea-ice covered area of 65.8 × 10^6 km^2, more than 1.5 times of that in the PD run (39.4 × 10^6 km^2, estimated as the area where annually averaged fractional ice coverage >1.25%). The Drake passage transport is 163 Sv in the LGM run, somewhat weaker compared to 189 Sv in the PD run. The simulated Atlantic Meridional Overturning Circulation (AMOC) in the LGM run is stronger than that in the PD run, with a maximum transport of ∼27 Sv compared to PD run's ∼19 Sv (Figure 5.3). This is in agreement with *Zhang et al.* (2013)'s model results, from which the forcing data for the LGM run was derived. This indicates

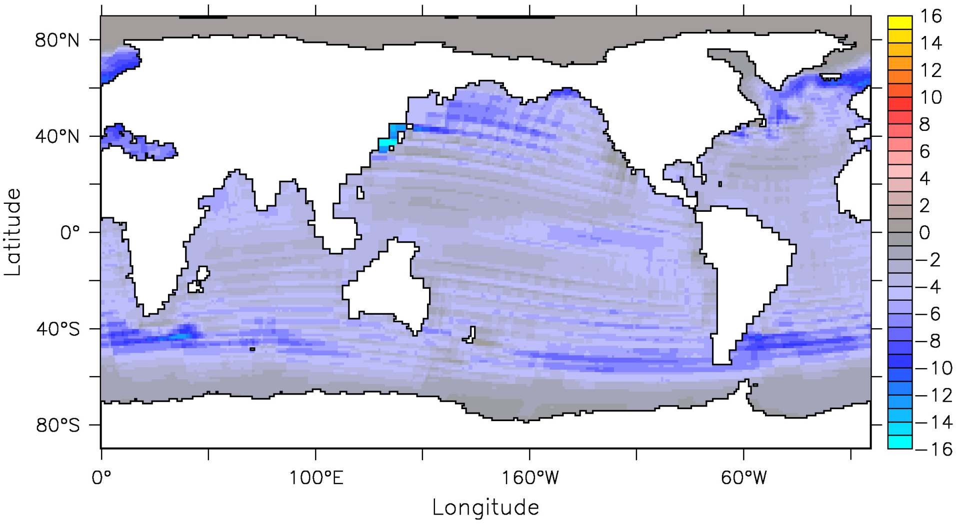

Figure 5.1: Annual mean sea surface temperature (°C) anomaly (difference between the LGM run and the present-day reference run).

that the ocean circulation in our model is comparable to theirs. It is noteworthy that the different spatial resolution of these two simulations (the LGM run with a resolution of ~3° versus the PD run of ~6°) may also contribute to the difference between the LGM and the PD run.

5.3.2 Nutrient distribution and export production

Similar to the modern distribution, surface silicic acid concentrations in the LGM run are less than 5 μmol L^{-1} in the subtropical gyres, but as high as 80 μmol L^{-1} in the Southern Ocean (Figure 5.4a). The simulated LGM surface silicic acid concentrations are higher in both the Southern Ocean and the Arctic Ocean compared to the PD run. The extension of ice sheets in both Northern and Southern Hemispheres may cause a reduction of phytoplankton growth due to low light under the ice. Therefore, the silicic acid utilization by diatoms in high latitudes are limited, which is in line with the reduced biogenic opal export fluxes in the Southern Ocean shown in Figure 5.6d.

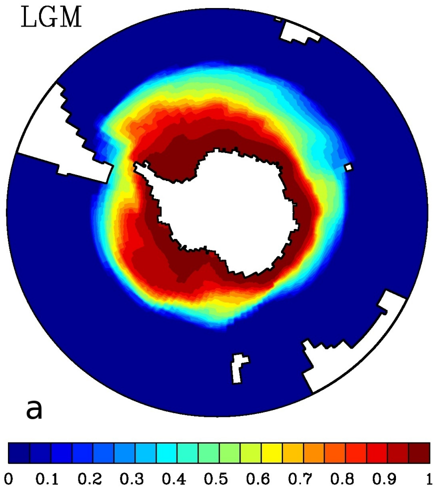

Figure 5.2: Annual mean fractional sea-ice cover in the Southern Hemisphere in the (a) LGM run and (b) present-day reference run.

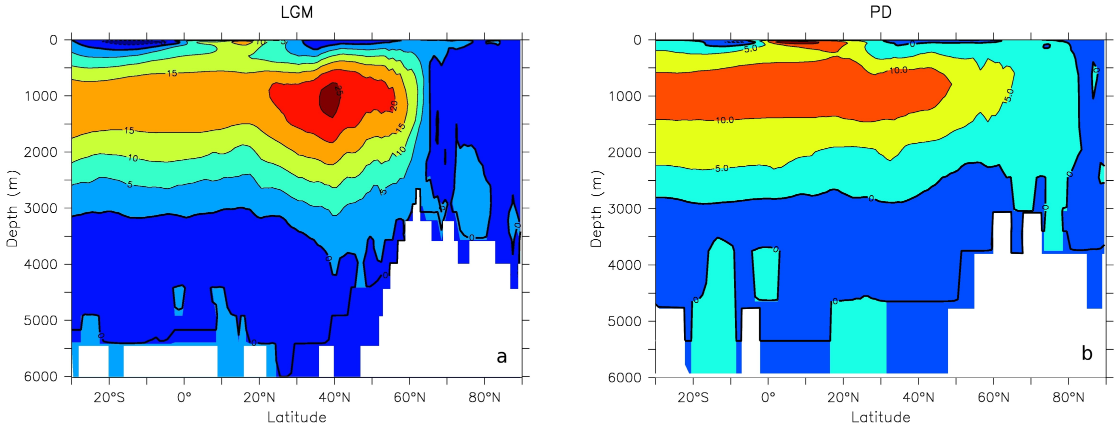

Figure 5.3: Overturning stream-function in the Atlantic (Sv) of the (a) LGM run and (b) present-day reference run. Note the different color scales.

The global zonal average of silicic acid concentration in the LGM run shows a distinct increase in the Antarctic Intermediate Water (AAIW), but a significant decrease in the Antarctic Bottom Water (AABW) compared to the PD run (Figure 5.5). Similar patterns are also found in nitrate distributions. The northward ice extension in the Antarctic during the LGM limits diatom growth under the ice, and thus lessens nutrient depletion in the surface waters. The unused nutrients are carried northward into the sub-Antarctic by Ekman transport and are partly consumed there (see the northward shift of the maximum POC and opal export in the LGM run compared with the PD run in Figure 5.6). Since the POC and BSi export production is reduced approximately by 16% and 25%, respectively, in the Southern Ocean (south of 40 °S) of the LGM run, there are still excess nutrients to be incorporated into the SAMW and the AAIW. These nutrients are further delivered to lower latitudes, promoting increased biological productivity there (Figure 5.6c, d). On the other hand, the diminished opal production under sea-ice in the Southern Ocean during the LGM leads to less BSi export to depth. This explains the decrease in DSi in the lower limb of the thermocline circulation during the LGM compared to the PD simulation.

The global total fluxes of particulate organic carbon (POC) and biogenic opal (BSi) across 90 m depth through sinking of dead organic matter and inorganic shells are 8.6 Pg C yr^{-1} and 88 Tmol Si yr^{-1}, respectively, in the LGM simulation. This is approximately 1.7 Pg C yr^{-1} and 30 Tmol Si yr^{-1} lower than the modern export fluxes. As shown in Figure 5.6, the export fluxes of both POC and BSi are reduced in both the Northern Hemisphere subpolar gyres and the Southern Ocean, probably owing to the equatorward extension of the ice cover in both Hemispheres. More pronounced export production, on the other hand, occurs in the eastern equatorial Pacific, which is very likely a result of increased nutrient supply by SAMW and AAIW originating from the Southern Ocean.

5.3.3 The δ^{30}Si distribution

The annual average value of $\delta^{30}\mathrm{Si}_{\mathrm{DSi}}$ in the upper 90 m ranges from +1 to +3.7‰ in the LGM simulation, which is a slightly larger range than that in the reference run (+1.20 -

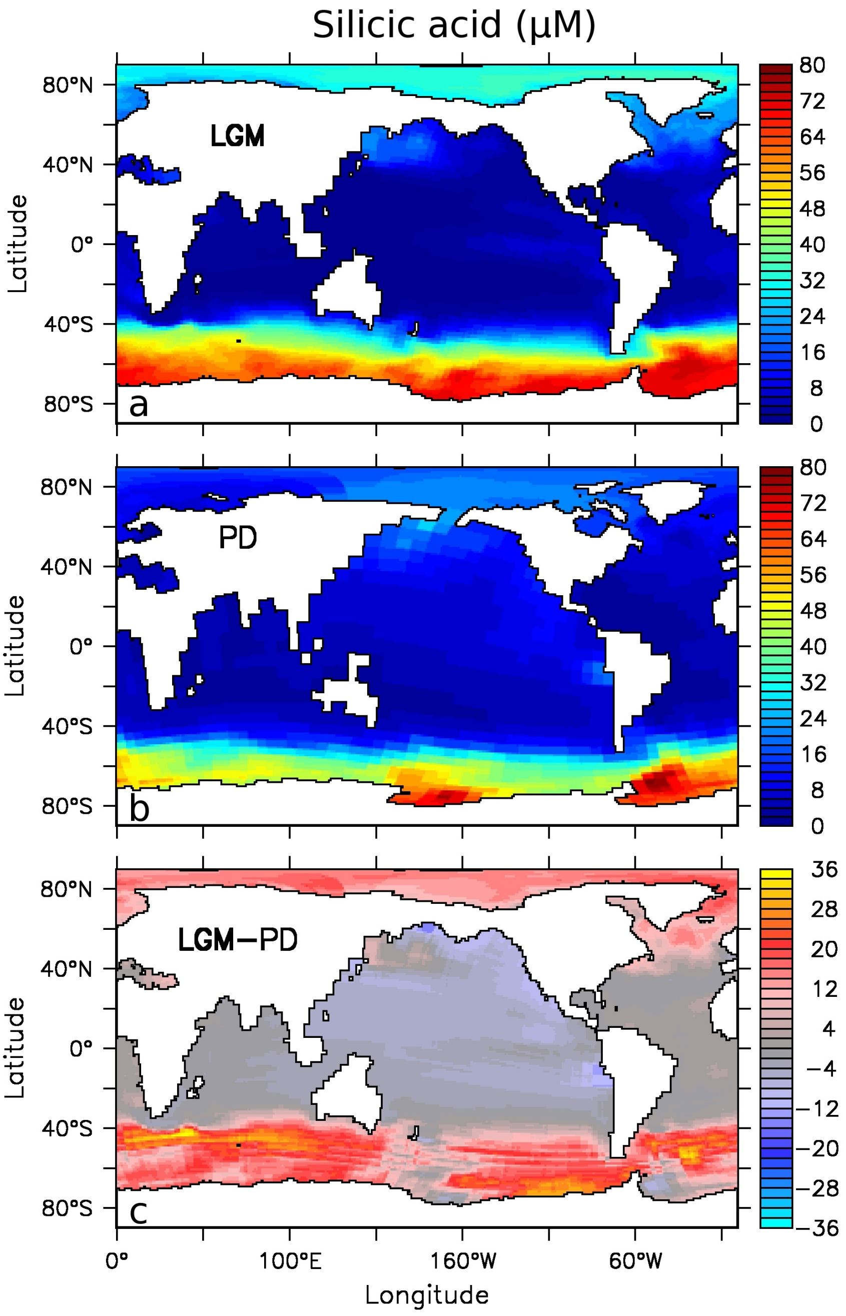

Figure 5.4: Annual mean surface silicic acid concentrations (μmol L^{-1}) in (a) the LGM run, (b) present-day reference run, and (c) difference between the LGM and present-day simulations.

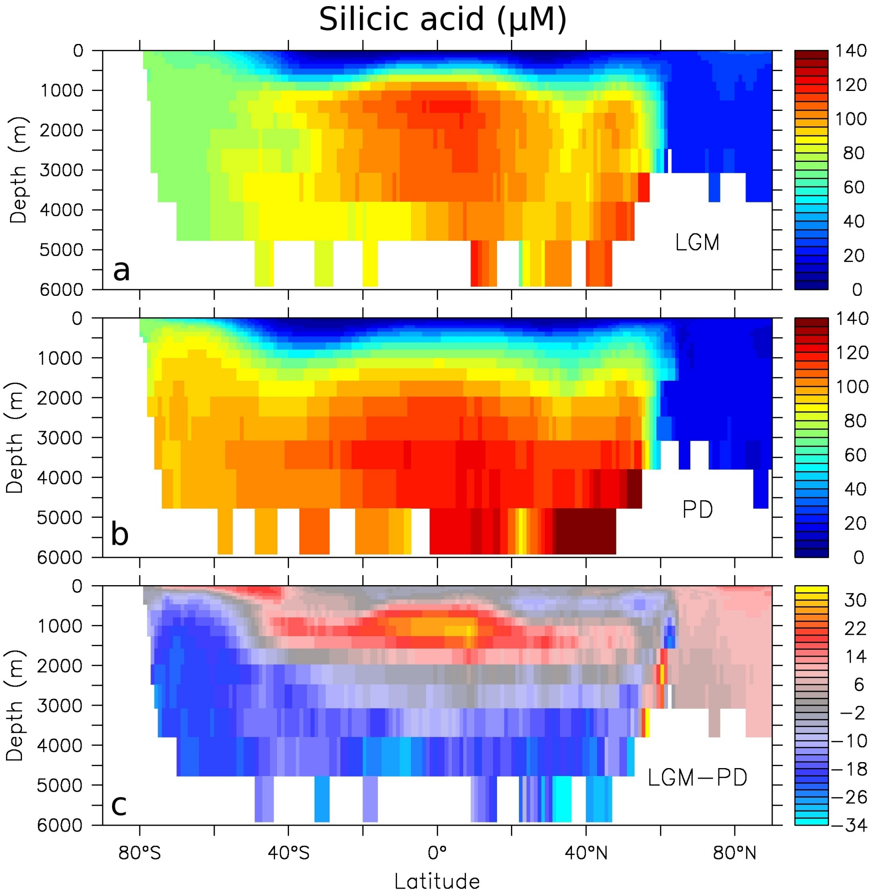

Figure 5.5: Global zonal average of silicic acid concentrations (μmol L^{-1}) in (a) the LGM run, (b) present-day reference run, and (c) difference between the LGM and present-day simulations.

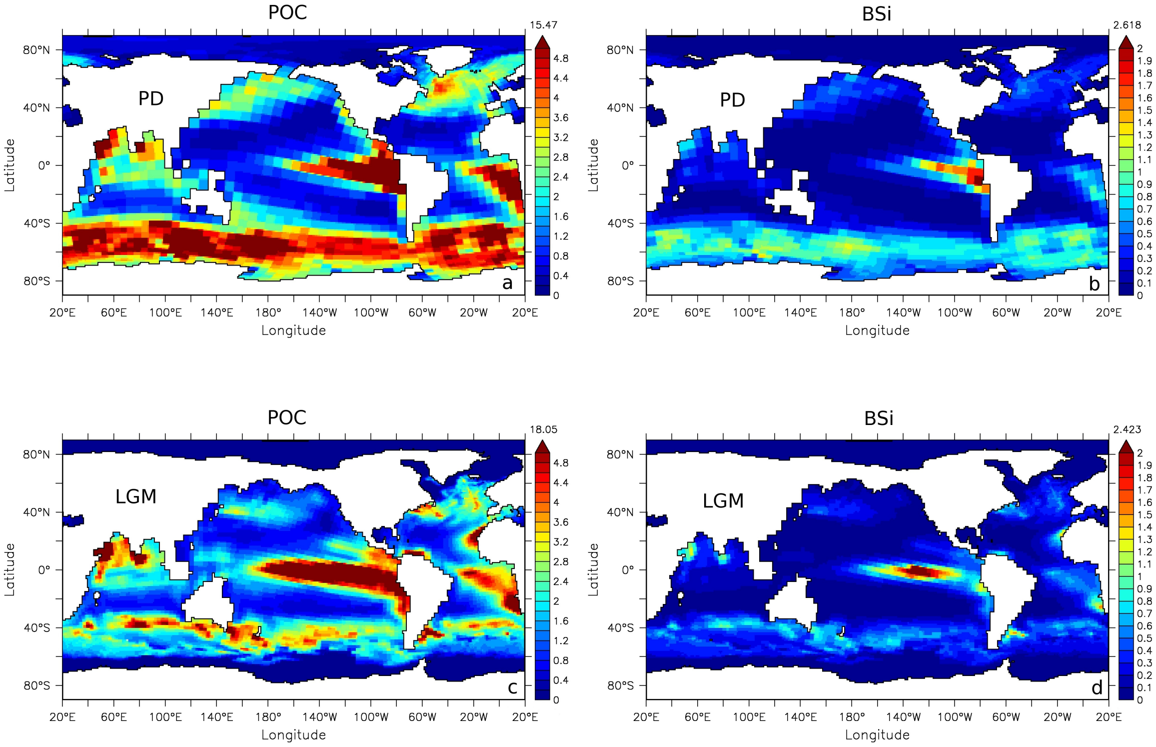

Figure 5.6: Particulate organic carbon export (mol C m^{-2} yr^{-1}) (a, c) and biogenic opal export (mol Si m^{-2} yr^{-1}) (b, d) at 90 m depth of the present-day reference run (a, b) and of the LGM run (c, d).

+3.15‰) (Figure 5.7a, b). The highest values occur in the subtropical gyres, but with an equatorward shift compared to the present-day run, which may be mainly caused by the extension of the ice sheets both in the Arctic and the Antarctic.

The horizontal distribution of $\delta^{30}\mathrm{Si}_{\mathrm{DSi}}$ at 2000 m in the LGM run shows a clear gradient (with ~0.3‰ difference) between the North Atlantic and the North Pacific (Figure 5.8), very similar to the pattern in the modern distribution.

The simulated global average vertical profiles of $\delta^{30}\mathrm{Si}_{\mathrm{DSi}}$ exhibits a shift of ~0.1‰ toward lower values in the upper 2000 m of the LGM run compared to the present-day reference run. A similar shift can be also found in the values of $\delta^{30}\mathrm{Si}_{\mathrm{BSi}}$, but is not constrained only to the upper 2000 m (Figure 5.9).

After 2000 years simulation, the global average $\delta^{30}\mathrm{Si}_{\mathrm{DSi}}$ is approximately 0.03‰ lower than in the PD run, which indicates an overall decrease in silicic acid utilization during the LGM. The lowering of average $\delta^{30}\mathrm{Si}_{\mathrm{DSi}}$ results in a lowering of $\delta^{30}\mathrm{Si}_{\mathrm{BSi}}$ that is produced from silicic acid. This means that the BSi buried permanently in the sediment in the LGM simulation is on average isotopically lighter than that in the PD run. The global average $\delta^{30}\mathrm{Si}_{\mathrm{DSi}}$ in the LGM run is close to a steady state after 2000 model years (remaining trend $<1.7\times10^{-6}$ ‰ yr^{-1}), while this value in the PD run changes by 1.3×10^{-5} ‰ yr^{-1} after the same simulation time.

5.3.4 Summary

We applied the same ocean-biogeochemical model as used for the present-day simulation, with a finer resolution, to simulate the glacial marine silicon cycle and $\delta^{30}\mathrm{Si}$ distribution. The ocean model is driven by atmospheric forcing fields taken from a coupled atmosphere-ocean simulation (*Zhang et al.*, 2013) under LGM climate conditions. The ocean physical state in our simulation is comparable with that in *Zhang et al.* (2013)'s simulation. Surface silicic acid concentrations are higher in both the Southern Ocean and the Arctic Ocean in our LGM simulation compared to the present-day run. The extension of ice sheets in both the Northern and Southern Hemisphere may cause a reduction of phytoplankton growth

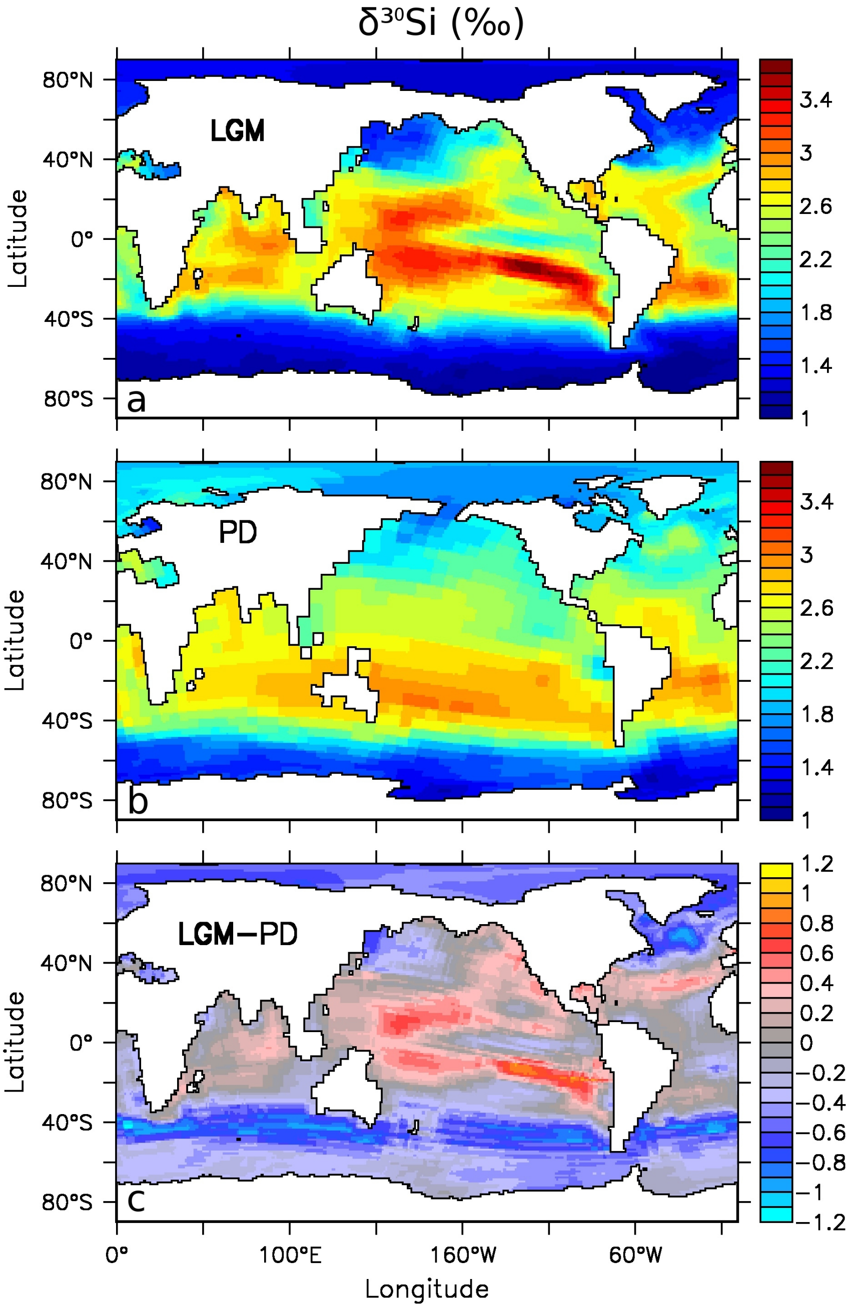

Figure 5.7: The δ^{30}Si of silicic acid (‰) in the surface ocean in(a) the LGM run, (b) present-day reference run, and (c) difference between the LGM and present-day simulations.

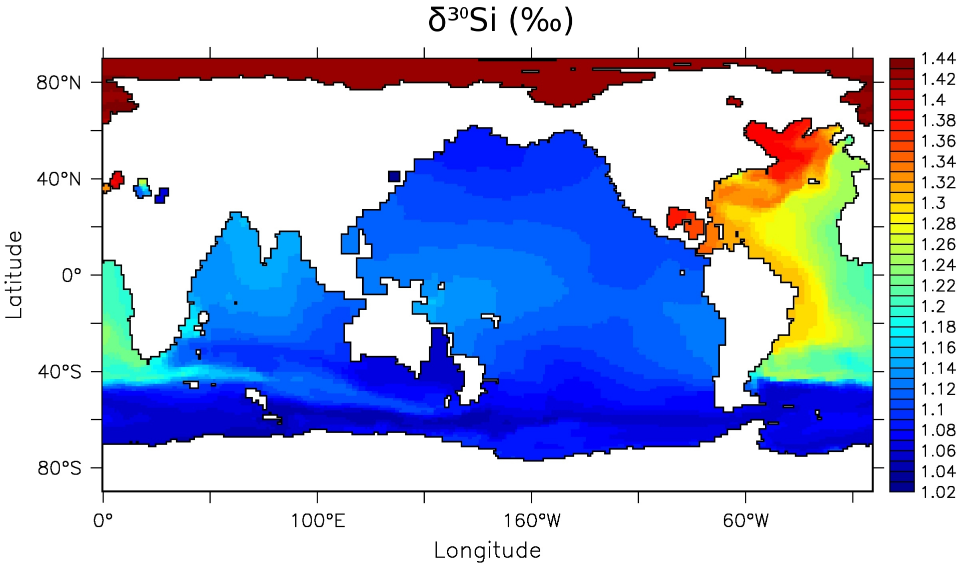

Figure 5.8: The δ^{30}Si of silicic acid (‰) at 2000 m water depth in the LGM run.

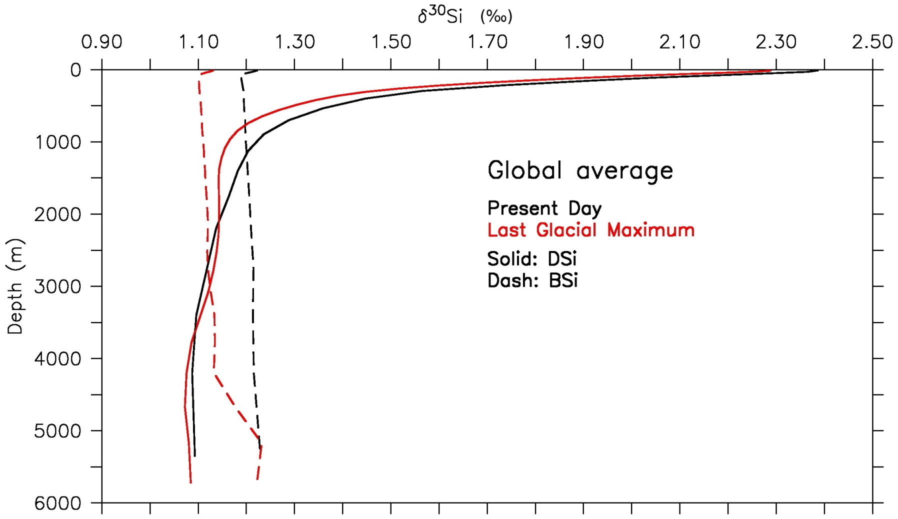

Figure 5.9: The horizontally averaged vertical profiles of δ^{30}Si (‰) of silicic acid (solid lines) and of biogenic silica (dashed lines) in both the LGM (red) and the present-day (black) model runs .

due to reduction of light under sea-ice. Therefore, the silicic acid utilization by diatoms in high latitudes is inhibited, which is in line with the reduced biogenic opal export fluxes in high latitudes of both hemispheres. Our preliminary model results of glacial Si isotopic composition agree with the interpretation from sediment core data by *De La Rocha et al.* (1998) that silicic acid utilization by diatoms in the Southern Ocean during the LGM was diminished relative to the present interglacial. In our model, this is to a great extent due to the northward extension of the ice cover around Antarctica, restraining the diatom growth. The excess nutrients are transported by SAMW and AAIW to low latitudes and support the biological productivity there. Although the model outcome is similar to the silicic acid leakage scenario, the driving mechanism behind it is different. The variable Si:N uptake ratio by diatoms induced by iron limitation is the key factor for the silicic acid leakage hypothesis, but this is not implemented in the current model version. Our model reproduces the diminished silicic acid utilization in the Southern Ocean and the elevated export production in the equatorial area without having a variable Si:N ratio as consequences of iron limitation. The glacial-interglacial variation of iron input into the ocean is represented in our model, but the changes in diatom productivity are largely due to more ice cover in high latitudes.

Chapter 6

Application of a box model to investigate marine δ^{30}Si distributions

6.1 Introduction

The silicon isotopic composition of silicic acid and of biogenic opal is a promising proxy for providing information on the diatom productivity and marine Si cycling both at present and in the geological past. During the last glacial maximum, reduced riverine input of silicate, diminished overturning circulation and perhaps changes of surface mixing strength might have influenced the marine δ^{30}Si signal. Here we apply a simple box model to test the sensitivity of δ^{30}Si to the above-mentioned forcing terms and ocean physical parameters.

6.2 Model setup

We constructed a seven-box model (Figure 6.1) based on the model presented by *Reynolds* (2009). The model includes two deep water boxes, one intermediate water box and four surface water boxes. The two deep water boxes distinguish the Atlantic deep water (derived from the North Atlantic Deep Water, referring as the NADW box) from deep waters of the Southern Ocean, the Indian Ocean and the Pacific (derived from Circumpolar Deep Water, referring as the CPDW box). The intermediate water box (referring as the AAIW box) represents the Antarctic Intermediate Water. The four surface water boxes are the surface Antarctic box, the surface subantarctic box, the low-latitude surface box, and the surface subarctic box, respectively. There is strong mixing between the surface Antarctic box and the CPDW box. The water in the low-latitude surface box is also mixed with the underlying water in the AAIW box.

In this multibox model, it is assumed that the concentration of tracers is homogeneously distributed within each box. Mass exchanges between boxes can be described by a combination of unidirectional overturning flux and bidirectional mixing fluxes (e.g. the Antarctic polar mixing and the low-latitude surface mixing). The particulate opal that is produced in surface boxes sinks down through the underlying boxes. The proportion of opal that dissolves in an individual box is depth dependent and follows the relation $(z/z_0)^{-0.2}$, where z is the depth at the bottom of the box and z_0 is the depth of the box above. This depth dependency (*Reynolds*, 2009) is a variation of the scaling relation for particulate organic carbon from *Martin et al.* (1987), which takes into account that silicon dissolution is slower than organic carbon remineralization. The model parameters (box sizes, water fluxes and opal export fluxes) are the same as used in *Reynolds* (2009)' model (listed in Table 6.1). One modification I made is the addition of riverine input of silicon into the surface ocean and an equal opal burial rate at the ocean bottom. This input and output of Si is set to 5.6 Tmol Si yr^{-1} following the riverine input magnitude reported by (*Tréguer et al.*, 1995). The input flux is located at the low-latitude surface box for simplification. For a detailed description of the parameterization of this model the readers should refer to the work of *Reynolds* (2009).

The model is solved for steady state, indicating that the inputs and outputs for each box in terms of water mass and tracer (Si) mass including isotopic mass (^{28}Si, ^{29}Si, ^{30}Si)

Table 6.1: Parameters used to construct the seven-box model.

Box	Surface area (%)	Area (10^{12} m^2)	Depth at base (m)	Volume (10^{15} m^3)	Water flux (Sv)	τ_{res} (yr)	Opal flux (Tmol yr^{-1})	Export flux per unit area (mol Si m^{-2} yr^{-1})
P	5	17	250	4.4	80	2	15	0.88
S	10	35	250	8.7	20	14	20	0.57
L	75	262	100	26.2	60	14	48	0.18
N	10	35	250	8.7	20	14	16	0.46
M	85	297	1000	262	60	140	-22	-0.08
A	28.5	95	3000	207	7	986	-5	-0.05
D	100	349	3702	775	80	309	-71	-0.20
Average								0.28
Total	100	349		1292			98	

are balanced. The Si isotopic fractionation is formulated as follows,

$$^{30}\mathrm{BSi} =^{28} \mathrm{BSi} \cdot \alpha \cdot \frac{^{30}\mathrm{DSi}}{^{28}\mathrm{DSi}}, \tag{6.1}$$

where α equals 0.9989. The steady state for the silicon isotopic composition in an open system is given by *Fry* (2006)

$$\delta^{30}\mathrm{Si}_{\mathrm{BSi}} = \delta^{30}\mathrm{Si}_{\mathrm{DSi}} + \epsilon \cdot (1 - [X]/[Y]). \tag{6.2}$$

The $[X]$ and $[Y]$ are DSi concentrations of the surface box (where opal production occurs) and of the input flux, respectively; ϵ is the fractionation between BSi and DSi, with a value of -1.1‰.

6.3 Sensitivity of δ^{30}Si to input parameters

6.3.1 Open versus closed system

The seven-box model presented by *Reynolds* (2009) is designed as a closed system with no Si input and sedimentary burial. He argued that external inputs and outputs of Si

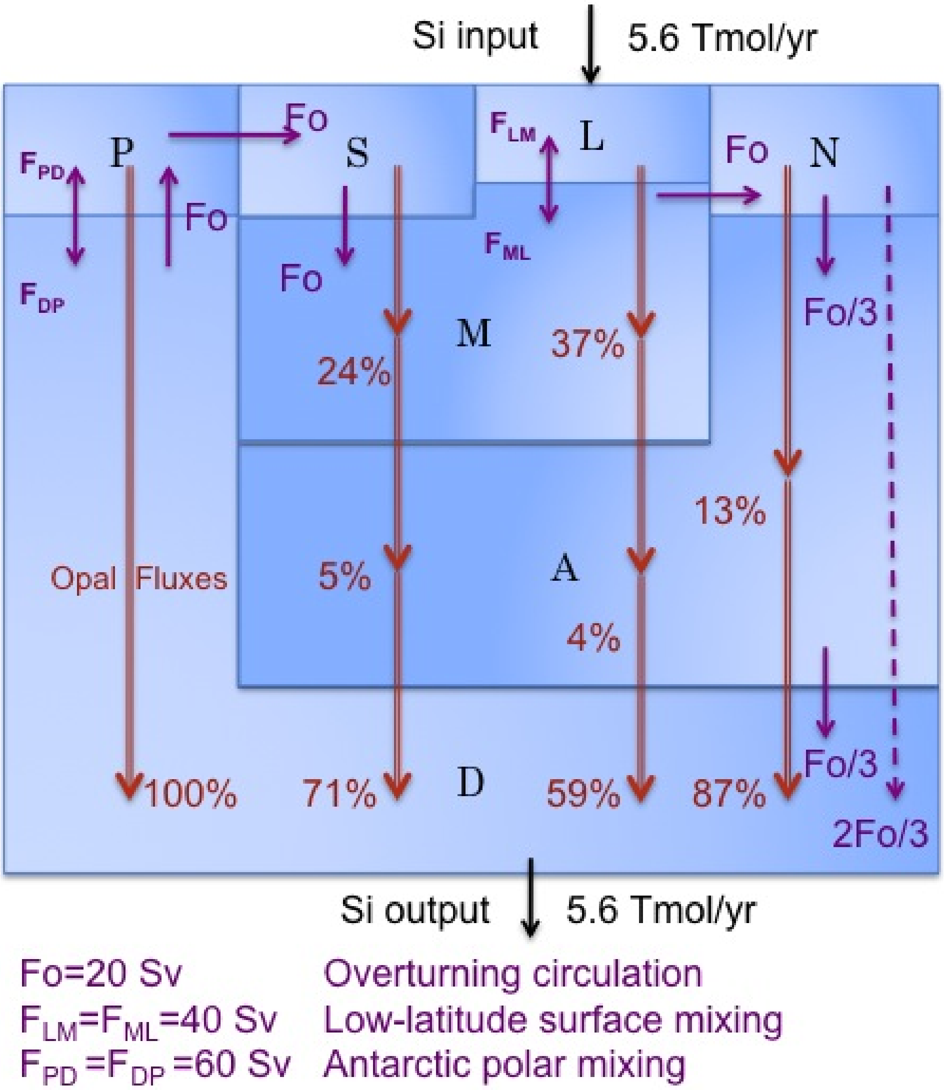

Figure 6.1: Seven-box model. The orange arrows indicate the sinking and dissolution of opal with depth. The purple arrows are water fluxes, where F_o indicates the overturning circulation with a strength of 20 Sv in the reference run. F_{LM} and F_{ML} indicate the low-latitude surface mixing, with a reference strength of 40 Sv. F_{PD} and F_{DP} indicate the Antarctic polar mixing, with a reference strength of 60 Sv. The black arrows are a pair of balanced input and output fluxes of Si, with a value of 5.6 Tmol yr^{-1}. P: Surface Antarctic box; S: Surface subantarctic box; L: Low-latitude surface box; N: Surface subarctic box; M: Antarctic Intermediate Water box; A: North Atlantic Deep Water box; D: Circumpolar Deep Water box.

Table 6.2: The δ^{30}Si values (‰) in different boxes at model equilibrium of the model run by *Reynolds* (2009) (with star) and of our model runs without and with Si input and output. The average values are the volume weighted mean.

	Without Si input and output		Without Si input and output		With Si input and output	
‰	$\delta^{30}\mathrm{Si}_{\mathrm{DSi}}$*	$\delta^{30}\mathrm{Si}_{\mathrm{BSi}}$*	$\delta^{30}\mathrm{Si}_{\mathrm{DSi}}$	$\delta^{30}\mathrm{Si}_{\mathrm{BSi}}$	$\delta^{30}\mathrm{Si}_{\mathrm{DSi}}$	$\delta^{30}\mathrm{Si}_{\mathrm{BSi}}$
P	1.16	0.06	1.16	0.06	1.16	0.06
S	1.48	0.38	1.48	0.38	1.49	0.38
L	2.48	1.38	2.48	1.38	2.47	1.37
N	2.12	1.02	2.13	1.02	2.09	0.99
M	1.38	1.16	1.38	1.04	1.37	1.03
A	1.40	1.03	1.40	1.04	1.38	1.02
D	1.10	0.83	1.10	0.83	1.11	0.83
Average	1.15 (1.24)	0.91 (0.94)	1.25	1.01	1.24	1.00

*The δ^{30}Si values from *Reynolds* (2009)' model run.
The values in brackets are calculated from δ^{30}Si value in each box (weighted by volume) from *Reynolds* (2009)' model; the average values without brackets are taken directly from *Reynolds* (2009).

are not necessary, because the magnitude of ~5 Tmol Si yr^{-1} is too small compared to the large export flux (~120 Tmol Si yr^{-1}) to affect the δ^{30}Si distribution by much. To verify that, we added a balanced input and output of Si into the model. First of all, we repeated *Reynolds* (2009)' model run as a closed system. The δ^{30}Si values resemble his results to a great extent, except one $\delta^{30}\mathrm{Si}_{\mathrm{BSi}}$ value in box M (Table 6.2). We further compared the global average value of $\delta^{30}\mathrm{Si}_{\mathrm{DSi}}$ in both our model runs with and without Si in- and output. The result shows only ~0.01‰ difference between the open and closed system. We can therefore confirm that addition of a surface input term and opal output term to the model would not strongly influence the overall δ^{30}Si signature in the ocean at steady state.

6.3.2 Marine overturning circulation

We test sensitivities of δ^{30}Si to the overturning circulation strength ranging from 0.5 to 1.5 times of the reference strength of 20 Sv (Figure 6.2). A weaker overturning circulation (10 Sv) results in a slightly higher averaged $\delta^{30}\mathrm{Si}_{\mathrm{DSi}}$, mainly due to a greater opal production in the Antarctic surface water. The change in overturning circulation strength shifts

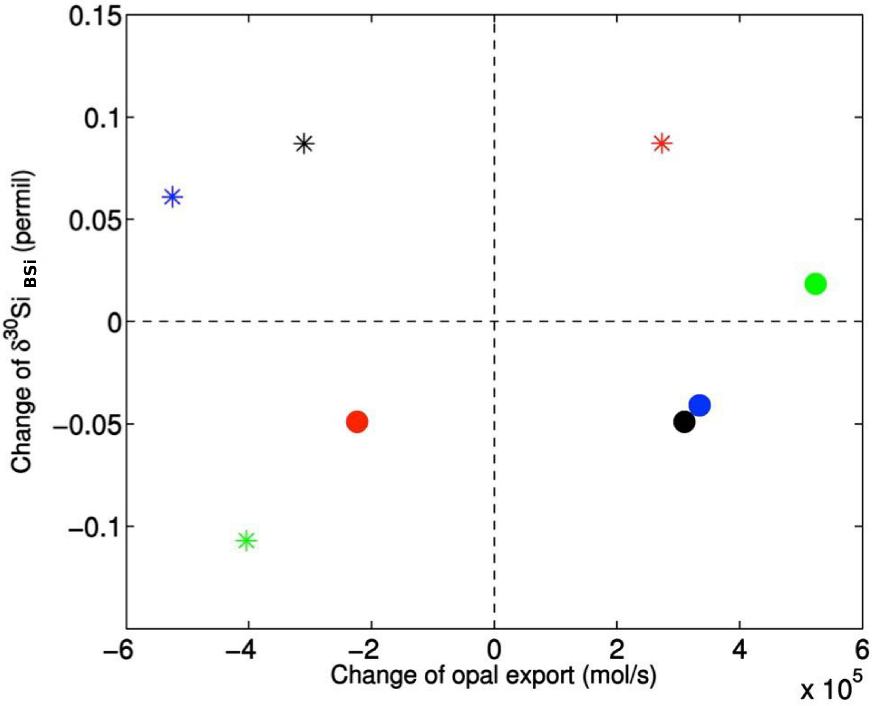

Figure 6.2: Change of opal export versus change of $\delta^{30}\mathrm{Si}_{\mathrm{BSi}}$ in ocean surface boxes with enhanced and diminished overturning circulation strength. Circle: 30 Sv (1.5 × 20 Sv); Star: 10 Sv (0.5 × 20 Sv); Red: Surface Antarctic (box P); Black: Surface subantarctic (box S); Blue: Low-latitude surface water (box L); Green: Surface subarctic (box N).

the silicic acid concentration among the AAIW, NADW and CPDW. The CPDW with a higher concentration upwells into the Antarctic surface water, supporting a higher opal production there. The heavier $\delta^{30}\mathrm{Si}_{\mathrm{DSi}}$ signal of Antarctic surface water is transported into subantarctic waters, resulting in a higher $\delta^{30}\mathrm{Si}_{\mathrm{DSi}}$ also in the subantarctic surface water, although the opal production there decreases. This demonstrates that changes in $\delta^{30}\mathrm{Si}_{\mathrm{BSi}}$ should not necessarily be interpreted as a local signal. The weaker overturning circulation also results in an elevated $\delta^{30}\mathrm{Si}_{\mathrm{BSi}}$ in the low-latitude surface water box despite the diminished opal export in this box. In the low-latitude surface water box, the utilization of silicic acid is set to 100%, meaning that all the Si input into this box is converted to opal production. The output $\delta^{30}\mathrm{Si}_{\mathrm{BSi}}$ thus equals the $\delta^{30}\mathrm{Si}$ value of the input DSi, resulting in zero fractionation.

6.3.3 Sea surface mixing strength

We test sensitivities of δ^{30}Si to the strength of both low-latitude and Antarctic polar mixing, with a range from 0.5 (0.7 for low-latitude mixing) to 2 times of the reference strength of 40 Sv and 60 Sv, respectively. A stronger low-latitude mixing brings more nutrients to the ocean surface, which benefits opal export production. The enhanced opal export results in a higher DSi concentration from the opal dissolution in the lowermost box (D: Circumpolar Deep Water box). The higher DSi concentration fuels the opal production also in the Antarctic surface water through deep mixing (Figure 6.3d). Consequently, the higher production in both low-latitude surface water and the Antarctic surface water elevates the $\delta^{30}\mathrm{Si}_{\mathrm{DSi}}$ value both locally and globally (average value) (Figure 6.3b).

On the other hand, a stronger Antarctic polar mixing increases the opal production only within the Antarctic surface water box (Figure 6.3c). Although the magnitude is small, there is a slight increase in $\delta^{30}\mathrm{Si}_{\mathrm{DSi}}$ in all boxes, certainly also in the global average value (Figure 6.3a). This can be explained by the transport of the $\delta^{30}\mathrm{Si}_{\mathrm{DSi}}$ signal preformed in the Antarctic surface water to other water masses through the overturning circulation. This outcome implies that the production process taking place in the Antarctic surface water potentially has a global impact.

6.3.4 Summary

Our results indicate that a slower overturning circulation can result in a higher globally averaged δ^{30}Si of silicic acid, which is mainly due to a greater productivity in the surface Antarctic. Despite a decrease in subantarctic productivity, the δ^{30}Si of opal follows the increase of the Antarctic, demonstrating that changes in opaline δ^{30}Si should not necessarily be interpreted as a local signal. A stronger low-latitude mixing brings more nutrients to the ocean surface, boosting the opal export production. This together with the increase in opal production in the Antarctic surface water, may cause an increase in the averaged global $\delta^{30}\mathrm{Si}_{\mathrm{DSi}}$ value. On the other hand, a stronger Antarctic polar mixing

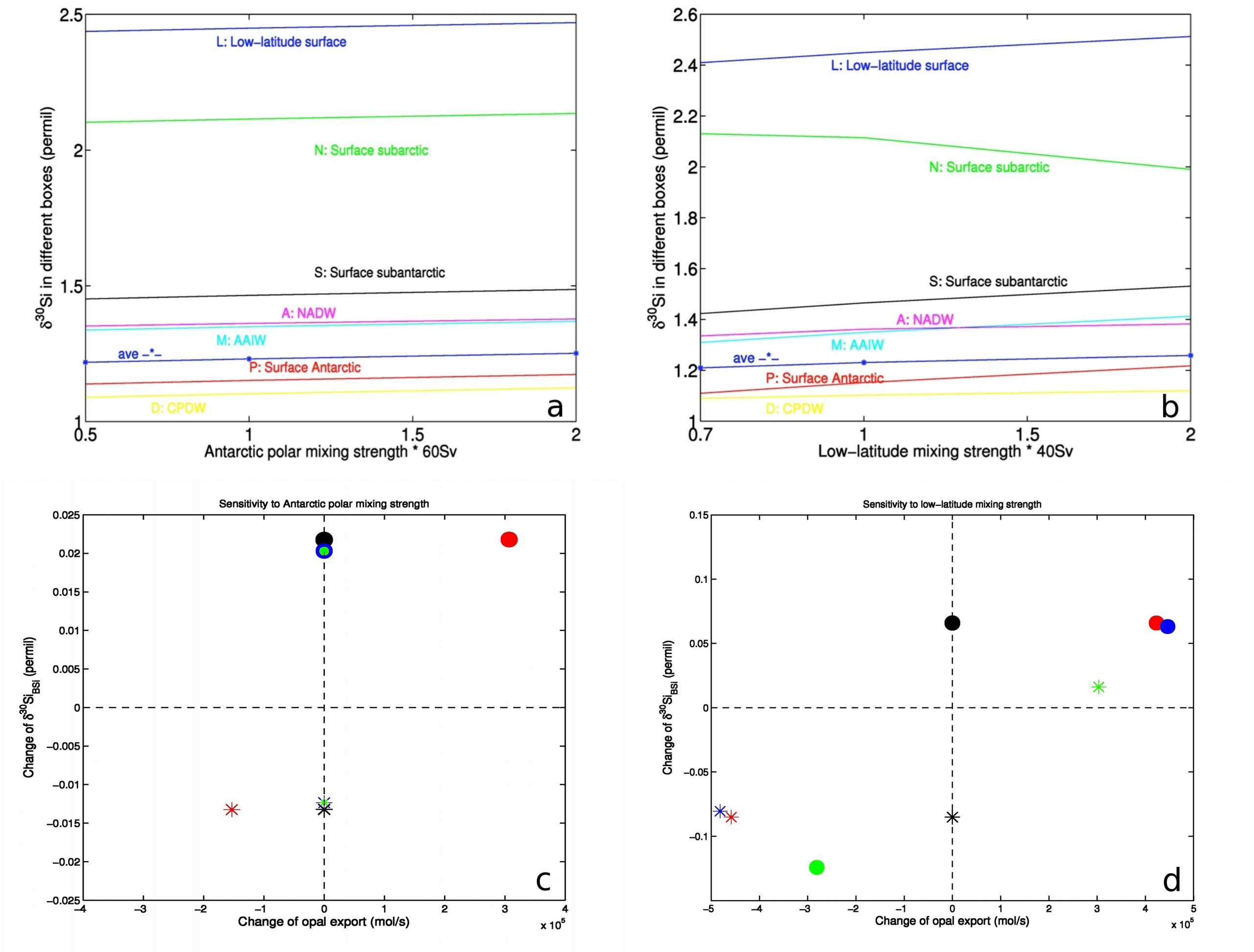

Figure 6.3: Change of $\delta^{30}\mathrm{Si}_{\mathrm{DSi}}$ in different model boxes with change of Antarctic mixing strength (a) and Low-latitude mixing strength (b). The change of $\delta^{30}\mathrm{Si}_{\mathrm{BSi}}$ in ocean surface boxes is shown as a function of the according change in opal export production. (c) Circle: 120 Sv (2 × 60 Sv); Star: 30 Sv (0.5 × 60 Sv); (d) Circle: 80 Sv (2 × 40 Sv); Star: 28 Sv (0.7 × 40 Sv) (When the strength is decreased to 0.5 × 40 Sv, the model becomes unstable.) Color code in (c) and (d) is the same as in (a) and (b).

does not affect $\delta^{30}\mathrm{Si}_{\mathrm{DSi}}$ very much in magnitude, but the influence has a global impact. Another conclusion we can draw is that an addition of today's riverine input and opal burial to the model does not change the average $\delta^{30}\mathrm{Si}_{\mathrm{DSi}}$ value much (< 0.015‰), because the input of silicate is small in magnitude compared with opal export fluxes.

Chapter 7

Summary and Outlook

7.1 Summary

The marine silicon cycle has received intense scientific attention over the past two decades, besides the cycles of carbon and nitrogen. The silicon cycle is closely connected to diatom growth, which is responsible for up to half of the modern oceanic primary production. Especially in areas such as the Southern Ocean, the drawdown of dissolved inorganic carbon by diatoms is crucial for controlling the atmospheric CO_2 concentration. A few questions that are the subject of active research are: "Has the diatom production in the Southern Ocean been higher or lower in the Last Glacial Maximum (LGM) compared to the present interglacial? What can we learn from the modern silicon cycle for a reconstruction of diatom production in the past and what are the main controlling factors in the silicon cycle? If the ocean circulation was different in the Last Glacial Maximum, what would be the consequences for marine biogeochemical cycles and diatom productivity?". One mean to study the marine silicon cycle and the productivity by diatoms both for the present and in the geological past is the isotopic composition δ^{30}Si of silicic acid and of biogenic opal. Plenty of laboratory and field studies have been conducted to quantify the magnitude of silicon isotopic fractionation during opal formation and/or dissolution, or the extent to which the δ^{30}Si is influenced by various biological, chemical and physical factors. However, modeling studies that can verify our understanding of the mechanism behind the distribution and behavior of δ^{30}Si are so far only a few.

The current study aims to contribute to a mechanistic understanding of δ^{30}Si as a proxy for the reconstruction of marine silicic acid utilization and primary production by diatoms both at present and in the geological past. An ocean general circulation model (MPI-OM) coupled with a biogeochemical model (HAMOCC5.1) is applied to simulate the marine silicon cycle and the silicon isotopic composition in it. An interactive sediment module is included so that the biogenic opal redissolution and accumulation in the sediment can be simulated, making the model an open system in terms of silicon in- and output. The silicon isotope ^{30}Si and the process of fractionation during both opal production and dissolution have been added to the HAMOCC model. With this model a comprehensive δ^{30}Si distribution of silicic acid and biogenic opal is produced and is compared with the available observation data for the present. For the first time, also the marine δ^{30}Si distribution under LGM climate conditions is simulated via a coupled ocean-biogeochemical model. In addition, the sensitivity of δ^{30}Si to various glacial-interglacial ocean physical parameters such as the strength of overturning circulation and ocean surface mixing is tested using a simple seven-box model. In brief, in this thesis I present a global pattern of oceanic and sedimentary δ^{30}Si distributions both under present-day and the LGM climate conditions and discuss the possible controlling mechanisms.

I simulated the δ^{30}Si distribution under the present-day climate condition (with pre-industrial atmospheric CO_2 concentration of 278 ppm), assuming that Si fractionation only occurs during the formation of biogenic opal but not during its dissolution (referred to as model run NoFD). Despite the coarse model resolution, the model results are in good agreement with the observed distribution patterns of silicic acid concentration, particulate organic carbon (POC) export and biogenic opal export production. Near the surface, there is a Rayleigh-like relationship between the concentration of silicic acid and its isotopic composition δ^{30}Si within different ocean basins. The surface $\delta^{30}\text{Si}_{\text{DSi}}$ increases during the utilization of silicic acid by diatoms following a Rayleigh-type distillation, which demonstrates the primary control of biological fractionation on the surface $\delta^{30}\mathrm{Si}_{\mathrm{DSi}}$ distribution. However, the Rayleigh-type distillation curves for different ocean basins are different from what one would expect from the pure biological fractionation. The variations among the Rayleigh curves indicate an impact of physical transport and mixing of water. At latitudes higher than 40 ° of both the Northern and Southern Hemisphere, we find that the surface $\delta^{30}\mathrm{Si}_{\mathrm{DSi}}$ is seasonally dependent and inversely related to DSi concentration and mixed layer depth. The surface $\delta^{30}\mathrm{Si}_{\mathrm{DSi}}$ peaks approximately four months after the BSi export reaches its maximum. These findings further demonstrate that the biological fractionation and the physical mixing are two major controlling factors of the surface $\delta^{30}\mathrm{Si}_{\mathrm{DSi}}$. In the deep ocean, our model reproduces a significant silicon isotopic gradient between the North Atlantic and the North Pacific, which agrees with the in situ measurements by *De La Rocha et al.* (2000) and modeling studies by *Reynolds* (2009) and *Matsumoto et al.* (2013). The advection related to the thermohaline circulation is thought to be the essential controlling factor for deep ocean $\delta^{30}\mathrm{Si}_{\mathrm{DSi}}$. The pattern of $\delta^{30}\mathrm{Si}_{\mathrm{BSi}}$ on the sediment surface in our model is more close to the pattern of $\delta^{30}\mathrm{Si}$ of BSi that sinks out of the euphotic zone (crossing 90 m) rather than that of $\delta^{30}\mathrm{Si}_{\mathrm{BSi}}$ averaged in the upper (50 m) water layers, especially along the Equator. This might be attributed to the shallower surface mixed layer depth (<50 m, sometimes even less than 10 m) induced by the permanent upwelling in the equatorial regions that prevents the surface $\delta^{30}\mathrm{Si}_{\mathrm{BSi}}$ from mixing with the deeper signals. This result suggests caution when using the sedimentary $\delta^{30}\mathrm{Si}_{\mathrm{BSi}}$ to reconstruct the surface diatom production in regions with special hydrographic conditions. A comprehensive comparison is conducted between the measured and modeled DSi concentrations and $\delta^{30}\mathrm{Si}_{\mathrm{DSi}}$ both in the surface water and in the deep water, taking advantage of the fast growing number of $\delta^{30}\mathrm{Si}$ measurements in the last decade. The results show a high degree of agreement between the simulation and the observation, given such a coarse resolution model. The ability of the model to reproduce the large-scale modern oceanic $\delta^{30}\mathrm{Si}$ distribution gives us some confidence in simulating the $\delta^{30}\mathrm{Si}$ during the last glacial maximum.

In the second part of the present-day simulation, we assume that Si fractionation occurs not only during the formation of diatom frustules but also during their dissolution (referred as model run FD). A laboratory work by *Demarest et al.* (2009) has shown that the dissolved silicon during biogenic silica dissolution has a δ^{30}Si value that is consistently 0.55‰ lower than that of its parent material over a wide variety of biogeochemical conditions. This implies a fractionation ϵ of -0.55‰ during biogenic opal dissolution. The study by *Demarest et al.* (2009) offers an alternative explanation for the in situ measured Δ^{30}Si ($\delta^{30}\mathrm{Si}_{\mathrm{BSi}}$ - $\delta^{30}\mathrm{Si}_{\mathrm{DSi}}$) that departs from -1.1‰, other than the physical mixing. An interesting feature of the δ^{30}Si distribution in model run FD is that in the water column the averaged $\delta^{30}\mathrm{Si}_{\mathrm{DSi}}$ value is lower compared to model run NoFD, while in the sediment $\delta^{30}\mathrm{Si}_{\mathrm{BSi}}$ is higher in most areas than that in model run NoFD. As dissolution of BSi discriminates against the release of the heavier isotopes of silicon in model run FD, the isotopic composition of BSi increases with water depth and further in the sediment through dissolution. This causes release of relatively light isotopes into the water column and burial of relatively heavier isotopes into the sediment compared with model run NoFD. Thus, the average $\delta^{30}\mathrm{Si}_{\mathrm{DSi}}$ of the ocean shifts toward a lower value and the $\delta^{30}\mathrm{Si}_{\mathrm{BSi}}$ of the sediment shifts then toward a higher value. The vertical profiles of $\delta^{30}\mathrm{Si}_{\mathrm{DSi}}$ from both model runs are compared with in situ measurements by (*de Souza et al.*, 2012b). The results from model run NoFD are in good agreement with the measurements, while results from model run FD are obviously lower than the in situ data at all water depths. The model-data comparison implies that currently the usage of fractionation during BSi dissolution as explanation to δ^{30}Si distribution is still speculative. More mechanistic studies of fractionation associated with BSi dissolution and the influence of diatom dissolution pattern on the fractionation effect need to be done.

We performed a simulation for the last glacial maximum, forcing the ocean model with atmospheric fields from a coupled ocean-atmosphere climate model run (*Zhang et al.*, 2013). In the LGM simulation, surface silicic acid concentrations are higher in both the Southern Ocean and the Arctic Ocean compared to the present-day run. The extension of sea-ice cover in both the Northern and Southern Hemisphere reduces phytoplankton growth due to low light under the ice. Therefore, the silicic acid utilization by diatoms in high latitudes is inhibited, in line with reduced biogenic opal export fluxes in high latitudes of both hemispheres. Our preliminary model results of Si isotopic composition agree with the interpretation from sediment core data by *De La Rocha et al.* (1998) that silicic acid utilization by diatoms in the Southern Ocean during the LGM was diminished relative to the present interglacial. In our model, this is to a great extent due to the northward extension of the ice cover around Antarctica, restraining the diatom growth. The excess nutrients are transported by intermediate and mode water to low latitudes and boost the biological productivity there. Although the model outcome is similar to the silicic acid leakage scenario (*Nozaki and Yamamoto*, 2001), the driving mechanism behind it is different. The variable Si:N uptake ratio by diatoms induced by iron limitation is the key factor for the silicic acid leakage hypothesis, but this is not implemented in the current model version. Nevertheless, the model produces a diminished silicic acid utilization in the Southern Ocean and elevated export production in the equatorial area without having a variable Si:N ratio (changes in phytoplankton stoichiometry), but only via changes in the distribution and strength of biological productivity .

During the last glacial maximum, reduced riverine input of silicate, diminished overturning circulation and perhaps changes of surface mixing strength would have had influences on the marine δ^{30}Si signal. A simple seven box model is applied to test the sensitivity of δ^{30}Si to different parameters describing ocean circulation. Our results indicate that a slower overturning circulation can result in a higher globally averaged δ^{30}Si of silicic acid, which is mainly due to a greater productivity in the Southern Ocean (south of ~60 °S). Despite a decrease in subantarctic productivity (between 45 °S and 60 °S), the $\delta^{30}\mathrm{Si}_{\mathrm{BSi}}$ in the subantarctic increases following the increase of the $\delta^{30}\mathrm{Si}_{\mathrm{DSi}}$ in the Southern Ocean (south of ~60 °S), demonstrating that changes in opaline δ^{30}Si should not necessarily be interpreted as a local signal. A stronger low-latitude mixing brings more nutrients to the ocean surface, boosting the opal export production there. This together with the increase in opal production in the Antarctic surface water, may cause an increase in the averaged global $\delta^{30}\mathrm{Si}_{\mathrm{DSi}}$ value. On the other hand, a stronger Antarctic polar mixing does not affect the average $\delta^{30}\mathrm{Si}_{\mathrm{DSi}}$ very much, but the influence has a global impact. Another conclusion we can draw is that an addition of today's riverine input and opal burial to the model does not change the average $\delta^{30}\mathrm{Si}_{\mathrm{DSi}}$ value much (< 0.015‰), because the input of silicate is small in magnitude compared with opal export fluxes.

7.2 Outlook

A relatively coarse resolution (~6 °) is used for the present-day simulation, because of the expensive computation and long equilibrium time. A simulation with a finer resolution may improve the nutrient distribution by avoiding high diffusivity, especially in the regions like the Southern Ocean, which is important for understanding the glacial-interglacial $p\mathrm{CO}_2$ variations. In the glacial simulation, the globally averaged nutrient concentrations have been kept at the same values as in the present-day run, in order to eliminate the influence from changing concentrations when comparing with the modern distribution. However, the nutrient concentrations might have been higher in the LGM due to a reduction of water volume in the ocean by ~3% caused by massive ice sheet formation and/or enhanced input of material exposed on shelves into the ocean. It might therefore be interesting to investigate the effects of changes in the total nutrient inventory on the distribution of stable Si isotopes. To implement a variable Si:N uptake ratio by diatoms into the model may allow us to further test the silicic acid leakage hypothesis and to quantify the influence of different biogeochemical and physical factors on the silicic acid distribution during the LGM. However, little is known on whether changes in diatom Si:N ratio induced by iron limitation also affect silicon isotope fractionation. An exciting perspective of this work is to compare the modeled sedimentary $\delta^{30}\mathrm{Si}$ with the available sediment core data both for present day and the LGM, although the uncertainty both from the model and the observations may remain large.

Modeling is a powerful tool for promoting a mechanistic understanding of the marine biogeochemical proxy δ^{30}Si. It produces comprehensive distributions of δ^{30}Si both in the ocean and in the sediment with low cost. The biological, chemical and physical factors that affect δ^{30}Si distributions can be tested separately or together. The dramatically increasing complexity of models reflects our understanding of the climate system. This work is just a tiny piece of the puzzle. Eventually, this type of modeling approach, together with laboratory work to understand mechanisms, and field work will add up to a full picture of climate and its historical and future changes.

Supplementary Information: Sensitivity tests for the global Si cycle

The marine silicon cycle receives input of silicon from continental sources, mainly through rivers. At the same time it loses silicon through permanent burial of biogenic silica in the sediments. Over long enough time-scales, on the order of a few times the residence time of roughly 10,000 years, the production and sedimentation of biogenic silica adjusts in such a way that inputs and losses balance and steady state is reached. A large number of models disregard oceanic sources and sinks of silicon and treat the ocean as a closed system. In that case, an equilibrium steady state distribution of silicate in the ocean is reached within a few thousand years. The HAMOCC model, in contrast, is designed in such a way that it is feasible to implement a riverine input and a burial loss term of nutrients into and out of the ocean-sediment system. The riverine input of silicon is equally distributed at the sea surface and the output is as burial of biogenic silica into a permanent burial layer, below the lowermost sediment layer in the model. In order to obtain a realistic silicic acid distribution at the model steady state, a rough estimation of the input flux of silicon is needed. This is usually done by running the model without input term for e.g. 1000 model years, and then take the magnitude of output flux as that for input. Besides a balanced input and output term, there are several other parameters which determine how fast the model will reach an equilibrium and how close the silicate distribution at steady state will be to the observed distribution. They are the initial value and distribution of silicate in the ocean, silicate uptake half-saturation constant, sinking speed of opal, dissolution rate of opal both in the ocean and in the sediment and silicate saturation concentration in the sediment.

With the original setting, the silicic acid concentration is overestimated in surface waters and underestimated in deep waters compared to the World Ocean Atlas 2009 dataset. A realistic silicic acid distribution is essential for determination of the δ^{30}Si distribution. Therefore, we conducted a series of sensitivity tests in order to obtain a more realistic Si cycle. Each of the sensitivity experiments was run for at least 1000 model years. The aim of this documentation is to give an overview of the sensitivity experiments we conducted and to show the steps toward a better match of the horizontally averaged vertical profile of silicic acid with the WOA09 dataset, rather than a detailed description of each experiment.

◊ Sensitivity tests for opal sinking speed

- Increase of opal sinking speed

  The sinking speed of opal is increased from 10 m d^{-1} to 20 and 30 m d^{-1}, in order to get less opal dissolution in the upper ocean.

- Depth dependent sinking speed

  We add an optional sinking term for biogenic opal that is depth dependent as used in the REcoM model. The opal sinking speed increases linearly from 20 m d^{-1} at the surface to 164 m d^{-1} at 5000 m depth (*Kriest et al.*, 2012). The reasoning for this assumption is that opal shells become associated with aggregates of organic and anorganic matter, therefore the sinking speed is getting higher with depth.

  The results from these two tests with increased sinking speed are compared with the WOA09 dataset and the results with varying opal dissolution rate (Figure S.1).

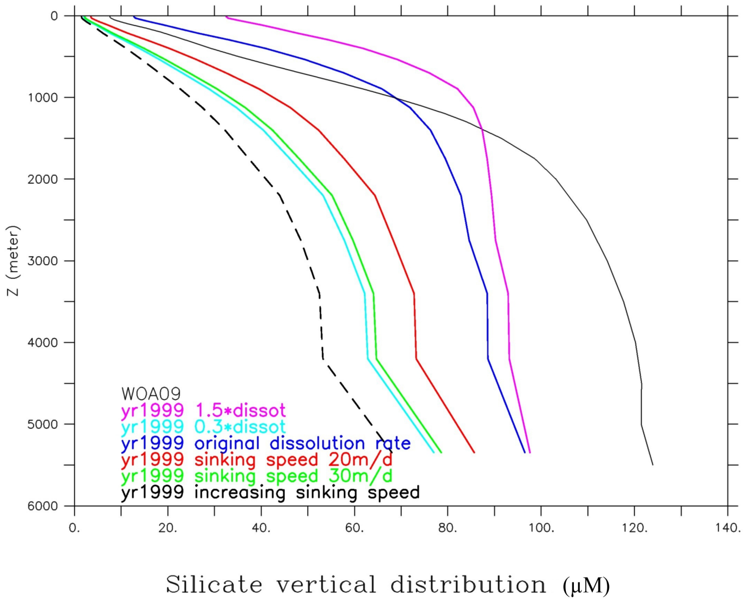

Figure S.1: The horizontally averaged vertical profiles of silicic acid with varying opal dissolution rate and sinking speed.

◇ Sensitivity tests for opal saturation concentration in the sediment combined with varying sinking speed

- Increase of opal saturation concentration by a factor of 1.5

  The opal saturation concentration is increased from 1000 μmol L^{-1} to 1500 μmol L^{-1} combined with the original opal sinking speed of 10 m d^{-1} and the increased sinking speed of 20 m d^{-1}.

- Increase of opal saturation concentration by a factor of two

  The opal saturation concentration is increased from 1000 μmol L^{-1} to 2000 μmol L^{-1} combined with the original opal sinking speed of 10 m d^{-1} and the increased sinking speed of 20 m d^{-1}.

The influence of saturation concentration (Figure S.2) is smaller than that of the opal sinking speed.

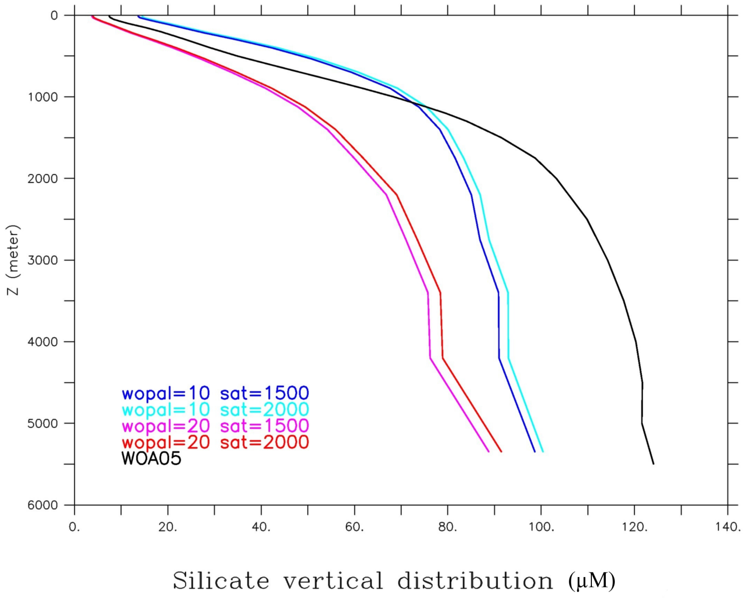

Figure S.2: The horizontally averaged vertical profiles of silicic acid with varying opal saturation concentration in the sediment combined with varying opal sinking speed.

◇ Sensitivity tests for the initial concentration and distribution of silicate in the ocean

- Variation of the initial silicic acid concentration

  The global average initial silicic acid concentration is changed from 120 μmol L^{-1} to 95 μmol L^{-1}.

- Variation of the initial silicic acid distribution

  The homogenous distribution of initial silicic acid concentration is changed to a horizontally averaged vertical profile of silicic acid concentration derived from the WOA09 dataset.

  The results from these two tests are compared with model runs with varying opal dissolution rate in the ocean (Figure S.3).

♢ Sensitivity tests for silicate uptake half-saturation constant

- Increase of the silicate uptake half-saturation constant

  The silicate uptake half-saturation constant is increased from 1 to 4 μmol L^{-1} (Figure S.3) in order to avoid too much silicic acid to be drawn out of the surface water.

♢ Sensitivity tests for the opal dissolution rate in the ocean

- Temperature-independent dissolution rate of opal

  A temperature-independent dissolution rate of 0.01 d^{-1} combined with an opal sinking speed of 10 m d^{-1} is tested. In this case, when T $>$ 17 °C (surface ocean), the dissolution rate is lower than the original rate; when T $<$ 17 °C (deep ocean), the dissolution rate is higher than the original one (Figure S.4).

- Increase of the temperature-dependent dissolution rate by a factor of 1.5

  $K = 1.5 \times constant \times 0.1 \times (T + 3)$; $constant = 0.01$ d^{-1}

- Decrease of the temperature-dependent dissolution rate by a factor of 0.3

  $K = 0.3 \times constant \times 0.1 \times (T + 3)$; $constant = 0.01$ d^{-1}

- Application of the dissolution rate formulation from HAMOCC4

  $K = constant \times (T + 2)$; $constant = 3.3 \times 10^{-4}$ d^{-1}

  The last three model runs are initialized with horizontally averaged profiles of Si, N and P from the WOA09 dataset instead of homogeneous initial values. The silicate uptake half-saturation constant is changed from 1 to 4 μmol L^{-1}. The results from these model runs are compared with the WOA09 dataset and the original profile (Figure S.5).

- Application of the dissolution rate from *Kamatani* (1982)

  The opal dissolution rate derived from *Kamatani* (1982) can be expressed as $K = A \cdot exp(b \cdot T)$. K is the dissolution rate (d^{-1}), A is a species-dependent constant (d^{-1}), b is 0.0833 ($^{\circ}\mathrm{C}^{-1}$), and T is temperature ($^{\circ}$C). The full range of A is 7.5×10^{-4}-1.5×10^{-2} according to the data from *Kamatani* (1982). This results in opal dissolution rates at 20 °C varying between 0.004 d^{-1} and 0.08 d^{-1}. As the frustules in the experiments by *Kamatani* (1982) were washed to remove organics, the in-situ dissolution is likely lower. Assuming the average marine surface temperature is $T = 15\,^{\circ}\mathrm{C}$, we want dissolution rate in the surface water to be 0.01 d^{-1}. Then we get $A = 0.01 \times exp(-0.0833 \times 15)$, which is roughly 3.0×10^{-3} d^{-1}. We tested A in the range of 1.0×10^{-3}-3.0×10^{-3} d^{-1} (Figure S.6).

◇ Sensitivity tests for the opal dissolution rate in the sediment

- Increase of the opal dissolution rate in the sediment

  The dissolution rate of opal in the sediment is increased from 10^{-6} to 10^{-5} (kmol Si $\mathrm{m}^{-3})^{-1}$ sec^{-1} in order to increase the diffusion flux of silicate from the sediment to the ocean (Figure S.7). It is further increased to 3×10^{-5}, 10^{-4} and 5×10^{-4}(kmol Si $\mathrm{m}^{-3})^{-1}$ sec^{-1}, while the opal dissolution rate constant in the ocean is fixed to 3.0×10^{-3} d^{-1} (Figure S.8).

◇ Sensitivity tests for the Si input into the ocean

- Variation of Si input

  The silicon riverine input flux is varied at a magnitude of 15, 11 and 9 Tmol yr^{-1}

Table S.1: Parameters tuned for the Si cycle

Model Parameter	Original value	Final value
Global riverine input of Si (Tmol Si yr^{-1})	None	9.0
Half saturation constant for Si(OH)$_4$ uptake: $K_{PHY}^{\mathrm{Si(OH)_4}}$ (μmol L^{-1})	1.0	4.0
Constant sinking speed of opal: w_{opal}* (m d^{-1})	10	10
Opal redissolution rate constant, water column (d^{-1})	0.01	3.0×10^{-3}
Opal redissolution rate constant, sediment ((kmol Si m^{-3})$^{-1}$ s^{-1})	1.0×10^{-6}	1.0×10^{-3}
Si(OH)$_4$ saturation concentration* (μmol L^{-1})	1000	1000

*Note that the original values are kept for the final model setting.

(Figure S.8 and S.9).

To sum up, a realistic initial concentration and distribution of silicic acid, besides a realistic input flux of silicon, is important to obtain a balanced input and loss of silicon from the ocean-sediment system and at the same time a realistic silicic acid distribution within the water column. The biogenic opal dissolution rate both in the ocean and in the sediment is essential for determination of the silicic acid distribution. The silicate uptake half-saturation constant and opal sinking speed can be used to adjust the surface and deep concentrations, respectively. The original and final setting of these parameters are listed in Table S.1.

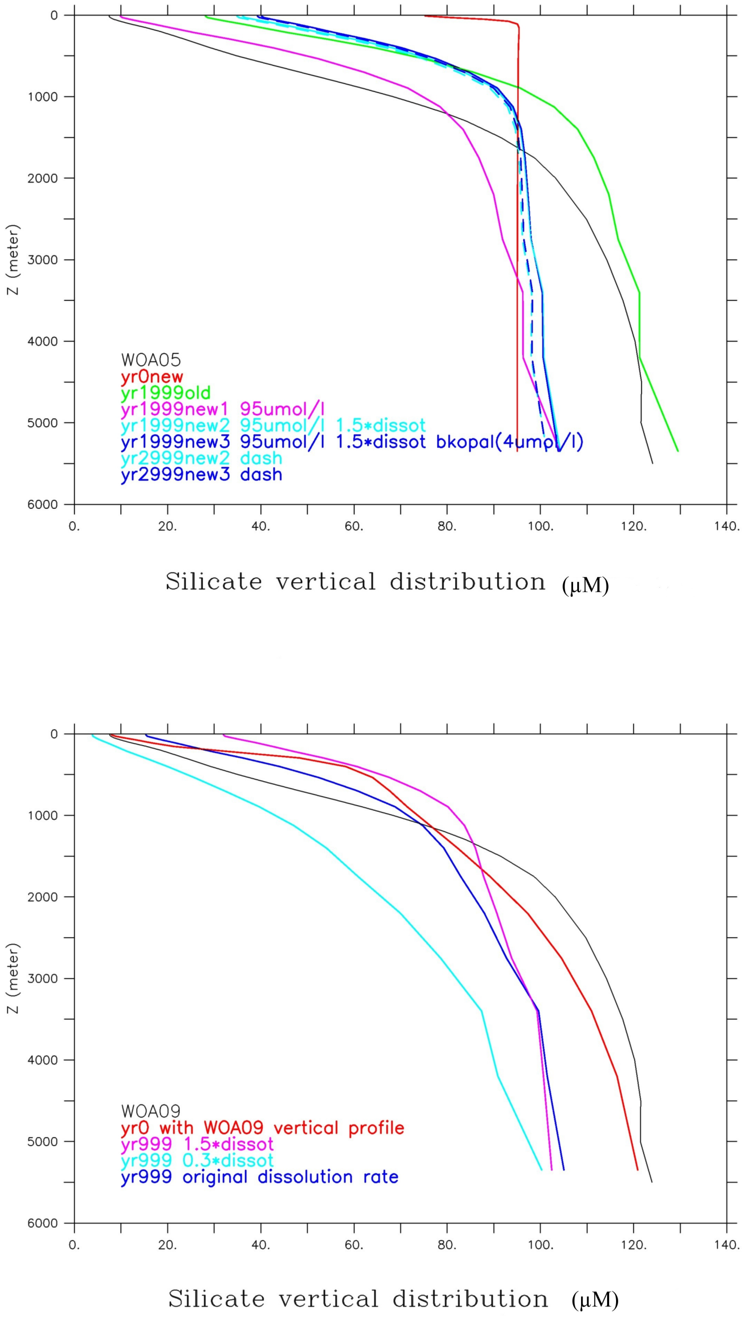

Figure S.3: The horizontally averaged vertical profiles of silicic acid with varying initial silicic acid concentration, silicate uptake half-saturation constant and opal dissolution rate.

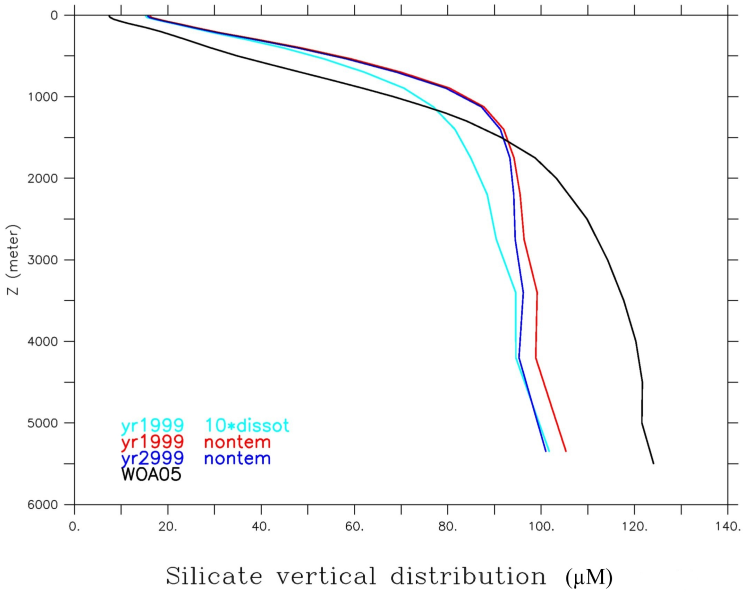

Figure S.4: The horizontally averaged vertical profiles of silicic acid with varying opal dissolution rate, with both temperature-dependent and -independent formulation.

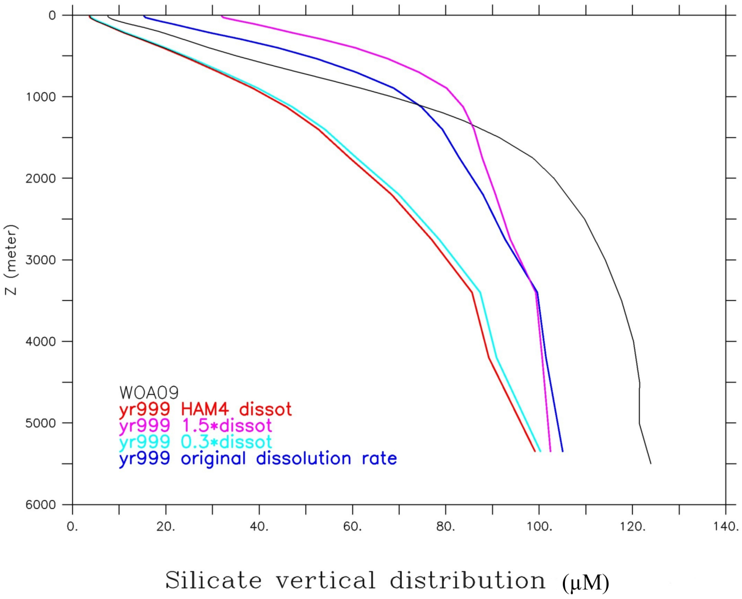

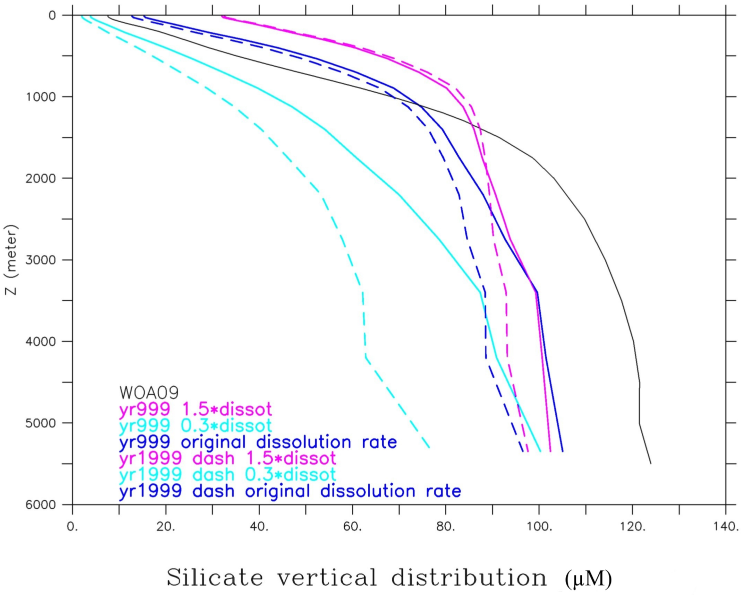

Figure S.5: The horizontally averaged vertical profiles of silicic acid with varying opal dissolution rate.

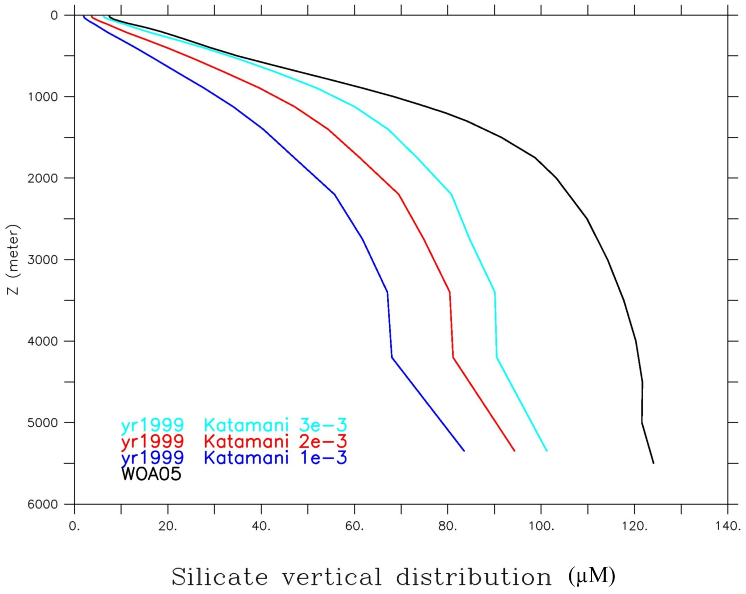

Figure S.6: The horizontally averaged vertical profiles of silicic acid with varying opal dissolution rate, based on *Kamatani* (1982)'s temperature-dependent formulation.

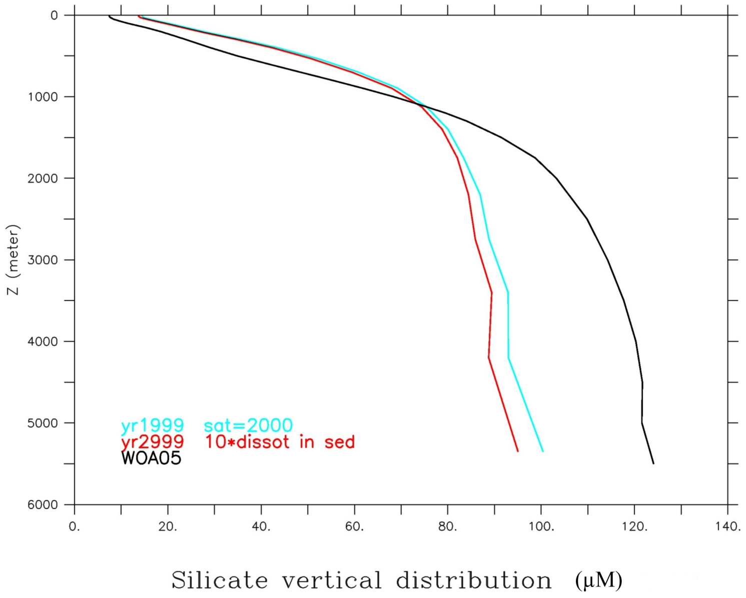

Figure S.7: The horizontally averaged vertical profiles of silicic acid with varying opal dissolution rate in the sediment.

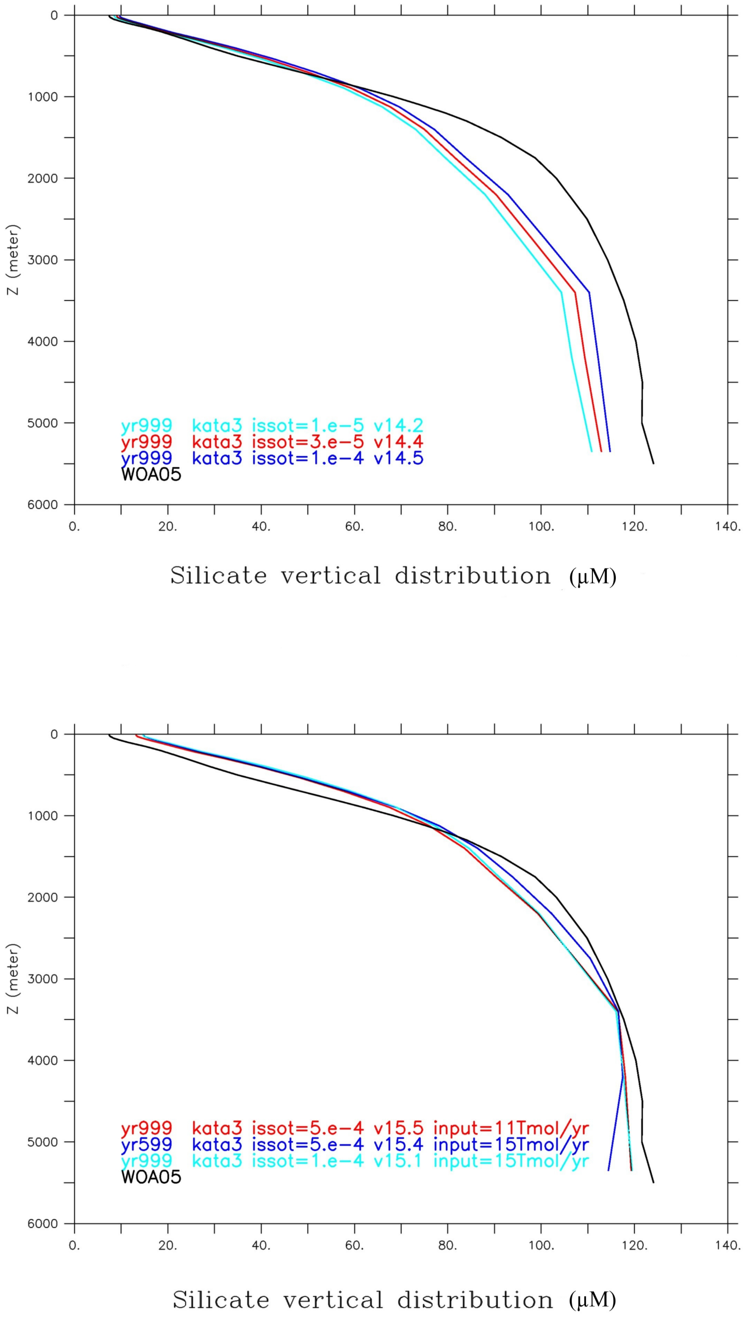

Figure S.8: The horizontally averaged vertical profiles of silicic acid with varying opal dissolution rate in the sediment and Si input flux.

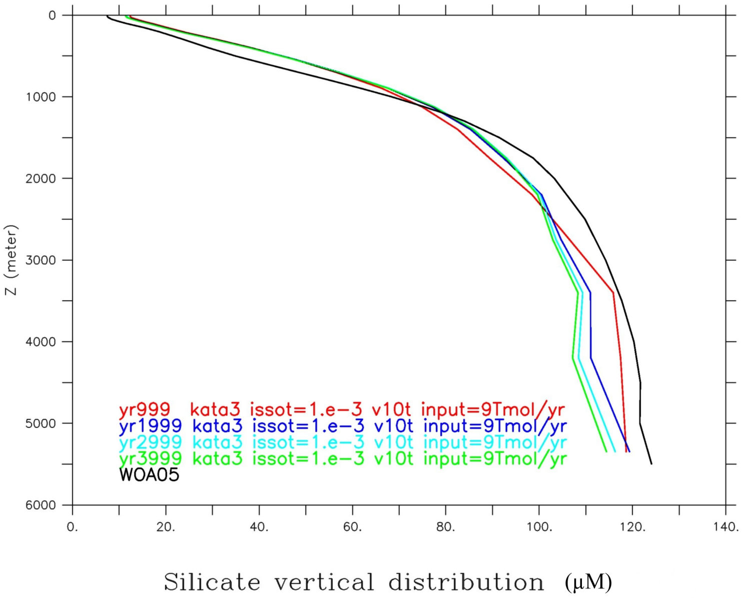

Figure S.9: Evolution of the horizontally averaged vertical profiles of silicic acid with time, with fixed opal dissolution rate in the ocean and sediment and the input flux of Si.

Bibliography

Annan, J., and J. Hargreaves (2013), A new global reconstruction of temperature changes at the Last Glacial Maximum, *Climate of the Past*, *9*(1), 367–376.

Archer, D., A. Winguth, D. Lea, and N. Mahowald (2000), What caused the glacial/interglacial atmospheric $p\mathrm{CO}_2$ cycles?, *Rev. Geophys.*, *38*(2), 159–189.

Armbrust, E. V. (2009), The life of diatoms in the world's oceans, *Nature*, *459*(7244), 185–192.

Assmy, P., V. Smetacek, M. Montresor, C. Klaas, J. Henjes, V. H. Strass, J. M. Arrieta, U. Bathmann, G. M. Berg, E. Breitbarth, B. Cisewski, L. Friedrichs, N. Fuchs, G. J. Herndl, S. Jansen, S. Krägefsky, M. Latasa, I. Peeken, R. Röttgers, R. Scharek, S. E. Schüller, S. Steigenberger, A. Webb, and D. Wolf-Gladrow (2013), Thick-shelled, grazer-protected diatoms decouple ocean carbon and silicon cycles in the iron-limited Antarctic Circumpolar Current, *Proceedings of the National Academy of Sciences*, doi:10.1073/pnas.1309345110.

Aumont, O., E. Maier-Reimer, S. Blain, and P. Monfray (2003), An ecosystem model of the global ocean including Fe, Si, P colimitations, *Global Biogeochem. Cycles*, *17*(2), 1060.

Baines, S. B., B. S. Twining, M. A. Brzezinski, D. M. Nelson, and N. S. Fisher (2010), Causes and biogeochemical implications of regional differences in silicification of marine diatoms, *Global Biogeochem. Cycles*, *24*, GB4031, doi:10.1029/2010GB003856.

Barker, P., J.-C. Fontes, F. Gasse, and J.-C. Druart (1994), Experimental dissolution of diatom silica in concentrated salt solutions and implications for paleoenvironmental reconstruction, *Limnology and Oceanography*, *39*, 99–110.

Bernard, C. Y., H. H. Dürr, C. Heinze, J. Segschneider, and E. Maier-Reimer (2011), Contribution of riverine nutrients to the silicon biogeochemistry of the global ocean – a model study, *Biogeosciences*, *8*(3), 551–564, doi:10.5194/bg-8-551-2011.

Berner, R. A. (1997), The rise of plants and their effect on weathering and atmospheric CO_2, *Science*, *276*(5312), 544–546, doi:10.1126/science.276.5312.544.

Beucher, C. P., M. A. Brzezinski, and X. Crosta (2007), Silicic acid dynamics in the glacial sub-Antarctic: Implications for the silicic acid leakage hypothesis, *Global Biogeochem. Cycles*, *21*(3), GB3015.

Beucher, C. P., M. A. Brzezinski, and J. L. Jones (2008), Sources and biological fractionation of Silicon isotopes in the Eastern Equatorial Pacific, *Geochimica et Cosmochimica Acta*, *72*(13), 3063–3073.

Beucher, C. P., M. A. Brzezinski, and J. L. Jones (2011), Mechanisms controlling silicon isotope distribution in the Eastern Equatorial Pacific, *Geochimica et Cosmochimica Acta*, *75*(15), 4286–4294.

Bidle, K. D., and F. Azam (1999), Accelerated dissolution of diatom silica by marine bacterial assemblages, *Nature*, *397*(6719), 508–512.

Bidle, K. D., M. Manganelli, and F. Azam (2002), Regulation of oceanic silicon and carbon preservation by temperature control on bacteria, *Science*, *298*(5600), 1980–1984.

Blank, G. S., D. H. Robinson, and C. W. Sullivan (1986), Diatom mineralization of silicic acid. VIII. Metabolic requirements and the timing of protein synthesis, *Journal of Phycology*, *22*(3), 382–389.

Broecker, W., and T.-H. Peng (1993), What caused the glacial to interglacial CO_2 change, in *The Global Carbon Cycle*, vol. 15, edited by M. Heimann, NATO ASI Series, Springer, Berlin.

Broecker, W. S., and G. M. Henderson (1998), The sequence of events surrounding Termination II and their implications for the cause of glacial-interglacial CO_2 changes, *Paleoceanography*, *13*(4), 352–364.

Brzezinski, M. A., and D. M. Nelson (1995), The annual silica cycle in the Sargasso Sea near Bermuda, *Deep Sea Research Part I: Oceanographic Research Papers*, *42*(7), 1215–1237.

Brzezinski, M. A., C. J. Pride, V. M. Franck, D. M. Sigman, J. L. Sarmiento, K. Matsumoto, N. Gruber, G. H. Rau, and K. H. Coale (2002), A switch from $Si(OH)_4$ to NO_3^- depletion in the glacial Southern Ocean, *Geophys. Res. Lett.*, *29*(12), 1564.

Buesseler, K. O. (1998), The decoupling of production and particulate export in the surface ocean, *Global Biogeochem. Cycles*, *12*(2), 297–310.

Cardinal, D., L. Y. Alleman, F. Dehairs, N. Savoye, T. W. Trull, and L. André (2005), Relevance of silicon isotopes to Si-nutrient utilization and Si-source assessment in Antarctic waters, *Global Biogeochem. Cycles*, *19*(2), GB2007.

Cardinal, D., N. Savoye, T. W. Trull, F. Dehairs, E. E. Kopczynska, F. Fripiat, J.-L. Tison, and L. André (2007), Silicon isotopes in spring Southern Ocean diatoms: Large zonal changes despite homogeneity among size fractions, *Marine Chemistry*, *106*(1-2), 46–62.

Claquin, P., V. Martin-Jézéquel, J. C. Kromkamp, M. J. W. Veldhuis, and G. W. Kraay (2002), Uncoupling of silicon compared with carbon and nitrogen metabolisms and the role of the cell cycle in continuous cultures of Thalassiosira pseudonana (bacillariophyceae) under light, nitrogen, and phosphorus control, *Journal of Phycology*, *38*(5), 922–930.

Clark, P. U., A. S. Dyke, J. D. Shakun, A. E. Carlson, J. Clark, B. Wohlfarth, J. X. Mitrovica, S. W. Hostetler, and A. M. McCabe (2009), The Last Glacial Maximum, *Science*, *325*(5941), 710–714, doi:10.1126/science.1172873.

Conley, D. J. (1997), Riverine contribution of biogenic silica to the oceanic silica budget, *Limnol. Oceanogr.*, *42*, 774–777.

Conley, D. J. (2002), Terrestrial ecosystems and the global biogeochemical silica cycle, *Global Biogeochem. Cycles*, *16*(4), 1121.

Conley, D. J., and C. L. Schelske (2001), Biogenic Silica, in *Developments in Paleoenvironmental Research*, vol. 3, edited by J. P. Smol, H. J. B. Birks, W. M. Last, R. S. Bradley, and K. Alverson, pp. 281–293, Springer Netherlands.

Coplen, T. B., J. A. Hopple, J. K. Böhlke, H. S. Peiser, S. E. Rieder, H. R. Krouse, K. J. R. Rosman, T. Ding, R. Vocke, J. K. M. Révész, A. Lamberty, P. Taylor, and P. De Bièvre (2002), Compilation of minimum and maximum isotope ratios of selected elements in naturally occurring terrestrial materials and reagents, *Water Resources Investigation Report 01-4222*, U.S. Department of the Interior and U.S. Geological Survey, Vancouver.

de Brauwere, A., F. Fripiat, D. Cardinal, A.-J. Cavagna, F. De Ridder, L. André, and M. Elskens (2012), Isotopic model of oceanic silicon cycling: The Kerguelen Plateau case study, *Deep Sea Research Part I: Oceanographic Research Papers*, *70*(0), 42–59.

De La Rocha, C. L., and M. J. Bickle (2005), Sensitivity of silicon isotopes to whole-ocean changes in the silica cycle, *Mar Geol*, *217*(3-4), 267–282.

De La Rocha, C. L., M. A. Brzezinski, and M. J. DeNiro (1997), Fractionation of silicon isotopes by marine diatoms during biogenic silica formation, *Geochimica et Cosmochimica Acta*, *61*(23), 5051–5056.

De La Rocha, C. L., M. A. Brzezinski, M. J. DeNiro, and A. Shemesh (1998), Silicon-isotope composition of diatoms as an indicator of past oceanic change, *Nature*, *395*(6703), 680–683.

De La Rocha, C. L., M. A. Brzezinski, and M. J. DeNiro (2000), A first look at the distribution of the stable isotopes of silicon in natural waters, *Geochimica et Cosmochimica Acta*, *64*(14), 2467–2477.

De La Rocha, C. L., P. Bescont, A. Croguennoc, and E. Ponzevera (2011), The silicon isotopic composition of surface waters in the Atlantic and Indian sectors of the Southern Ocean, *Geochimica et Cosmochimica Acta*, *75*(18), 5283–5295.

de Souza, G. F., B. C. Reynolds, G. C. Johnson, J. L. Bullister, and B. Bourdon (2012a), Silicon stable isotope distribution traces Southern Ocean export of Si to the eastern South Pacific thermocline, *Biogeosciences*, *9*(11), 4199–4213.

de Souza, G. F., B. C. Reynolds, J. Rickli, M. Frank, M. A. Saito, L. J. A. Gerringa, and B. Bourdon (2012b), Southern Ocean control of silicon stable isotope distribution in the deep Atlantic Ocean, *Global Biogeochem. Cycles*, *26*(2), GB2035.

Demarest, M. S., M. A. Brzezinski, and C. P. Beucher (2009), Fractionation of silicon isotopes during biogenic silica dissolution, *Geochimica et Cosmochimica Acta*, *73*(19), 5572–5583.

DeMaster, D. J. (2002), The accumulation and cycling of biogenic silica in the Southern Ocean: revisiting the marine silica budget, *Deep Sea Research Part II: Topical Studies in Oceanography*, *49*(16), 3155–3167.

Dezileau, L., G. Bareille, and J. Reyss (2003), The 231Pa/230Th ratio as a proxy for past changes in opal fluxes in the Indian sector of the Southern Ocean, *Marine Chemistry*, *81*, 105–117.

Ding, T., D. Wan, R. Bai, Z. Zhang, Y. Shen, and R. Meng (2005), Silicon isotope abundance ratios and atomic weights of NBS-28 and other reference materials, *Geochimica et Cosmochimica Acta*, *69*(23), 5487–5494.

Drum, R. W., and H. S. Pankratz (1964), Post mitotic fine structure of Gomphonema parvulum, *Journal of Ultrastructure Research*, *10*(3–4), 217–223.

Dubois, N., M. Kienast, S. Kienast, S. E. Calvert, R. Francois, and R. F. Anderson (2010), Sedimentary opal records in the eastern equatorial Pacific: It is not all about leakage, *Global Biogeochem. Cycles*, *24*, GB4020, doi:10.1029/2010GB003821.

Dugdale, R. C., F. P. Wilkerson, and H. J. Minas (1995), The role of a silicate pump in driving new production, *Deep Sea Research Part I: Oceanographic Research Papers*, *42*(5), 697–719.

Dunne, J. P., J. L. Sarmiento, and A. Gnanadesikan (2007), A synthesis of global particle export from the surface ocean and cycling through the ocean interior and on the seafloor, *Global Biogeochem. Cycles*, *21*(4), GB4006.

Dürr, H. H., M. Meybeck, J. Hartmann, G. G. Laruelle, and V. Roubeix (2011), Global spatial distribution of natural riverine silica inputs to the coastal zone, *Biogeosciences*, *8*(3), 597–620.

Ehrlich, H., K. D. Demadis, O. S. Pokrovsky, and P. G. Koutsoukos (2010), Modern views on desilicification: Biosilica and abiotic silica dissolution in natural and artificial environments, *Chem. Rev.*, *110*(8), 4656–4689, doi:10.1021/cr900334y.

Ellwood, M. J., M. Wille, and W. Maher (2010), Glacial Silicic Acid Concentrations in the Southern Ocean, *Science*, *330*(6007), 1088–1091.

Fofonoff, N. P., and R. C. Millard (1983), Algorithms for the Computation of Fundamental Properties of Seawater, *UNESCO Technical Papers in Marine Science 44*, Division of Marine Sciences, Unesco, Place de Fontenoy, Paris, France.

Fripiat, F., A. J. Cavagna, F. Dehairs, S. Speich, L. André, and D. Cardinal (2011a), Silicon pool dynamics and biogenic silica export in the Southern Ocean inferred from Si-isotopes, *Ocean Sci.*, *7*(5), 533–547.

Fripiat, F., A.-J. Cavagna, N. Savoye, F. Dehairs, L. André, and D. Cardinal (2011b), Isotopic constraints on the Si-biogeochemical cycle of the Antarctic Zone in the Kerguelen area (KEOPS), *Marine Chemistry*, *123*(1-4), 11–22.

Fripiat, F., A.-J. Cavagna, F. Dehairs, A. de Brauwere, L. André, and D. Cardinal (2012), Processes controlling the Si-isotopic composition in the Southern Ocean and application for paleoceanography, *Biogeosciences*, *9*(7), 2443–2457.

Fry, B. (2006), Fractionation, in *Stable Isotope Ecology*, pp. 194–270, Springer, New York.

Garcia, H. E., R. A. Locarnini, T. P. Boyer, J. I. Antonov, M. M. Zweng, O. K. Baranova, and D. R. Johnson (2010), World Ocean Atlas 2009, Volume 4: Nutrients (phosphate, nitrate, silicate), *Tech. rep.*, S. Levitus, Ed. NOAA Atlas NESDIS 71, U.S. Government Printing Office, Washington, D.C.

Gent, P. R., J. Willebrand, T. J. McDougall, and J. C. McWilliams (1995), Parameterizing Eddy-Induced Tracer Transports in Ocean Circulation Models, *J. Phys. Oceanogr.*, *25*(4), 463–474.

Georg, R. B., B. C. Reynolds, M. Frank, and A. N. Halliday (2006), Mechanisms controlling the silicon isotopic compositions of river waters, *Earth and Planetary Science Letters*, *249*(3-4), 290–306.

Grasse, P., C. Ehlert, and M. Frank (2013), The influence of water mass mixing on the dissolved Si isotope composition in the Eastern Equatorial Pacific, *Earth and Planetary Science Letters*, *380*(0), 60–71.

Hasle, G. R., and E. E. Syvertsen (1996), Chapter 2 - marine diatoms, in *Identifying Marine Diatoms and Dinoflagellates*, edited by C. R. Tomas, G. R. Hasle, E. E. Syvertsen, K. A. Steidinger, and K. Tangen, pp. 5–385, Academic Press, San Diego.

Heinze, C., E. Maier-Reimer, A. M. E. Winguth, and D. Archer (1999), A global oceanic sediment model for long-term climate studies, *Global Biogeochem. Cycles*, *13*(1), 221–250.

Honjo, S., S. J. Manganini, R. A. Krishfield, and R. Francois (2008), Particulate organic carbon fluxes to the ocean interior and factors controlling the biological pump: A synthesis of global sediment trap programs since 1983, *Progress in Oceanography*, *76*(3), 217–285.

Hurd, D. C., and S. Birdwhistell (1983), On producing a more general model for biogenic silica dissolution, *American Journal of Science*, *283*(1), 1–28.

Hutchins, D. A., and K. W. Bruland (1998), Iron-limited diatom growth and Si:N uptake ratios in a coastal upwelling regime, *Nature*, *393*(6685), 561–564.

Jacobson, D. M., and D. M. Anderson (1986), Thecate heterophic dinoflagellates: Feeding behavior and mechanisms, *Journal of Phycology*, *22*(3), 249–258.

Johnson, K. S., R. M. Gordon, and K. H. Coale (1997), What controls dissolved iron concentrations in the world ocean?, *Marine Chemistry*, *57*(3-4), 137–161.

Kamatani, A. (1982), Dissolution rates of silica from diatoms decomposing at various temperatures, *Marine Biology*, *68*(1), 91–96.

Kaufman, P. B., P. Dayanandan, Y. Takeoka, W. C. Bigelow, J. D. Jones, and R. Iler (1981), Silica in shoots of higher plants, in *Silicon and Siliceous Structures in Biological Systems*, edited by T. L. Simpson and B. E. Volcani, pp. 409–449, Springer-Verlag, New York.

Kohfeld, K. E., and A. Ridgwell (2009), Glacial-Interglacial Variability in Atmospheric CO_2, in *Surface Ocean/Lower Atmosphere Processes*, edited by C. Le Quéré and E. Saltzman, pp. 251–286, American Geophysical Union, Washington, DC.

Köhler, P., and R. Bintanja (2008), The carbon cycle during the Mid Pleistocene Transition: the Southern Ocean Decoupling Hypothesis, *Clim. Past*, *4*(4), 311–332.

Kriest, I., A. Oschlies, and S. Khatiwala (2012), Sensitivity analysis of simple global marine biogeochemical models, *Global Biogeochem. Cycles*, *26*(2), GB2029.

Kröger, N., and N. Poulsen (2008), Diatoms—From Cell Wall Biogenesis to Nanotechnology, *Annu. Rev. Genet.*, *42*(1), 83–107.

Lam, P. J., S. C. Doney, and J. K. B. Bishop (2011), The dynamic ocean biological pump: Insights from a global compilation of particulate organic carbon, $CaCO_3$, and opal concentration profiles from the mesopelagic, *Global Biogeochem. Cycles*, *25*(3), GB3009.

Laruelle, G. G., V. Roubeix, A. Sferratore, B. Brodherr, D. Ciuffa, D. J. Conley, H. H. Dürr, J. Garnier, C. Lancelot, Q. Le Thi Phuong, J.-D. Meunier, M. Meybeck, P. Michalopoulos, B. Moriceau, S. Ní Longphuirt, S. Loucaides, L. Papush, M. Presti, O. Ragueneau, P. Regnier, L. Saccone, C. P. Slomp, C. Spiteri, and P. Van Cappellen (2009), Anthropogenic perturbations of the silicon cycle at the global scale: Key role of the land-ocean transition, *Global Biogeochem. Cycles*, *23*(4), GB4031.

Legutke, S., and E. Maier-Reimer (2002), The impact of a downslope water-transport parametrization in a global ocean general circulation model, *Climate Dynamics*, *18*, 611 – 623.

Lewin, J. C. (1961), The dissolution of silica from diatom walls, *Geochimica et Cosmochimica Acta*, *21*(3–4), 182–198.

Mahowald, N. M., M. Yoshioka, W. D. Collins, A. J. Conley, D. W. Fillmore, and D. B. Coleman (2006), Climate response and radiative forcing from mineral aerosols during the last glacial maximum, pre-industrial, current and doubled-carbon dioxide climates, *Geophys. Res. Lett.*, *33*(20), L20,705.

Maier-Reimer, E., I. Kriest, J. Segschneider, and P. Wetzel (2005), The HAMburg Ocean Carbon Cycle Model HAMOCC 5.1, *Technical Description Release 1.1*, Max Planck Institute for Meteorology, Hamburg.

Mann, D. G., and S. J. M. Droop (1996), Biodiversity, biogeography and conservation of diatoms, *Hydrobiologia*, *336*(1-3), 19–32.

Marshall, J., and K. Speer (2012), Closure of the meridional overturning circulation through Southern Ocean upwelling, *Nature Geosci.*, *5*(3), 171–180.

Marsland, S. J., H. Haak, J. H. Jungclaus, M. Latif, and F. Roske (2003), The Max-Planck-Institute global ocean/sea ice model with orthogonal curvilinear coordinates, *Ocean Modelling*, *5*(2), 91–127.

Martin, J. H., G. A. Knauer, D. M. Karl, and W. W. Broenkow (1987), VERTEX: carbon cycling in the northeast Pacific, *Deep Sea Research Part A. Oceanographic Research Papers*, *34*(2), 267–285.

Martin-Jézéquel, V., M. Hildebrand, and M. A. Brzezinski (2000), Silicon metabolism in diatoms: Implications for growth, *Journal of Phycology*, *36*(5), 821–840.

Matsumoto, K., J. L. Sarmiento, and M. A. Brzezinski (2002), Silicic acid leakage from the Southern Ocean: A possible explanation for glacial atmospheric $p\mathrm{CO}_2$, *Global Biogeochem. Cycles*, *16*(3), 1031.

Matsumoto, K., K. Tokos, A. Huston, and H. Joy-Warren (2013), MESMO 2: a mechanistic marine silica cycle and coupling to a simple terrestrial scheme, *Geosci. Model Dev.*, *6*(2), 477–494.

Miller, C., D. Nelson, C. Weiss, and A. Soeldner (1990), Morphogenesis of opal teeth in calanoid copepods, *Marine Biology*, *106*(1), 91–101.

Milligan, A. J., D. E. Varela, M. A. Brzezinski, and F. M. M. Morel (2004), Dynamics of Silicon Metabolism and Silicon Isotopic Discrimination in a Marine Diatom as a Function of pCO_2, *Limnology and Oceanography*, *49*(2), 322–329.

Mix, A. C., E. Bard, and R. Schneider (2001), Environmental processes of the ice age: land, oceans, glaciers (EPILOG), *Quaternary Science Reviews*, *20*(4), 627–657.

Murakami, S., R. Ohgaito, A. Abe-Ouchi, M. Crucifix, and B. L. Otto-Bliesner (2008), Global-scale energy and freshwater balance in glacial climate: A comparison of three PMIP2 LGM simulations, *Journal of Climate*, *21*(19), 5008–5033.

Nelson, D. M., and W. O. Smith Jr. (1986), Phytoplankton bloom dynamics of the western Ross Sea ice edge–II. Mesoscale cycling of nitrogen and silicon, *Deep Sea Research Part A. Oceanographic Research Papers*, *33*(10), 1389–1412.

Nelson, D. M., P. Tréguer, M. A. Brzezinski, A. Leynaert, and B. Quéguiner (1995), Production and dissolution of biogenic silica in the ocean: Revised global estimates, comparison with regional data and relationship to biogenic sedimentation, *Global Biogeochem. Cycles*, *9*(3), 359–372.

Nelson, D. M., R. F. Anderson, R. T. Barber, M. A. Brzezinski, K. O. Buesseler, Z. Chase, R. W. Collier, M.-L. Dickson, R. François, M. R. Hiscock, S. Honjo, J. Marra, W. R. Martin, R. N. Sambrotto, F. L. Sayles, and D. E. Sigmon (2002), Vertical budgets for organic carbon and biogenic silica in the Pacific sector of the Southern Ocean, 1996-1998, *Deep Sea Research Part II: Topical Studies in Oceanography*, *49*(9–10), 1645–1674.

Nozaki, Y., and Y. Yamamoto (2001), Radium 228 based nitrate fluxes in the eastern Indian Ocean and the South China Sea and a silicon-induced "alkalinity pump" hypothesis, *Global Biogeochem. Cycles*, *15*(3), 555–567.

Parrenin, F., V. Masson-Delmotte, P. Köhler, D. Raynaud, D. Paillard, J. Schwander, C. Barbante, A. Landais, A. Wegner, and J. Jouzel (2013), Synchronous Change of Atmospheric CO_2 and Antarctic Temperature During the Last Deglacial Warming, *Science*, *339*(6123), 1060–1063, doi:10.1126/science.1226368.

Passow, U., M. A. French, and M. Robert (2011), Biological controls on dissolution of diatom frustules during their descent to the deep ocean: Lessons learned from controlled laboratory experiments, *Deep Sea Research Part I: Oceanographic Research Papers*, *58*(12), 1147–1157.

Petit, J. R., J. Jouzel, D. Raynaud, N. I. Barkov, J.-M. Barnola, I. Basile, M. Bender, J. Chappellaz, M. Davis, G. Delaygue, M. Delmotte, V. M. Kotlyakov, M. Legrand, V. Y. Lipenkov, C. Lorius, L. Pépin, C. Ritz, E. Saltzman, and M. Stievenard (1999), Climate and atmospheric history of the past 420,000 years from the Vostok ice core, Antarctica, *Nature*, *399*(6735), 429–436.

Pichevin, L. E., B. C. Reynolds, R. S. Ganeshram, I. Cacho, L. Pena, K. Keefe, and R. M. Ellam (2009), Enhanced carbon pump inferred from relaxation of nutrient limitation in the glacial ocean, *Nature*, *459*(7250), 1114–1117.

Pondaven, P., O. Ragueneau, P. Tréguer, A. Hauvespre, L. Dezileau, and J. L. Reyss (2000), Resolving the 'opal paradox' in the Southern Ocean, *Nature*, *405*(6783), 168–172.

Pondaven, P., M. Gallinari, S. Chollet, E. Bucciarelli, G. Sarthou, S. Schultes, and F. Jean (2007), Grazing-induced changes in cell wall silicification in a marine diatom, *Protist*, *158*(1), 21–28.

Ragueneau, O., P. Tréguer, A. Leynaert, R. F. Anderson, M. A. Brzezinski, D. J. DeMaster, R. C. Dugdale, J. Dymond, G. Fischer, R. François, C. Heinze, E. Maier-Reimer, V. Martin-Jézéquel, D. M. Nelson, and B. Quéguiner (2000), A review of the Si cycle in the modern ocean: recent progress and missing gaps in the application of biogenic opal as a paleoproductivity proxy, *Global and Planetary Change*, *26*(4), 317–365.

Ragueneau, O., N. Dittert, P. Pondaven, P. Tréguer, and L. Corrin (2002), Si/C decoupling in the world ocean: is the Southern Ocean different?, *Deep Sea Research Part II: Topical Studies in Oceanography*, *49*(16), 3127–3154.

Ragueneau, O., S. Schultes, K. Bidle, P. Claquin, and B. Moriceau (2006), Si and C interactions in the world ocean: Importance of ecological processes and implications for the role of diatoms in the biological pump, *Global Biogeochem. Cycles*, *20*(4), GB4S02.

Redfield, A. C. (1934), On the proportions of organic derivations in sea water and their relation to the composition of plankton, in *James Johnstone Memorial Volume*, edited by R. J. Daniel, pp. 177–192, University Press of Liverpool.

Reynolds, B. C. (2009), Modeling the modern marine δ^{30}Si distribution, *Global Biogeochem. Cycles*, *23*(2), GB2015.

Reynolds, B. C., M. Frank, and A. N. Halliday (2006), Silicon isotope fractionation during nutrient utilization in the North Pacific, *Earth and Planetary Science Letters*, *244*(1-2), 431–443.

Rickert, D., M. Schlüter, and K. Wallmann (2002), Dissolution kinetics of biogenic silica from the water column to the sediments, *Geochimica et Cosmochimica Acta*, *66*(3), 439–455.

Round, F. E., R. M. Crawford, and D. G. Mann (1990), Biology of diatoms, in *The diatoms: the biology and morphology of the genera*, pp. 1–130, Cambridge University Press, Cambrige, UK.

Rudnick, R., and S. Gao (2003), 3.01 - composition of the continental crust, in *Treatise on Geochemistry*, edited by H. D. Holland and K. K. Turekian, pp. 1–64, Pergamon, Oxford.

Sarmiento, J. L., and N. Gruber (Eds.) (2006), *Ocean Biogeochemical Dynamics*, Princeton University Press, Princeton, New Jersey, USA.

Sarmiento, J. L., N. Gruber, M. A. Brzezinski, and J. P. Dunne (2004), High-latitude controls of thermocline nutrients and low latitude biological productivity, *Nature*, *427*(6969), 56–60.

Shackleton, N. J. (2000), The 100,000-Year Ice-Age Cycle Identified and Found to Lag Temperature, Carbon Dioxide, and Orbital Eccentricity, *Science*, *289*(5486), 1897–1902, doi: 10.1126/science.289.5486.1897.

Sigman, D. M., and E. A. Boyle (2000), Glacial/interglacial variations in atmospheric carbon dioxide, *Nature*, *407*(6806), 859–869.

Six, K. D., and E. Maier-Reimer (1996), Effects of plankton dynamics on seasonal carbon fluxes in an ocean general circulation model, *Global Biogeochem. Cycles*, *10*(4), 559–583.

Smetacek, V. (1999), Diatoms and the Ocean Carbon Cycle, *Protist*, *150*(1), 25–32.

Sullivan, C. W. (1986), Silicification by diatoms, in *Silicon Biochemistry*, edited by D. Evered and M. O'Connor, pp. 59–89, Wiley and Sons, New York.

Sutton, J. N., D. E. Varela, M. A. Brzezinski, and C. P. Beucher (2013), Species-dependent silicon isotope fractionation by marine diatoms, *Geochimica et Cosmochimica Acta*, *104*(0), 300–309.

Takeda, S. (1998), Influence of iron availability on nutrient consumption ratio of diatoms in oceanic waters, *Nature*, *393*(6687), 774–777.

Toggweiler, J. R., J. L. Russell, and S. R. Carson (2006), Midlatitude westerlies, atmospheric CO_2, and climate change during the ice ages, *Paleoceanography*, *21*(2), PA2005.

Tréguer, P., D. M. Nelson, A. J. Van Bennekom, D. J. DeMaster, A. Leynaert, and B. Quéguiner (1995), The Silica Balance in the World Ocean: A Reestimate, *Science*, *268*(5209), 375–379.

Tréguer, P. J., and C. L. De La Rocha (2013), The World Ocean Silica Cycle, *Annual Review of Marine Science*, *5*(1), 477–501.

Van Bennekom, A., A. Buma, and R. Nolting (1991), Dissolved aluminium in the Weddell-Scotia Confluence and effect of Al on the dissolution kinetics of biogenic silica, *Marine Chemistry*, *35*, 423–434.

Van Cappellen, P., and L. Qiu (1997), Biogenic silica dissolution in sediments of the Southern Ocean. I. Solubility, *Deep Sea Research Part II: Topical Studies in Oceanography*, *44*(5), 1109–1128.

Varela, D. E., C. J. Pride, and M. A. Brzezinski (2004), Biological fractionation of silicon isotopes in Southern Ocean surface waters, *Global Biogeochem. Cycles*, *18*(1), GB1047.

Wilson, J. D., S. Barker, and A. Ridgwell (2012), Assessment of the spatial variability in particulate organic matter and mineral sinking fluxes in the ocean interior: Implications for the ballast hypothesis, *Global Biogeochem. Cycles*, *26*(4), GB4011.

Wischmeyer, A. G. (2002), Modeling the Marine Silicon Cycle-Physics, Chemistry, and Biology, Ph.D thesis, Univ. of Bremen, Bremen, Germany.

Wischmeyer, A. G., C. L. De La Rocha, E. Maier-Reimer, and D. A. Wolf-Gladrow (2003), Control mechanisms for the oceanic distribution of silicon isotopes, *Global Biogeochem. Cycles*, *17*(3), 1083.

Xu, X. (2012), Variations of oceanic and foraminiferal oxygen isotopes at the present day and the Last Glacial Maximum, Ph.D thesis, Univ. of Bremen, Bremen, Germany.

Yokoyama, Y., K. Lambeck, P. De Deckker, P. Johnston, and L. K. Fifield (2000), Timing of the Last Glacial Maximum from observed sea-level minima, *Nature*, *406*(6797), 713–716.

Zhang, X., G. Lohmann, G. Knorr, and X. Xu (2013), Different ocean states and transient characteristics in Last Glacial Maximum simulations and implications for deglaciation, *Clim. Past*, *9*(5), 2319–2333.